

# **Design of Tissue Leaflets for a Percutaneous Aortic Valve**

**by**

**Adriaan Nicolaas Smuts**

*Thesis presented at Stellenbosch University in  
partial fulfilment of the requirements for the  
degree of*

**Master of Science in Mechatronic Engineering**

Department of Mechanical and Mechatronic Engineering  
Stellenbosch University  
South Africa

Supervisors: Prof. C Scheffer  
Dr. DC Blaine

March 2009

Copyright © 2009 Stellenbosch University

All rights reserved

## DECLARATION

I, the undersigned, hereby declare that the work contained in this thesis is my own original work and that I have not previously in its entirety or in part submitted it at any university for a degree.

Signed: .....

Adriaan Nicolaas Smuts

Date: .....

Copyright © 2009 Stellenbosch University

All rights reserved

# **ABSTRACT**

## **Design of tissue leaflets for a percutaneous aortic valve**

A.N. Smuts

*Department of Mechanical and Mechatronic Engineering*

*Stellenbosch University*

*Private Bag XI, 7602 Matieland, South Africa*

Thesis: MScEng (Mechanical)

March 2009

In this project the shape and attachment method of tissue leaflets for a percutaneous aortic valve is designed and tested as a first prototype. Bovine and kangaroo pericardium was tested and compared with natural human valve tissue by using the Fung elastic constitutive model for skin. Biaxial tests were conducted to determine the material parameters for each material. The constitutive model was implemented using finite element analysis (FEA) by applying a user-specified subroutine. The FEA implementation was validated by simulating the biaxial tests and comparing it with the experimental data. Concepts for different valve geometries were developed by incorporating valve design and performance parameters, along with stent constraints. Attachment techniques and tools were developed for valve manufacturing. FEA was used to evaluate two concepts. The influence of effects such as different leaflet material, material orientation and abnormal valve dilation on the valve function was investigated. The stress distribution across the valve leaflet was examined to determine the appropriate fibre direction for the leaflet. The simulated attachment forces were compared with suture tearing tests performed on the pericardium to evaluate suture density. In vitro tests were conducted to evaluate the valve function. Satisfactory testing results for the prototype valves were found which indicates the possibility for further development and refinement.

# UITTREKSEL

## Ontwerp van weefsel klepsuile vir 'n perkutane aorta klep

("The design of tissue leaflets for a percutaneous aortic valve")

A.N. Smuts

*Departement Meganiese en Megatroniese Ingenieurswese*

*Universiteit van Stellenbosch*

*Privaatsak XI, 7602 Matieland, Suid-Afrika*

Thesis: MScEng (Meganies)

Maart 2009

In hierdie projek word die vorm en hegingsmetode van weefsel klepsuile vir 'n perkutane aortiese klep ontwerp en getoets as 'n eerste prototipe. Bees en kangaroo perikardium is getoets en vergelyk met vars menslike klepweefsel deur gebruik te maak van die Fung elastiese konstitiewe model vir vel. Biaksiale toetse is uitgevoer om die materiaal eienskappe van elke materiaal te bepaal. Die Fung model is geïmplementeer in eindige element analise deur gebruik te maak van 'n operateur-gespesifiseerde subroetine. Die eindige element analise is gevalideer deur die biaksiale toetse te simuleer en die resultate met die eksperimentele data te vergelyk. Konsepte vir verskillende klep geometrieë is ontwikkel deur die insluiting van klep ontwerp en werksverrigting parameters tesame met die beperkinge van die binnespalk. Hegtingstegnieke en gereedskap is ontwikkel vir die vervaardiging van die kleppe. Eindige element analise is gebruik om twee van die konsepte te evalueer. Die invloed van effekte soos verskillende klepsuil materiale, materiaal oriëntasie en abnormale klep dilatasie op die funksie van die klep is ondersoek. Die spannings-distribusie oor die klepsuil is ondersoek om die toepaslike veselrigting vir die klep te bepaal. Gesimuleerde vashegtingskragte is vergelyk met die skeurtoetse van steke in die perikard om die digtheid van die steke te evalueer. In vitro toetse is gedoen om die funksie van die klep te evalueer. Bevredigende toetsresultate vir die prototipe kleppe is verkry wat die moontlikheid vir vêrdere ontwikkeling en verfyning aandui.

## ACKNOWLEDGEMENTS

I would like to express my sincere gratitude to the following people and organizations that have contributed to this project and help make this work possible:

- My promoters, Prof. Cornie Scheffer, Dr. Debbie Blaine, Dr. Hellmuth Weich, Prof. Albert Groenwold and Mr. Kobus van der Westhuizen. Thank you for your valuable contributions, patience and advice.
- Dr. Hellmuth Weich and Prof. Anton Doubell of Tygerberg Hospital for providing the funding for the project as well as enthusiastic support.
- Mr. Anton Esterhuysen and Mr. Karl van Aswegen for making valuable contributions to the project. I enjoyed working with you.
- Prof. Leon Neethling, thank you for all your enthusiasm and valuable contribution to the project.
- Mr. Rusbeh Göcke who assisted me with my testing.
- All my fellow students in the office. Thank you for all the intellectual conversations and humor.
- The staff in the workshop, thanks for all the inputs and humor.
- My family who supported me all the way and provided a steady shoulder to lean on.

# DEDICATIONS

*To my family*

# CONTENTS

DECLARATION .....	i
ABSTRACT.....	ii
UITTREKSEL .....	iii
ACKNOWLEDGEMENTS.....	iv
DEDICATIONS.....	v
CONTENTS.....	vi
LIST OF FIGURES .....	x
LIST OF TABLES.....	xiii
GLOSSARY & NOMENCLATURE .....	xiv
CHAPTER 1 .....	1
1. INTRODUCTION.....	1
1.1 Background .....	1
1.2 Objectives.....	1
1.3 Motivation.....	1
1.4 Thesis overview .....	2
CHAPTER 2 .....	3
2. LITERATURE REVIEW.....	3
2.1 The heart and heart valves.....	3
2.2 The aortic valve.....	4
2.3 Aortic valve disease .....	4
2.3.1 Aortic stenosis.....	4
2.3.2 Aortic regurgitation.....	5
2.4 Aortic valve disease treatment .....	5
2.4.1 Conventional treatments .....	6
2.4.2 Percutaneous aortic valve replacement (PAVR) .....	8
2.4.3 Current limitations in PAVR .....	9
2.4.4 PAVR technique .....	10
2.5 Valve material and treatment .....	11

2.5.1	Conventional materials .....	11
2.5.2	Material used for this study .....	11
2.6	Material storage and testing solutions.....	12
2.7	Valve design requirements .....	12
2.8	Valve testing.....	13
2.9	Recent research .....	14
CHAPTER 3	.....	15
3.	MATERIAL PROPERTIES .....	15
3.1	The constitutive equation of skin .....	15
3.2	Biaxial testing device .....	16
3.2.1	Load Application and Capturing.....	17
3.2.2	Pulley System .....	17
3.2.3	Temperature control.....	19
3.3	Camera calibration .....	20
3.3.1	The camera model.....	20
3.3.2	Lens distortion model .....	22
3.3.3	Calibration technique.....	22
3.4	Strain calculation.....	23
3.5	Stress calculation.....	26
3.6	Test protocol.....	28
3.6.1	Sample selection and preparation .....	28
3.6.2	Placement of sample in the testing device .....	29
3.6.3	Human tissue test setup.....	30
3.6.4	Calibration .....	31
3.6.5	Graphical user interface (GUI) and data processing.....	31
3.7	Material parameters.....	33
3.7.1	Enforcement of convexity.....	33
3.7.2	Condition number .....	34
3.7.3	Nonlinear regression .....	34
CHAPTER 4	.....	36

4. MATERIAL EVALUATION .....	36
4.1 Material constants .....	36
4.2 Finite element analysis (FEA) implementation.....	37
4.3 Finite element analysis (FEA) validation.....	38
4.4 Material comparison.....	40
4.4.1 Stress-strain curve comparison .....	40
4.4.2 Strain energy comparison .....	41
CHAPTER 5 .....	42
5. VALVE DESIGN.....	42
5.1 Native aortic valve dimensions .....	42
5.2 Native aortic valve design- and performance parameters .....	43
5.3 Prosthetic valve design and performance parameters .....	45
5.4 Implementation of valve design parameters .....	46
5.5 Valve geometry design.....	48
CHAPTER 6 .....	51
6. VALVE MANUFACTURING .....	51
6.1 Attachment material considerations.....	51
6.2 Valve sealing considerations.....	52
6.3 Valve attachment considerations.....	53
6.4 Valve assembly tools and techniques.....	55
6.4.1 Suturing techniques.....	55
6.4.2 Knot consideration.....	55
6.4.3 Assembly tools developed .....	56
6.4.4 Assembly procedures.....	57
CHAPTER 7 .....	60
7. FINITE ELEMENT ANALYSIS (FEA) OF VALVE .....	60
7.1 FEA implementation .....	60
7.2 Extreme pressure simulations .....	60
7.3 Material orientation.....	62
7.4 Different leaflet material .....	63

7.5	Over and under dilation of the valve.....	63
7.6	Unsymmetrical dilation of valve.....	64
7.7	Leaflet attachment forces.....	66
7.8	Stress distribution across the valve leaflet.....	67
CHAPTER 8.....		69
8.	TESTING AND RESULTS.....	69
8.1	Camera calibration testing.....	69
8.2	Rupture tests.....	69
8.3	Pulse duplicator tests.....	71
8.4	Crimping diameter.....	72
8.5	Deployment tests.....	73
CHAPTER 9.....		75
9.	CONCLUSIONS AND RECOMMENDATIONS.....	75
9.1	Thesis goal and outcome.....	75
9.2	Challenges, future improvements and recommendations.....	75
9.3	Conclusion.....	76
10.	REFERENCES.....	78
APPENDIX A.....		82
EXPERIMENTAL STRESS-STRAIN RELATIONSHIPS.....		82
APPENDIX B.....		88
USER SUBROUTINE FOR FEA IMPLEMENTATION.....		88

## LIST OF FIGURES

Figure 2-1: Anatomy of the heart ( <a href="http://encarta.msn.com">http://encarta.msn.com</a> ) .....	3
Figure 2-2: An aortic valve with calcific stenosis ( <a href="http://www.pathology.vcu.edu">http://www.pathology.vcu.edu</a> ) ....	5
Figure 2-3: Bioprosthetic and mechanical valves (Shekar <i>et al.</i> , 2006) .....	6
Figure 2-4: The Edwards Lifesciences (left) (Edwards Lifesciences, 2008) and CoreValve® (right) (CoreValve, 2008) PAVs .....	8
Figure 2-5: PAV after implantation .....	9
Figure 2-6: PAVR implantation technique ( <a href="http://www.ptca.us">http://www.ptca.us</a> ) .....	10
Figure 3-1: Biaxial testing device .....	17
Figure 3-2: Load application setup .....	18
Figure 3-3: Pulley system .....	18
Figure 3-4: SPI interface with the temperature sensor .....	19
Figure 3-5: Electronic circuit for heating element .....	19
Figure 3-6: Pinhole camera model .....	20
Figure 3-7: Four-node quadrilateral element as it appears in different coordinate reference systems .....	23
Figure 3-8: Stress calculation of test spesimen .....	26
Figure 3-9: Picture of test sample before (left) and after (right) digital alteration ....	28
Figure 3-10: Stencil for cutting out test samples .....	29
Figure 3-11: Schematic of fibre orientation and load application .....	29
Figure 3-12: Placement of test sample .....	30
Figure 3-13: Human valve tissue procurement and testing .....	30
Figure 3-14: Calibration object and window .....	31
Figure 3-15: Graphical user interface (GUI) for stress-strain calculations .....	32
Figure 3-16: Picking of markers for node location .....	32
Figure 3-17: Contour plots representing the projections of $W$ against two strain components with the other component set to zero with (d, e, f) and without (a, b, c) the convexity condition imposed. ....	35
Figure 4-1: Nonlinear regression fitting results for the normal stresses .....	37
Figure 4-2: Nonlinear regression fitting results for the shear stresses .....	37
Figure 4-3: Validation of FEA using a load ratio of 2:1 on Bovine sample # 2 .....	38

Figure 4-4: Normal stress FEA and experimental comparison.....	39
Figure 4-5: Shear stress FEA and experimental comparison.....	39
Figure 4-6: Normal stress-strain plots of kangaroo, bovine and human for a load ratio of 1:1 .....	40
Figure 4-7: Shear stress-strain plots of kangaroo, bovine and human for a load ratio of 1:1 .....	40
Figure 5-1: Aortic valve showing a side view of one leaflet (Thubrikar, 1990) .....	42
Figure 5-2: The design and performance parameters of the native aortic valve showing a side view (right) of one leaflet (Thubrikar, 1990).....	43
Figure 5-3: The design and performance parameters of the straight prosthetic valve	45
Figure 5-4: GUI for designing and evaluating a native aortic valve .....	47
Figure 5-5: GUI for designing and evaluating a straight aortic valve .....	47
Figure 5-6: The four different stent designs with measurements .....	48
Figure 5-7: The four different valve designs .....	49
Figure 5-8: Lines of attachment for concepts A and B.....	50
Figure 6-1: Tubular fabrics .....	52
Figure 6-2: Valve attachment methods considered.....	54
Figure 6-3: Suture knots (Troop7, 2008).....	55
Figure 6-4: The leaflet cut-out geometry for concepts A and B.....	56
Figure 6-5: Custom made tweezers for valve assembly .....	56
Figure 6-6: Valve assembly procedures.....	58
Figure 6-7: The three different manufactured valves .....	59
Figure 7-1: Finite element models for concepts A and B .....	61
Figure 7-2: Finite element simulations for concepts A and B under hypertensive pressures.....	61
Figure 7-3: The effects of leaflet material orientation on valve closure.....	62
Figure 7-4: The effects of different leaflet material on valve closure .....	63
Figure 7-5: Over and under dilation of valves.....	65
Figure 7-6: Unsymmetrical dilation of the valve.....	66
Figure 7-7: Attachment forces for concepts A and B .....	67
Figure 7-8: Stress distribution across the valve leaflet.....	68

Figure 8-1: Original and calibrated camera points .....	69
Figure 8-2: Tissue rupture tests .....	70
Figure 8-3: Tearing loads of pericardium for various tissue thicknesses with fibre alignment in the longitudinal and transverse directions .....	71
Figure 8-4: Concept A during pulse duplicator tests showing the systole and diastole .....	72
Figure 8-5: Pressure curves of pulse duplicator tests .....	72
Figure 8-6: Crimping of concepts A and B.....	73
Figure 8-7: In vitro deployment of concept B (left) constructed out of bovine and concept A (right) constructed out of kangaroo in a sheep heart .....	74
Figure 9-1: Hollow punch for cutting out valve leaflets.....	76
Figure A-1: Normal stress-strain relationships for kangaroo tests for ratios of $P_x:P_y = 1:1, 1:2$ and $2:1$ . .....	82
Figure A-2: Normal stress-strain relationships for bovine tests for ratios of $P_x:P_y = 1:1, 1:2$ and $2:1$ .....	83
Figure A-3: Normal stress-strain relationships for human tests for ratios of $P_x:P_y = 1:1, 1:2$ and $2:1$ .....	84
Figure A-4: Shear stress-strain relationships for kangaroo tests for ratios of $P_x:P_y = 1:1, 1:2$ and $2:1$ .....	85
Figure A-5: Shear stress-strain relationships for bovine tests for ratios of $P_x:P_y = 1:1, 1:2$ and $2:1$ .....	86
Figure A-6: Shear stress-strain relationships for human tests for ratios of $P_x:P_y = 1:1, 1:2$ and $2:1$ .....	87

## LIST OF TABLES

Table 4-1: Parameters for the Fung-type elastic constitutive model .....	36
Table 4-2: Strain energy of kangaroo, bovine and human pericardium using the Fung model as well as an isotropic model for comparison.....	41
Table 4-3: Strain energy and von Mises stresses of kangaroo, bovine and human pericardium with their respective thicknesses, using the Fung model and subjected to a load ratio of 1:1 N .....	41
Table 5-1: The design and performance parameters for concepts A and B.....	50
Table 6-1: Size and strength properties of Gore-Tex <sup>®</sup> sutures .....	52
Table 6-2: Physical properties of tubular fabrics.....	53
Table 7-1: Maximum von Mises stresses for various material properties .....	62
Table A-1: Fung parameters for the bovine and kangaroo pericardium samples .....	87

# GLOSSARY & NOMENCLATURE

## GLOSSARY

Annulus	–	A circular or ring-shaped structure.
Calcification	–	The process whereby calcium salts are deposited in an organic matrix.
Cardiovascular	–	Of or pertaining to or involving the heart and blood vessels.
Congenital	–	Existing at or before birth usually through heredity, as a disorder.
Comorbid	–	Existing simultaneously with and usually independently of another medical condition.
Cryopreserve	–	To preserve (cells or tissue, for example) by freezing at very low temperatures.
Embolization	–	The process by which a blood vessel or organ is obstructed by an embolus or other mass.
Endocarditis	–	Inflammation of the endocardium and heart valves.
Haemolysis	–	The destruction or dissolution of red blood cells.
Hypertensive	–	Characterized by or causing high blood pressure.
Hypotensive	–	Having abnormally low blood pressure.
Normotensive	–	Having normal blood pressure.
Paravalvular leak	–	Backflow around the outside of the valve.
Regurgitation	–	Backflow of blood through the valve.
Sclerosis	–	Any pathological hardening or thickening of tissue.
Sheath	–	An enveloping tubular structure that covers a stent or balloon.
Stent	–	Expandable meshed tube used for insertion in a blocked vessel or other part.
Systole	–	The contraction of the chambers of the heart (especially the ventricles) to drive blood into the aorta and pulmonary artery.
Thromboembolism	–	A clot in the blood that forms and blocks a

		blood vessel.
Transcatheter	–	Performed through the lumen of a catheter. Includes the delivery of intravascular devices such as balloon, coils and stents to dilate or close cardiovascular defects.
Transluminal	–	Passing or occurring across a lumen, as of a blood vessel.
Valvuloplasty	–	Use of an intracardiac catheter with an inflatable balloon to dilate stenotic cardiac valves.
Velour	–	A closely napped fabric resembling velvet.
Xenograft	–	Tissue that is transplanted from one species to another (e.g., pigs to humans).

## ABBREVIATIONS

CNC	–	Computer Numerically Controlled
FE	–	Finite Element
FEA	–	Finite Element Analysis
FEM	–	Finite Element Method
GUI	–	Graphical User Interface
PAV	–	Percutaneous Aortic Valve
PAVR	–	Percutaneous Aortic Valve Replacement
PIC	–	Peripheral Interface Controller
POM	–	Polyoxymethylene
PTFE	–	Polytetrafluoroethylene
PWM	–	Pulse Width Modulation
SPI	–	Serial Peripheral Interface

## CONVERSIONS

1 mmHg	=	133.32 Pa
1" (1 inch)	=	25.4 mm
1 French	=	0.333 mm

## CHAPTER 1

### 1. INTRODUCTION

#### 1.1 Background

Conventional heart valve replacement surgery involves making a longitudinal incision in the chest, stopping the heart and placing the patient on cardiopulmonary bypass. Open heart surgery is particularly invasive and requires a lengthy and difficult recovery period which could be fatal for older or terminally ill patients. The percutaneous transcatheter aortic valve replacement involves a minimally invasive technique whereby the valve is placed in position inside the aorta with a catheter through a small insertion in the femoral artery, and expanded into contact with the host annulus by a balloon. The result is a far shorter recovery period and less risk for the patient.

The development of a percutaneous transcatheter aortic valve (PAVR) was initiated in 2007 in the Biomedical Engineering Research Group at Stellenbosch University, and consisted out of three sub-projects, namely the expandable stent design (Esterhuysen, 2008), the simulation of the flow through the aortic valve (Van Aswegen, 2008) and the design and attachment of the tissue leaflets, (this project).

#### 1.2 Objectives

The following objectives were set out for the project:

- Test and use a newly developed processed tissue for the valve leaflets which will be attached to an expandable stent
- Investigate the valve design requirements as well as the current limitations of percutaneous aortic valves
- Develop conceptual models for leaflet geometry and attachment methods
- Conduct numerical simulations in order to analyse the concepts
- Manufacture and test prototypes

#### 1.3 Motivation

Aortic valve stenosis affects up to 20% of the elderly population which accounts for 200 000 surgical aortic valve replacements annually worldwide. About 30% of patients are denied valve replacement due to the risk factors associated with open heart surgery and cardiac bypass which places significant physical stress on the body (Brounstein *et al.*, 2007). The estimated 275 000 to 370 000 annual valve replacements benefit predominantly older patients of developed countries while

developing countries with their much higher incidence of rheumatic fever often have no access to heart surgery (Zilla *et al.*, 2008). Cardiac surgery is only available to 8.1% of the Chinese and 6.9% of the Indian population, compared to European service levels (Zilla *et al.*, 2008). Given the fast growing economics of some of these countries, along with the fact that the improved socio-economic circumstances will only have a delayed impact on reducing the incidence of rheumatic fever, it is predictable that they will soon develop a high demand for prosthetic heart valves that are affordable and that address the specific needs of young patients (Zilla *et al.*, 2008).

Current tissue valves continue to degenerate rapidly in younger patients which make them unsuitable for developing countries (Zilla *et al.*, 2008). Bioprosthetic valves have, however, been tried and tested for quite a long time in comparison to polymeric and tissue-engineered valves. The newly developed processed tissue used in this study has a much higher resistance to calcification and is totally biocompatible which could possibly give rise to a solution for the large market in developing countries.

Percutaneous aortic valve replacement technology is still in an early development and clinical trial phase with a lot of reported issues. Percutaneous aortic valve replacement has the potential of reducing the risks associated with aortic valve replacement and to be less expensive if the procedure is refined and enhanced. If this technology can be improved such that it is reliable enough, it could also be applied to younger patients. This will result in an increase in the market size for these valves.

Improvements on this technology are needed in order to reduce the risks associated with PAVs which would improve the quality of life for many people.

### **1.4 Thesis overview**

Chapter 2 presents the background on the aortic heart valve, its associated diseases and conventional treatments. The PAVR technique and its limitations are discussed which is followed by the valve materials along with the storage and testing solutions used. The chapter ends off with the investigation into the valve design and testing requirements. In Chapter 3 the development of a biaxial testing device is presented to characterize the mechanical behaviour of the materials used. The test protocol and the stress-strain calculations are presented followed by calculation of the material parameters. In Chapter 4 the evaluation and comparison of the materials is performed by implementing finite element analysis and comparing the simulation results with the experimental data. Chapter 5 depicts the valve geometry design and concept development. The manufacturing tools and techniques are demonstrated in Chapter 6. The finite element analysis of the chosen concepts is presented in Chapter 7 whereby various possible scenarios were tested on the two chosen concepts. The experimental testing results are presented in Chapter 8 followed by the conclusions and recommendations made on this study in Chapter 9.

## CHAPTER 2

### 2. LITERATURE REVIEW

#### 2.1 The heart and heart valves

The heart has four chambers (left atrium, left ventricle, right atrium and right ventricle) and four valves (mitral, pulmonary, tricuspid, and aortic valves) as is shown in Figure 2-1. The mitral valve is located between the left atrium and left ventricle, the pulmonary valve between the right ventricle and the pulmonary artery, the tricuspid valve between the right atrium and right ventricle and the aortic valve between the left ventricle and the aorta. The mitral and tricuspid valves are called atrioventricular valves, and the aortic and pulmonary valves are called arterioventricular or also semilunar valves because of the leaflets' half moon shape. The atrioventricular valves are attached to the heart muscle (myocardium) by means of papillary muscles and fibrous cords, and are therefore responding to myocardial contractions. The semilunar valves do not have a direct attachment of the movable part to the myocardium.

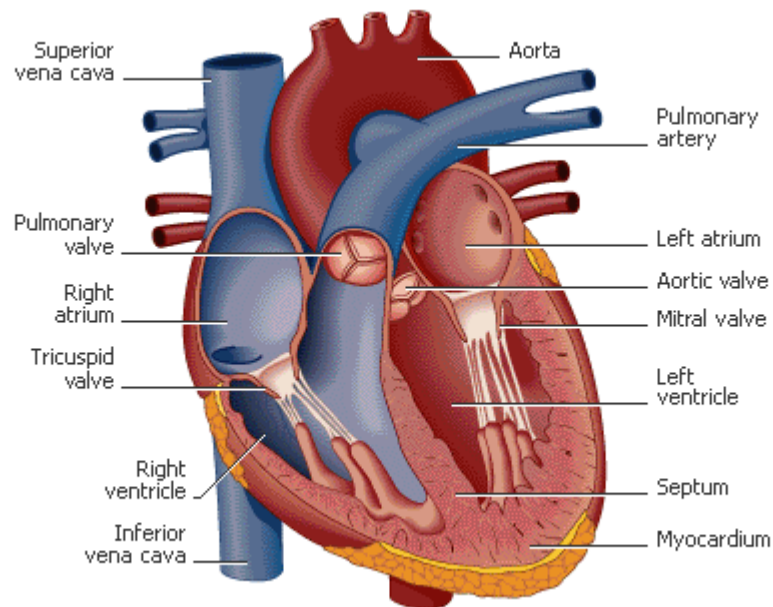


**Figure 2-1: Anatomy of the heart (<http://encarta.msn.com>)**

All the valves only allow blood flow in one direction. The flow of the blood is caused by the rhythmic contractions of the four chambers of the heart. Oxygen-depleted blood returns from the body via the venae cava to the right atrium and via the

tricuspid valve to the right ventricle. The pulmonary valve allows the blood to enter the pulmonary artery towards the lungs. Oxygenated blood from the lungs returns via the pulmonary veins to the left atrium and through the mitral valve to the left ventricle. The aortic valve allows the blood to enter the aorta towards the rest of the body.

## **2.2 The aortic valve**

The aortic valve allows blood to flow into the aorta and prevents backflow into the ventricle. The aortic valve opens and closes approximately 103,000 times per day and 3.7 billion times in its lifespan. Because the aortic valve is located on the high pressure side of the blood transport through the body, it is the heart valve that must endure the highest pressures, fatigue and strains.

## **2.3 Aortic valve disease**

Aortic valve disease is a common clinical problem and is likely to continue to increase with the aging of the population (Kar and Shah, 2006).

Abnormalities of the aortic valve can generally be categorized as involving incompetence of the valve, i.e. aortic regurgitation or insufficiency and obstruction of the valve, i.e. aortic stenosis and sclerosis.

### **2.3.1 Aortic stenosis**

Aortic stenosis can be caused by subvalvular, valvular or supra-ventricular obstruction to the left ventricular outflow. Subvalvular aortic stenosis usually occurs as a fibromuscular membrane or a tunnel-like narrowing of the left ventricular outflow tract. Supra-ventricular aortic stenosis usually occurs due to a congenital narrowing of the ascending aorta, usually beginning just above the sinuses of Valsalva. Valvular stenosis is the most common cause of aortic stenosis and is due to an abnormality of the aortic valve leaflets. The causes of valvular aortic stenosis can be divided into congenital, rheumatic and degenerative stenosis (Ward and Lang, 2006).

Congenital aortic stenosis accounts for the most cases of valvular stenosis in young adults and may be unicuspid, bicuspid or tricuspid. A bicuspid valve is most common in males and accounts for 1-2% of the general population. The two leaflets are usually of unequal size with the larger leaflet generally having a raphe, which may give the appearance of a tricuspid valve. Unicuspid valves produce severe obstruction in infancy and thus are rarely encountered in adults (Ward and Lang, 2006).

Rheumatic aortic valve stenosis is becoming increasingly rare in developed countries, but still has a high incidence in developing countries. Because the mitral valve is

preferentially affected in rheumatic heart disease, certain diagnosis of rheumatic aortic stenosis normally requires related mitral valve stenosis (Ward and Lang, 2006).

Degenerative (or senile calcific) aortic stenosis is the most common in the elderly and accounts for the majority of cases in adults. It normally develops after years of mechanical stress on an originally normal aortic valve. It occurs due to progressive calcium deposition at the leaflet bases, which limits leaflet movement. It is the most common form of aortic stenosis in patients referred for aortic valve replacement (Ward and Lang, 2006).

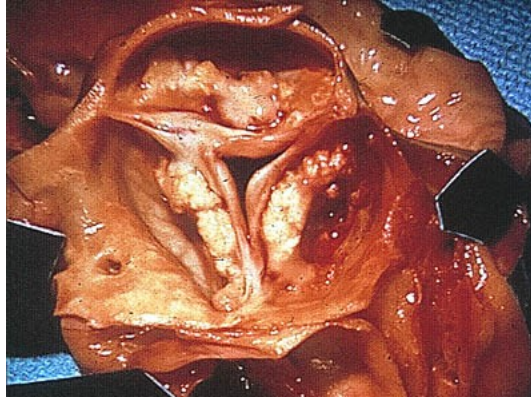


**Figure 2-2: An aortic valve with calcific stenosis (<http://www.pathology.vcu.edu>)**

### **2.3.2 Aortic regurgitation**

Aortic regurgitation occurs when the valve doesn't close properly and blood can leak backward into the left ventricle. The ventricle normally adapts to this abnormality by gradually enlarging to account for the greater workload. Aortic stenosis is one of the main causes of aortic regurgitation. Prosthetic heart valves may in some cases also be relative obstructive while others may have some degree of incompetence from design limitations, unusual patient anatomy and degeneration (Kay and Carroll, 2006).

### **2.4 Aortic valve disease treatment**

The traditional therapeutic approach to symptomatic and severe aortic valve disease has largely involved surgical replacement of the aortic valve. Some other infrequent treatment options involve reconstruction and surgical valvulotomy which is the surgical cutting of a constricted cardiac valve to relief obstruction. The outcome of aortic valve replacement surgery is generally good to excellent. This is often even true for elderly patients, especially when stenosis is the predominant disease and despite the presence of left ventricular dysfunction. However, there are many clinical conditions where surgical intervention in patients with significant aortic valvular disease poses a relatively high risk of morbidity and mortality. As a result of these high risk factors, percutaneous aortic valve replacement has become a considerably

attractive solution or even an alternative for some conventional valvular interventions (Kar and Shah, 2006).

### 2.4.1 Conventional treatments

Aortic valve replacement was made possible due to the cardiopulmonary bypass system and the development of various metallic and bioprosthetic valves. Conventional aortic valve replacement can be subdivided into mechanical, bioprosthetic and biological valve replacements (Figure 2-3).

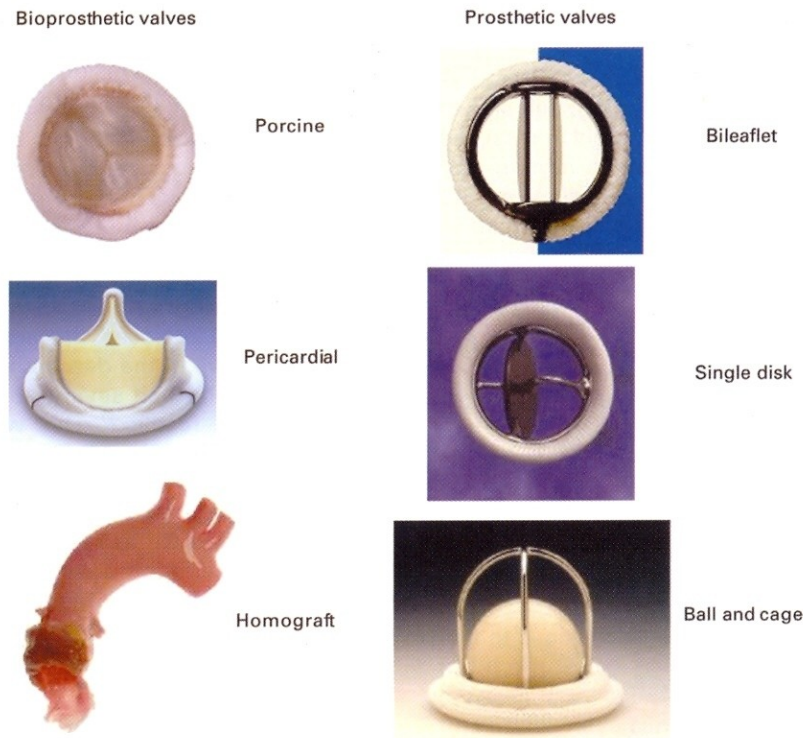


**Figure 2-3: Bioprosthetic and mechanical valves (Shekar *et al.*, 2006)**

There are three types of mechanical valves: ball and cage, tilting disc and bileaflet valves. Mechanical valves have excellent long-term results and freedom from reoperation. A disadvantage however is the need for anticoagulation throughout the life of the valve which in long-term may lead to thromboembolism and hemorrhage. Anticoagulation involves the use of blood thinner medication to prevent blood clotting on the valve. Bioprosthetic valves can be divided into stented and stentless bioprosthetic valves. Stented valves are xenografts derived from animal tissue that have been stented on a semi rigid sewing ring for easier application. The animal tissue is chemically treated or ‘fixed’ with glutaraldehyde. It crosslinks the collagen

fibres and reduces antigenicity. Stentless bioprosthetic valves are a newer generation of xenograft valves which lack the semi rigid sewing ring and commonly have a layer of Dacron<sup>®</sup> along the outside edge.

Bioprosthetic valves do not require anticoagulation, but are susceptible to calcification and currently lasts only about 15 years, after which another surgical intervention may be required. Stented bioprosthetic valves also have a risk of thromboembolism. Stentless porcine valves have a lower gradient at smaller sizes and could therefore aid in reducing load on the left ventricle and assist with ventricular remodelling. Biological valves include homografts that are harvested from human cadavers and cryopreserved. Although not requiring anticoagulation, homografts have long-term problems with calcification and are relatively harder to reoperate on.

Due to years of successes and improvements, conventional treatments became the treatment of choice. Despite all these successes, aortic valve replacement by means of open-heart surgery still has its limitations. The 30-day mortality rate is around 3.1% and the survival rate at five years is around 78%. Normally at follow-up, valve-related complications, including thromboembolism, bleeding from anticoagulation, prosthetic valve endocarditis and even reoperation may occur. Additionally most cases of severe aortic stenosis occur in elderly patients, who often have additional coexisting conditions that increase surgical risk. These include left ventricular failure, coronary artery complications and patients older than 80 years. Younger patients with aortic valve disease often outlive the bioprosthetic valve, requiring reoperations. Although the life expectancy of patients receiving valve replacement is significantly increased, its use in asymptomatic severe aortic valve stenosis is still controversial. The risk of cardiac surgery often outweighs that of intense follow-up and risk stratification of patients with asymptomatic severe aortic valve stenosis. These limitations in surgery dictate the need for low-risk, minimally invasive surgical, or percutaneous techniques (Kar and Shah, 2006).

The development of balloon angioplasty brought forth the use of metallic stents as a common treatment for symptomatic coronary artery disease. Physicians later used the same technique to dilate stenosed aortic, pulmonary, and mitral valves. Aortic valvuloplasty is successful for children and adolescents with congenital aortic valve stenosis, but most elderly and adult patients suffer from degenerative calcific aortic stenosis which makes valve dilation difficult. Although initial improvement occurs, stenosis reoccurrences is as high as 60% within 6-12 months. In most cases a significant residual aortic stenosis still remains. Aortic valvuloplasty is also not an option when significant regurgitation is present. Balloon aortic valvuloplasty in elderly and adult patients is performed infrequently and often only for short-term alleviation. It is however recently more used as part of percutaneous aortic valve replacement.

### 2.4.2 Percutaneous aortic valve replacement (PAVR)

The refinement of balloons and the development of stents in the late 1980s led to the percutaneous approach to aortic valve repair. In 1992, Andersen *et al.* (1992) reported the first case of implementation by the transluminal catheter technique without thoracotomy or extracorporeal circulation. The valve consisted out of a porcine valve mounted on a stent which was implanted in a pig. Percutaneous pulmonary valve replacements using a jugular venous valve mounted in a stent, followed in humans.

In 2002, Cribier *et al.* (2002) reported the first successful implantation of a stent-mounted pericardial valve in a patient with critical aortic valve stenosis. The valve consisted out of three bovine pericardial leaflets mounted within a balloon-expandable stent. Following this initial success, the valve underwent modifications and several companies have developed different types of percutaneous heart valves.

One cardiovascular company called Edwards Lifesciences improved on Cribier's initial design and developed the Edwards SAPIEN transcatheter heart valve, shown in Figure 2-4. The Edwards prosthesis is constructed from a tubular slotted stainless steel stent with an attached trileaflet pericardial valve. A fabric cuff is used to prevent leakage of blood between the stent and the native aortic sinus and covers the left ventricular portion of the prosthesis. The cuff also reduces the stress concentrations near the attachments of the leaflets at the ventricular. The cuff is located on the inside of the stent. Another company called CoreValve<sup>®</sup> developed a valve with a self-expanding Nitinol stent which eliminates the need for balloon expansion. Both valves are currently still undergoing the human trial phase and are not yet available on the market.

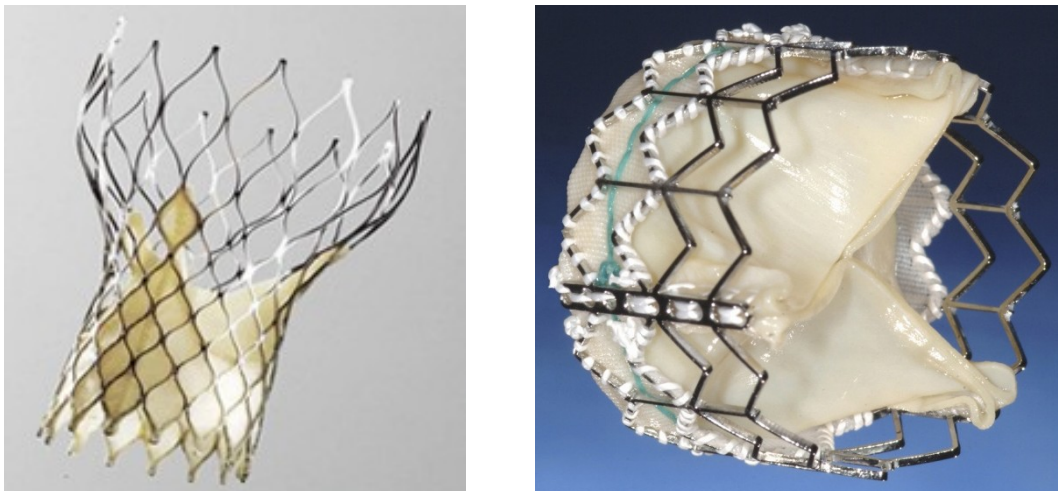


**Figure 2-4: The Edwards Lifesciences (left) (Edwards Lifesciences, 2008) and CoreValve<sup>®</sup> (right) (CoreValve, 2008) PAVs**

### 2.4.3 Current limitations in PAVR

Current designs of percutaneous aortic valve replacements are not yet an acceptable substitute for aortic valve surgery, mostly because of the following limitations:

- The valve needs a large-diameter delivery catheter to contain the crimped valve
- Accurate and secure positioning and deployment is often a challenge
- Blockage of the coronary ostia
- Migration of the valve after implantation
- Post-deployment paravalvular leak is common
- Severe aortic regurgitation might cause interference of the coronary ostium
- Temporary circulatory support might be needed to assure careful and accurate deployment
- Subsequent surgical replacement of a malfunctioning percutaneous valve could be challenging due to the size of some valves that results in a large section to be cut out
- Calcification of the leaflets
- Regurgitation due to irregular expansion

The final position of the valve after implantation relative to the surrounding physiological regions is shown in Figure 2-5.

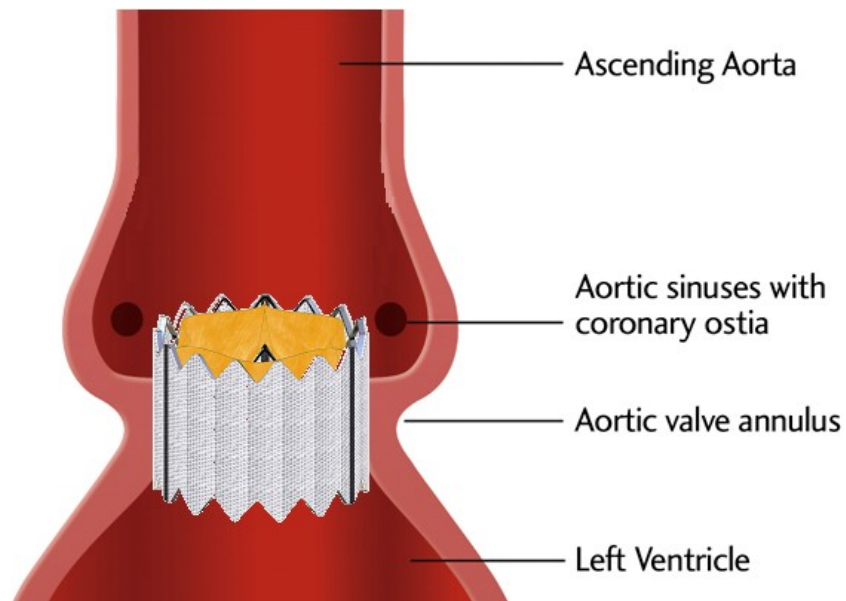


**Figure 2-5: PAV after implantation**

Despite these limitations, severely symptomatic patients for whom it is considered high risk to undergo surgery because of comorbidity or poor ventricular function, are considered potential candidates for percutaneous valve replacement. It is conceivable that with refinements in valve design, delivery, deployment and improvement in valve durability, the percutaneous valve replacement may well develop into a viable alternative to surgery. This may later even include average to low-risk patients.

#### 2.4.4 PAVR technique

A sheath of roughly 22F (8 mm external diameter) to 24F (9 mm external diameter) is placed from the femoral artery to the aorta with the patient sedated but conscious. A catheter with a guide wire facilitates manipulation of the prosthesis around the aortic arch and through the damaged native valve with the guidance of fluoroscopy. Rapid ventricular pacing is used to reduce cardiac output and ease the insertion. A delivery balloon is inflated to deploy the prosthesis within the annulus (Webb *et al.*, 2006). The procedure takes less than an hour and recovery takes normally one to two days. The implantation technique is shown in Figure 2-6.

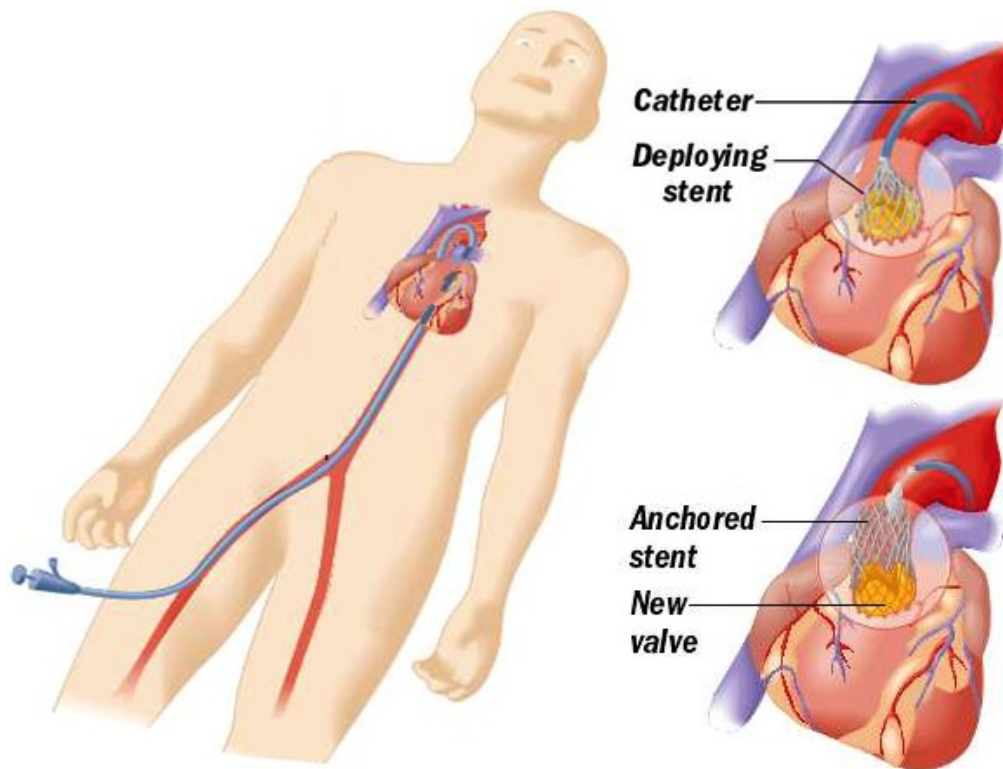


Figure 2-6: PAVR implantation technique (<http://www.ptca.us>)

## 2.5 Valve material and treatment

### 2.5.1 Conventional materials

Mechanical heart valves are essentially made out of metal and other engineering materials. The struts and occluders are made out of either pyrolytic carbon or pyrolytic carbon coated titanium, and the sewing ring cuff is made out of Teflon<sup>®</sup> (PTFE), polyester or Dacron<sup>®</sup>. Percutaneous heart valve stents are generally made out of stainless steel, cobalt-chrome or Nitinol. The latter is generally used for self-expandable stents.

Bioprosthetic aortic valves are normally constructed out of complete porcine aortic valves or animal tissue, such as bovine pericardium, that is used to construct the leaflets. The pericardium is the fluid-filled sac that surrounds the heart and the proximal ends of the aorta, vena cava, and the pulmonary artery. There have been three generations of improved bioprosthetic valve treatment processes. The first-generation valves are high-pressure pre-fixation valves, such as the Medtronic Hancock I. The second-generation valves are treated with low- or zero-pressure fixation which includes the Medtronic Hancock II valve and the Carpentier-Edwards Supra-Annular valve. The third-generation valves are subjected to an antimineralization process, in addition to low to zero-pressure fixation like the Medtronic Mosaic porcine valve. This process is designed to reduce material fatigue and calcification (Shekar *et al.*, 2006).

Percutaneous aortic valves are generally tricuspid bioprosthetic valves of which the leaflets are made from animal tissue.

### 2.5.2 Material used for this study

The material used for this study is bovine and kangaroo pericardium. The material was provided by BioMD Limited which is a medical device and surgical technology company based in Perth, Australia. Celxcel, which is one of BioMD's subsidiary companies, have developed a new anticalcific treatment called ADAPT<sup>™</sup>.

The ADAPT<sup>™</sup> process is an antimineralization process based on a multifactorial approach focused on synchronized synergy between enhanced crosslink stability, removal of residual glutaraldehyde, modification of non-bifunctionally reacted glutaraldehyde residues, reduction of the lipid content and restoration of tissue elasticity (Neethling *et al.*, 2004). The process prevents calcification of glutaraldehyde treated collagen and proves to be better than conventional anticalcific treatments.

In 2002, Neethling *et al.* (2002) reported that kangaroo pericardium has a densely arranged collagen matrix with a higher extensibility and significantly lower calcification potential than bovine pericardium. It can be noted that the material in their study did not undergo the ADAPT™ treatment.

## 2.6 Material storage and testing solutions

As pericardium is a tissue-derived biomaterial, it is susceptible to bacterial decay and degeneration. Chemically treated pericardium is more resistant to decay and may remain stable for up to five days without antibiotic treatment, depending on the surrounding environment.

Tissue prepared for experimental use is stored in 70% ethanol or 20% isopropanol. For clinical use, the tissue is stored in propylene glycol. Before use the material must undergo rehydration in a 0.9% NaCl (saline) solution for twenty minutes.

During fatigue tests in a pulse generator a volume-based solution of 42% glycerol and 58% water is used as the testing fluid. 0.9 wt.% NaCl is then added to the solution. If antibiotics are added for preservation, the solution must preferably be replaced every seven days. The preferred antibiotic is Tetracycline. Alternatively a 0.5% glutaraldehyde buffered solution may be used as the basis solution with glycerol added for viscosity. No antibiotics are needed for this solution (Neethling, 2008).

## 2.7 Valve design requirements

The valve design requirements can be split into quantifiable and non-quantifiable requirements of which some are provided by the ISO standards for conventional heart valve prostheses (International Organization for Standardization, 2005):

Quantifiable:

- An external valve diameter of 20 mm for in vivo testing in sheep
- A maximum valve height of 16 mm
- A maximum valve crimping diameter of 18 French (6 mm)
- Able to withstand a maximum pressure of 230 mmHg across the valve during diastole.

Non-Quantifiable:

- Allow forward flow with acceptably small mean pressure difference
- Prevent retrograde flow with acceptably small regurgitation and paravalvular leak
- Resist embolization
- Resist haemolysis
- Resist thrombus formation

- Is biocompatible
- Is compatible with in vivo diagnostic techniques
- Is deliverable and implantable in the target population
- Remain fixed once placed
- Has an acceptable noise level
- Has reproducible function
- Maintain its functionality for a reasonable lifetime
- Maintain its functionality and sterility for a reasonable shelf life prior to implantation

These design requirements were used as guidelines during the valve development and evaluation.

## **2.8 Valve testing**

Preclinical testing of PAVRs can be broken down into three main areas: evaluation of device hydrodynamic function, device durability/life cycle and device biocompatibility/host response (Lemmon, 2006).

Hydrodynamic testing is used to evaluate the function of heart valve replacements under a range of physiologic conditions. It is typically conducted in a pulse duplicator with typical heart rates of 45-150 beats/min and cardiac outputs of 2-10  $\ell$ /min. Measurements of pressure drop, effective orifice area and regurgitant flow volume are normally taken. Normal to hypertensive pressures across the valve are tested. Additional measurements can be taken to assess laminar and turbulent flow regions as well as areas with stagnant flow that could lead to thrombus formation. This flow visualization can be performed by using a laser light sheet illuminating a test solution seeded with small glass or plastic particles. Laboratory tests also have the benefit of calculating the shear stresses in the flow field and thus evaluate the potential damage to blood elements. Velocities through the valve can be measured by using Doppler ultrasound.

Failure mode analysis is a durability analysis with the purpose of determining whether failure is catastrophic or degenerative. Damage is caused to the valve by increasing the cycle rate whereas overloading will reveal the weaker components that will fail first. Biological PAVs can fail due to leaflet prolapse, leaflet abrasion, valve dehiscence from the stent, stent migration and stent fracture. Accelerated wear testing is in the ranges of 10-20 times the physiologic cycle rates which allow clinical cycles of five years to be achieved in 5-6 months. This testing is performed under normal pressures. Biological valves need to be evaluated over 200 million cycles which represent five years of clinical implantation.

The final verification testing prior to clinical trials is to perform animal studies. Biocompatibility testing provides data on inflammation, irritation, cytotoxicity, etc.

of the device. Chronic animal studies are done to test the host response at the implant site, device histology and hemodynamic function of the valve (Lemmon, 2006).

## 2.9 Recent research

Many physiological, surgical, and medical device applications exist where rigorous constitutive modelling and numerical simulations are required due to the complex mechanical behaviour of the tissues used (Sun and Sacks, 2005). Soft tissues possess highly nonlinear stress-strain relationships, large deformations and mechanical anisotropy. Although finite element analysis (FEA) has been commonly used for structural analysis of heart valves, the material models used were generally simplified models. These models can be divided into four groups: linear anisotropic, nonlinear isotropic, linear anisotropic and nonlinear anisotropic (Kim *et al.*, 2006). Burriesci *et al.* (1999) reported that even a small amount of anisotropy can significantly affect the mechanical behaviour of the valve. Arcidiacono *et al.* (2005) suggested that leaflets of pericardium bioprosthetic valves could be manufactured to be similar to natural human heart valves, reproducing their well-known anisotropy. In this way it could be possible to improve the durability and function of pericardial bioprosthetic valves. It is therefore clear that both nonlinearity and anisotropy should be taken into consideration for the finite element analysis of bioprosthetic heart valves. Sun *et al.* (2005) employed the Fung-type elastic material model in a quasi-static analysis. They used rigorous experimental validation and found that the utilization of actual leaflet material properties is essential for accurate bioprosthetic heart valve simulations. Kim *et al.* (2006) conducted a dynamic simulation of a pericardial bioprosthetic heart valve during the opening phase of the valve by implementing the Fung-type elastic material model. It is known that the highest stresses occurs during the closing phase (diastole) of the valve, which is one of the main causes of valve failure. Currently no literature has been found that implement the Fung-type elastic material model during the closing phase of the valve.

The geometric modeling of the aortic leaflet and the aortic valve in general has received considerable attention (Labrosse *et al.*, 2006). Thubrikar (1990) explored the design of aortic valves to ensure optimal performance whereby geometric criteria were defined to guarantee appropriate sealing of the leaflets, minimize the dead space, eliminate folds in the leaflets and minimize leaflet flexion. Labrosse *et al.* (2006) established a method to determine by how much the dimensions of the aortic valve components can vary while still maintaining proper function. This may aid in the examination of “what-if” scenarios in aortic valve design and valve-sparing operations.

## CHAPTER 3

### 3. MATERIAL PROPERTIES

In order to perform finite element analysis (FEA) on the valve, the mechanical behaviour of the pericardium under a generalized loading state needs to be defined. To achieve this, rigorous experimentation involving all relevant deformations is necessary to obtain the material constants and the strain-energy density function that describes the material behaviour of the pericardium.

The pericardium consists partially out of collagen fibres which are integrated with cells and intercellular substances. Sections in which the fibres are predominantly aligned in one direction are used for testing and manufacturing the prostheses. The fibre direction normally possesses tougher mechanical properties. In native aortic valves these fibres are mostly aligned in the circumferential direction under pressure (Sacks *et al.*, 1998). Biological tissues are generally considered incompressible (Fung, 1993), which means that planar testing allows for a two-dimensional stress-state that can be used to fully characterize its mechanical behaviour.

#### 3.1 The constitutive equation of skin

Accurate numerical simulations of the mechanical properties of soft biological tissues remain a challenge due to the fact that most soft biomaterials are nonlinear orthotropic. Consequently, tissues are assumed to be isotropic, nonlinear isotropic or orthotropic for simulation purposes. The constitutive equation proposed by Fung (1993) provides one of the most accurate material behaviour predictions for soft tissues. Although this model is widely used in the literature for characterization of experimental data, it is rarely implemented in finite element simulations (Sun and Sacks, 2005). The main reasons are numerical instability and convergence problems. Fung proposed the following form for the pseudo-strain-energy function for skin:

$$\begin{aligned} \rho_0 W = & \frac{1}{2} (\alpha_1 E_1^2 + \alpha_2 E_2^2 + \alpha_3 E_{12}^2 + \alpha_3 E_{21}^2 + 2\alpha_4 E_1 E_2) \\ & + \frac{1}{2} c \exp (\alpha_1 E_1^2 + \alpha_2 E_2^2 + \alpha_3 E_{12}^2 + \alpha_3 E_{21}^2 + 2\alpha_4 E_1 E_2 \\ & + \gamma_1 E_1^3 + \gamma_2 E_2^3 + \gamma_4 E_1^2 E_2 + \gamma_5 E_1 E_2^2) \end{aligned} \quad (1)$$

where  $W$  is the strain energy per unit mass of the tissue and  $\rho_0$  is the density (mass per unit volume) in the zero-stress state which makes  $\rho_0 W$  the strain energy per unit volume of the tissue in the zero-stress state. The  $\alpha$ 's,  $a$ 's,  $\gamma$ 's and  $c$  are constants and  $E_{ij}$  is the Green strain tensor. The rate of the Green strain tensor is conjugate in power

(energy) to the second Piola-Kirchoff (PK2) stress (Belytschko *et al.*, 2000). The PK2 stress tensor,  $S_{ij}$ , is derived from the strain energy function  $W$ :

$$S_{ij} = \frac{\partial W}{\partial E_{ij}} \quad (2)$$

Sun and Sacks (2005) implemented the following simplified Fung model with full expansion of quadratic terms to account for in-plane shear strains:

$$W = \frac{c}{2} [e^Q - 1] \quad (3)$$

where

$$Q = A_1 E_{11}^2 + A_2 E_{22}^2 + 2A_3 E_{11} E_{22} + A_4 E_{12}^2 + 2A_5 E_{12} E_{11} + 2A_6 E_{12} E_{22} \quad (4)$$

and  $c$  and  $A_i$  are material constants. Although *equation 3* is a simplified version of *equation 1*, it is still accurate in the higher stress and strain ranges (Fung, 1993). *Equation 3* is implemented in this study because of its relative simplicity and fewer constants.

### 3.2 Biaxial testing device

In order to determine the material constants for *equation 3*, a device was needed to measure the stress-strain relationships in various load configurations. A biaxial testing device was constructed and used to determine the material constants for the simplified Fung model. The device had the following design criteria:

- Apply independent biaxial loads to the sample being tested
- Measure the deformation of the sample without influencing the load measurements
- The tissue being tested must be maintained under simulated body conditions during the testing
- The device should allow the test specimen to shear freely (Sacks, 2000)

The device can be seen in Figure 3-1. The device consists out of a support structure which contains an attachment for a digital camera for optical strain measurement and linear adjustable slides with load cells for load measurement. A Canon PowerShot A620 digital camera with a resolution of 3072 x 2304 pixels was used in these tests. A special pulley system was attached to the load cells to allow for in-plane shear of the test sample. A tub with a heating element was used to maintain the 0.9% NaCl (saline) testing solution at a constant temperature of 37 °C, simulating body temperature.

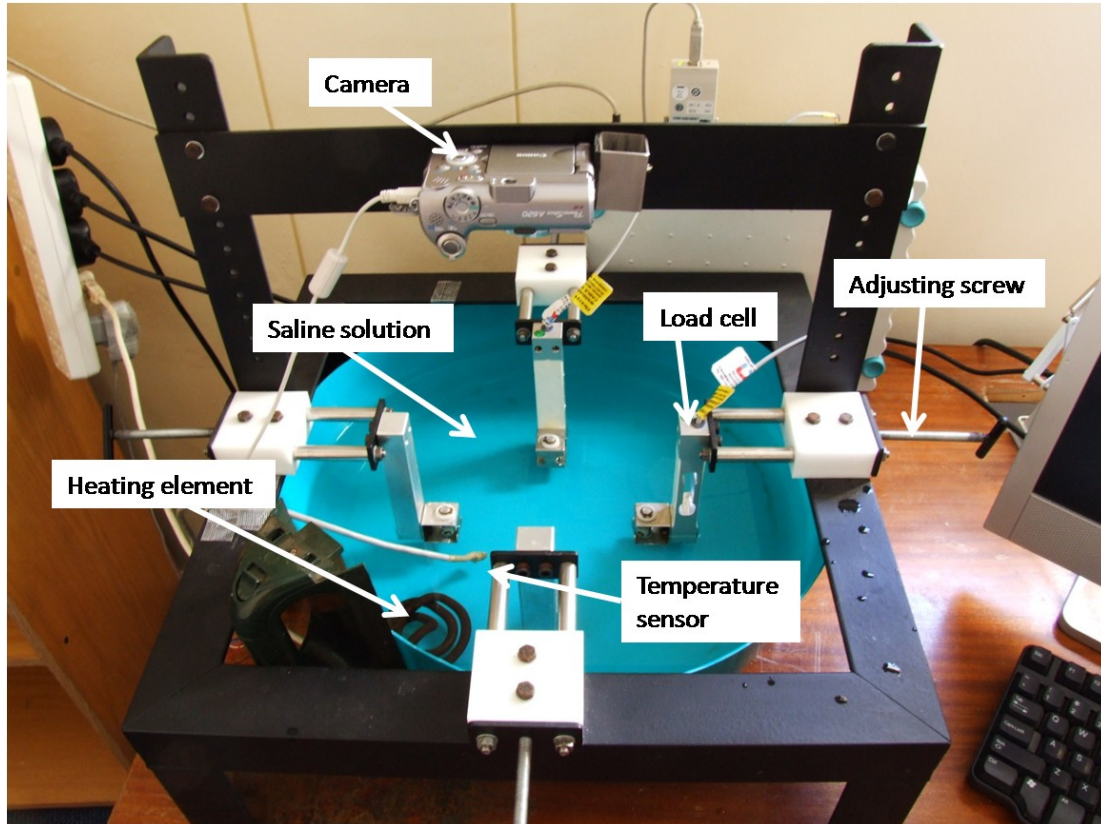


**Figure 3-1: Biaxial testing device**

### 3.2.1 Load Application and Capturing

To determine the stress-strain curves of the test sample, the loads applied needed to be determined and adjusted. Two PW6CMR/20KG load cells from HBM were used to determine the loads applied to the test sample in the x and y directions. These single point load cells compensate for off-centre loads. The length of the load cell makes it ideal for this application due to the fact that the test sample needs to be submerged in the saline solution. A HBM Spider8 bridge amplifier was used to capture the loading data. An adjusting screw and linear slide setup were designed to adjust the applied loads. The linear slide setup consisted of an acetal (POM) housing with two polished stainless steel shafts sliding through it. A brass bush was mounted in the housing. The loading screw fits into the bush. A manually operated loading screw was used to generate the linear movement. The load application setup can be seen in Figure 3-2.

### 3.2.2 Pulley System

The main purpose of the pulley system is to allow the test sample to shear freely during loading. The setup consists of two acetal pulleys mounted on a horizontal shaft

what passes through a vertical shaft. The vertical shaft is supported by a square tube section and acetal bushes for free movement. Both shafts are kept in place by means of circlips. The shafts as well as the square tube section were manufactured from stainless steel. The pulley system can be seen in Figure 3-3.

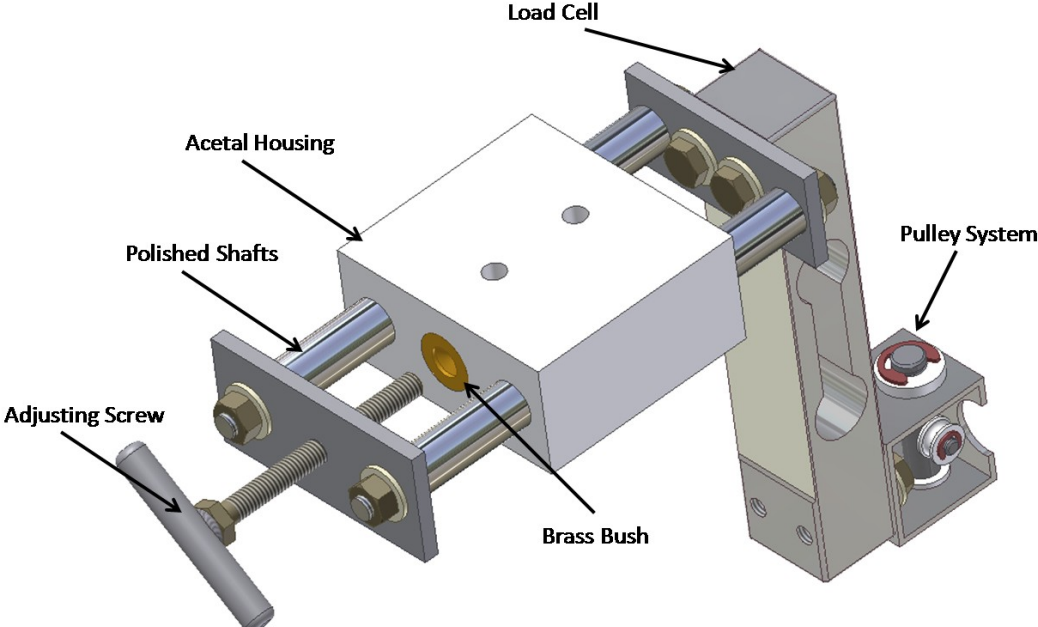


Figure 3-2: Load application setup

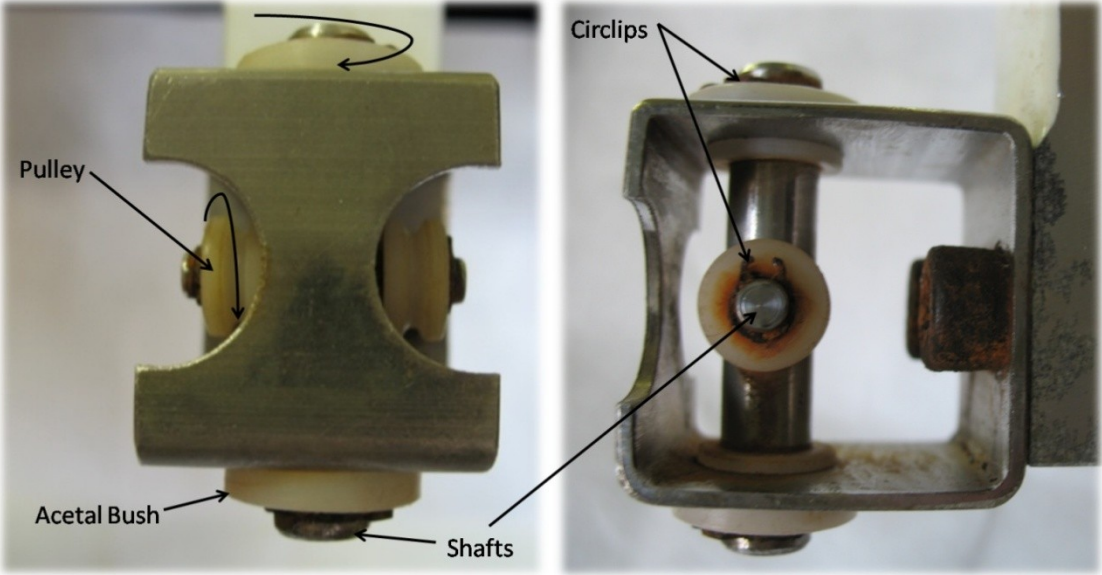


Figure 3-3: Pulley system

### 3.2.3 Temperature control

The material properties of the tissue need to be measured at a constant human body temperature of 37 °C. An electronic circuit was designed to keep the saline solution at a constant temperature. A PIC 18F2550 microcontroller was used to control a 2 kW heating element which was submerged in the saline solution. An ADT7301 digital temperature sensor from Analog Devices was used to measure the temperature. The sensor was sealed with glue and submerged in the solution near the test sample. The two devices communicated via SPI protocol rather than analog signals to eliminate electrostatic noise. The SPI interface can be seen in Figure 3-4. The heating element was controlled using pulse width modulation (PWM) with a frequency of 1 Hz. The following exponential function was used to control the duty cycle (DS):

$$DS = 1 - e^{-C(T-37)} \tag{5}$$

where  $C$  is a calibration constant and  $T$  is the measured temperature in °C.

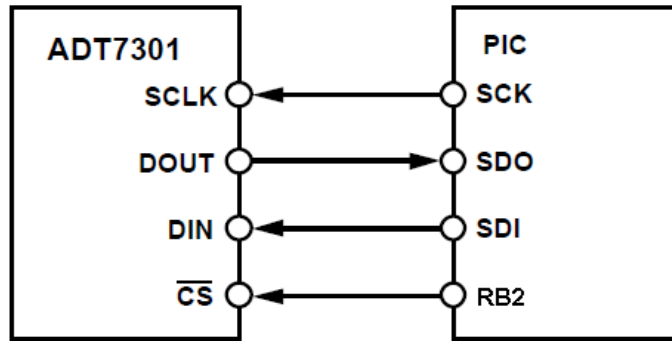


Figure 3-4: SPI interface with the temperature sensor

The heating element was powered by a BT139 triac which was driven by a MOC3041 optoisolator as can be seen in Figure 3-5. A heat sink was attached to the triac to dissipate the heat generated.

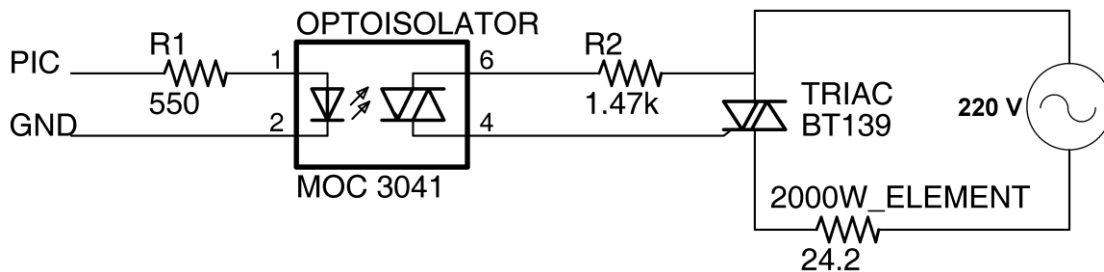


Figure 3-5: Electronic circuit for heating element

The temperature value was sent to the computer each second via serial port and accessed using HyperTerminal. The calibration constant  $C$  could also be changed by using the keyboard. A value of 0.5 for  $C$  proved to be adequate. This simple control proved to be adequate with almost no temperature overshoot if taken into consideration that the testing solution was kept motionless.

### 3.3 Camera calibration

Camera lens distortion is present in almost every camera and may contribute to optical errors during strain measurements. The following calibration technique was adopted from Van der Merwe, (2008).

#### 3.3.1 The camera model

The pinhole camera is the simplest camera model and is used as a basis for camera calibration methods. In this model, illustrated in Figure 3-6, a point  $P$  in the world coordinate system is projected onto the image plane as point  $p$ . The image point  $p$  lies on the intersection between a straight line connecting  $P$  with the centre of projection,  $C$  and the image plane. The principle point or image centre is located at  $c$  and  $Z$  is the optical axis or axis of camera reference frame. The distance  $f$  from  $C$  to  $c$  is called the focal length.

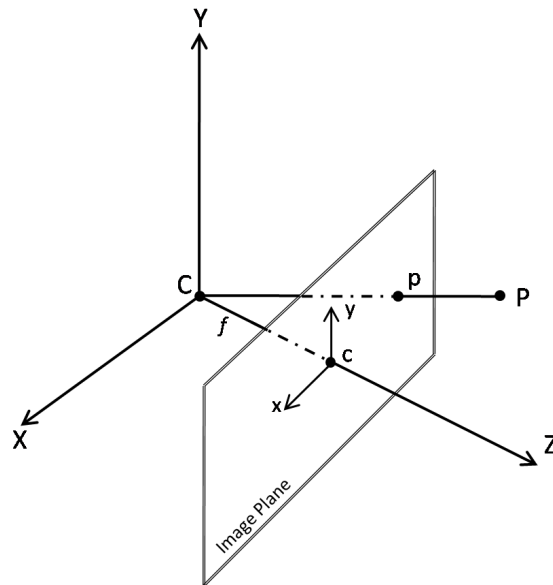


**Figure 3-6: Pinhole camera model**

The world  $(x_p, y_p, z_p, 1)^T$  and image coordinates  $(x_i, y_i, 1)^T$  can be related by:

$$\begin{bmatrix} x_i \\ y_i \\ 1 \end{bmatrix} = \begin{bmatrix} f & 0 & p_x \\ 0 & f & p_y \\ 0 & 0 & 1 \end{bmatrix} \begin{bmatrix} 1 & 0 & 0 & 0 \\ 0 & 1 & 0 & 0 \\ 0 & 0 & 1 & 0 \end{bmatrix} \begin{bmatrix} x_p \\ y_p \\ z_p \\ 1 \end{bmatrix} \quad (6)$$

$$\mathbf{x} = \mathbf{K}[\mathbf{I}|\mathbf{0}]\mathbf{X}$$

where  $\mathbf{K}$  is called the calibration matrix and  $p_x$  and  $p_y$  are the positive distances from the image origin to the principle point,  $c$ .

The calibration matrix describes the internal geometry of the camera and contains the intrinsic parameters. These parameters stay constant if the camera goes through an arbitrary translation and rotation.

The calibration matrix for a digital camera for which the pixel elements have been taken into account is as follows:

$$\mathbf{K} = \begin{bmatrix} \alpha_x & s & x_0 \\ 0 & \alpha_y & y_0 \\ 0 & 0 & 1 \end{bmatrix} \quad (7)$$

where the focal length terms become  $\alpha_x = fm_x$  and  $\alpha_y = fm_y$  and the principle offset values become  $x_0 = m_x p_x$  and  $y_0 = m_y p_y$ . The  $m_x$  and  $m_y$  values are the pixel width and height, respectively, given in the number of pixels per metric unit. In most digital cameras the pixels are nearly square. The skew parameter  $s$  compensates for pixels that do not form square angles. In most cases the skew factor is set to zero.

If the world coordinate frame does not fall on the camera coordinate frame, a translation and rotation is needed to transform the world coordinate frame to the camera coordinate frame. The rotation matrix,  $\mathbf{R}$ , and the camera centre,  $\mathbf{C}$ , relate the camera position and orientation to the world coordinate frame. The final relation between the world and image coordinates is as follows:

$$\begin{bmatrix} x_i \\ y_i \\ 1 \end{bmatrix} = \begin{bmatrix} \alpha_x & 0 & x_0 \\ 0 & \alpha_y & y_0 \\ 0 & 0 & 1 \end{bmatrix} \begin{bmatrix} r_{11} & r_{12} & r_{13} \\ r_{21} & r_{22} & r_{23} \\ r_{31} & r_{32} & r_{33} \end{bmatrix} \begin{bmatrix} 1 & 0 & 0 & -x_c \\ 0 & 1 & 0 & -y_c \\ 0 & 0 & 1 & -z_c \end{bmatrix} \begin{bmatrix} x_p \\ y_p \\ z_p \\ 1 \end{bmatrix} \quad (8)$$

$$\mathbf{x} = \mathbf{KR}[\mathbf{I} - \mathbf{C}]\mathbf{X}$$

The camera matrix follows as:

$$\mathbf{P} = \mathbf{KR}[\mathbf{I} - \mathbf{C}] \quad (9)$$

where

$$\mathbf{x} = \mathbf{PX} \quad (10)$$

### 3.3.2 Lens distortion model

Radial distortion by camera lenses is one of the main causes of deviation from the pinhole camera model to the digital camera model. There are mainly two types of radial distortion, namely pincushion and barrel distortion. Pincushion distortion causes the straight edges of an image to curve inwards and barrel distortion causes the edges to curve away from the radial centre. The undistorted image coordinate,  $\mathbf{x}_u$ , is computed by adding the corrected distances to the centre of radial distortion,  $\mathbf{c}$ , as shown in *equation 11*.

$$\mathbf{x}_u = \mathbf{c} + f(r)(\mathbf{x}_d - \mathbf{c}) \quad (11)$$

The correction function,  $f(r)$ , is a function of the absolute Euclidean distance,  $r$ , from the radial centre,  $\mathbf{c}$ , to the distorted image coordinate,  $\mathbf{x}_d$ , and is calculated as follows:

$$f(r) = 1 + k_1 r + k_2 r^3 \quad (12)$$

where  $k_1$  and  $k_2$  are the distortion correction parameters to be optimized and  $r$  is calculated by:

$$r = \|\mathbf{x}_d - \mathbf{c}\| \quad (13)$$

### 3.3.3 Calibration technique

Van der Merwe (2008) implemented a two-step calibration method. In the first step, the camera matrix,  $\mathbf{P}$ , is determined using a linear method which ignores non-linear effects such as lens distortion. The second step introduces the non-linear effects of lens distortion with the model described above.

In calculating the camera matrix,  $\mathbf{P}$ , and thus the point correspondences  $x_i \leftrightarrow x_i'$ , the Direct Linear Transformation (DLT) method was used which calculates a matrix,  $\mathbf{H}$ , such that  $x_i \mathbf{H} = x_i'$  for each point  $i$ . For practical implementation of the solution, the linear system first needs to be preconditioned or by scaling and shifting both the image and world coordinates. The DLT algorithm calculates a normalized camera matrix, whereafter the matrix is denormalised to retrieve the final camera matrix.

In the second step the values from the camera matrix, a set of known world-coordinates and a set of image coordinates are used to minimize the lens distortion error. The back-projection error, or the difference between the calibration-feature coordinates extracted from the image and the back-projection of the world coordinates onto the image plane, needs to be minimized. The camera matrix determined in the first step is used along with *equation 11* to project a known world coordinate onto the image plane of the camera. The projected coordinate is then compared with the corresponding coordinate extracted directly from the image. The Euclidean distance between the two coordinates is used as an output to be minimized

and is called the back-projection error. Van der Merwe minimized a collection of coordinate errors calculated by adding the mean and standard deviation of the error-set.

A picture of a calibration object is taken each time the camera is moved or placed onto the testing rig and a new calibration is performed. The optimized distortion coefficients and camera matrix are then used to calibrate each image corresponding to an applied load.

### 3.4 Strain calculation

When simulating hypoelastic materials large strains are common and thus need to be taken into account. Mathematics used in finite element methods is applied to the displacements measured optically to yield a solution for the components of plane strain at the nodes as proposed by Hoffman and Grigg, (1984).

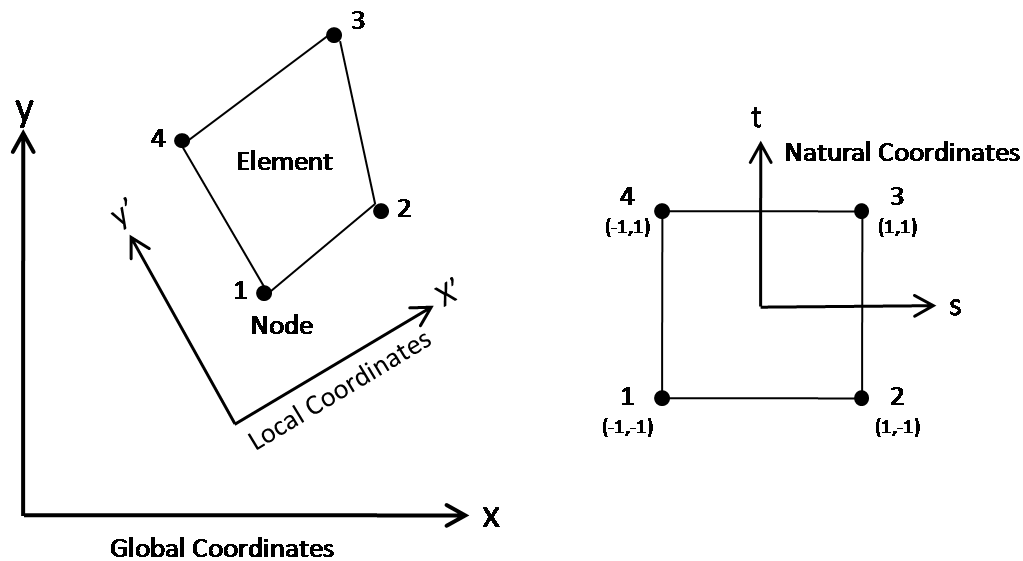


**Figure 3-7: Four-node quadrilateral element as it appears in different coordinate reference systems**

The markers in this method are treated as the nodes of a four-node finite element with no constraints placed on them. This allows for shear and normal strains to be calculated. Finite element interpolation functions are used to calculate the strain components.

Three coordinate systems are used in this method where the first is a global coordinate system that is fixed in space and is the reference frame for the entire continuum. The global coordinate system  $(x, y)$  corresponds to the coordinate system of the digital camera. The second coordinate system is local,  $(x', y')$  and is the

reference frame for the element. The third coordinate system is the natural coordinate system  $(t,s)$  and is a transformation dimensionless system in which the element appears as a square with nodal coordinates of unity. The representation of the four-node quadrilateral element and the different coordinate reference systems can be observed in Figure 3-7.

The geometry of the element can be expressed as:

$$x = \sum_{i=1}^4 N_i x_i \quad (14a)$$

$$y = \sum_{i=1}^4 N_i y_i \quad (14b)$$

where  $(x_i, y_i)$  are the nodal coordinates in the global coordinate system. The horizontal and vertical displacement components of the element can be expressed as:

$$u = \sum_{i=1}^4 N_i u_i \quad (15a)$$

$$v = \sum_{i=1}^4 N_i v_i \quad (15b)$$

where  $(u_i, v_i)$  are the nodal displacements and  $N_i$  are the interpolation functions given in terms of  $s$  and  $t$  by:

$$\begin{aligned} N_1 &= \frac{(1-s)(1-t)}{4} \\ N_2 &= \frac{(1+s)(1-t)}{4} \\ N_3 &= \frac{(1+s)(1+t)}{4} \\ N_4 &= \frac{(1-s)(1+t)}{4} \end{aligned} \quad (16)$$

The locations  $(x_i, y_i)$  and the displacements  $(u_i, v_i)$  of the element nodes are determined optically. The location  $(x, y)$  and displacements  $(u, v)$  of any point within the element (including the nodes) are calculated using the interpolation functions given by equations 14 to 16. The same interpolation functions are used to describe the element's displacement field as well as its geometry which is why it is called a four

node isoparametric element. The partial derivatives of the displacement components with respect to  $s$  and  $t$  using the chain rule are given by:

$$\begin{bmatrix} \frac{\partial u}{\partial s} \\ \frac{\partial u}{\partial t} \end{bmatrix} = \begin{bmatrix} \frac{\partial x}{\partial s} & \frac{\partial y}{\partial s} \\ \frac{\partial x}{\partial t} & \frac{\partial y}{\partial t} \end{bmatrix} \begin{bmatrix} \frac{\partial u}{\partial x} \\ \frac{\partial u}{\partial y} \end{bmatrix} \quad (17a)$$

$$\begin{bmatrix} \frac{\partial v}{\partial s} \\ \frac{\partial v}{\partial t} \end{bmatrix} = \begin{bmatrix} \frac{\partial x}{\partial s} & \frac{\partial y}{\partial s} \\ \frac{\partial x}{\partial t} & \frac{\partial y}{\partial t} \end{bmatrix} \begin{bmatrix} \frac{\partial v}{\partial x} \\ \frac{\partial v}{\partial y} \end{bmatrix} \quad (17b)$$

The partial derivatives of  $u$  and  $v$  with respect to  $x$  and  $y$  are determined by inverting the above relations and are given by:

$$\begin{bmatrix} \frac{\partial u}{\partial x} \\ \frac{\partial u}{\partial y} \end{bmatrix} = \frac{1}{|J|} \begin{bmatrix} \frac{\partial y}{\partial t} & -\frac{\partial y}{\partial s} \\ -\frac{\partial x}{\partial t} & \frac{\partial x}{\partial s} \end{bmatrix} \begin{bmatrix} \frac{\partial u}{\partial s} \\ \frac{\partial u}{\partial t} \end{bmatrix} \quad (18a)$$

$$\begin{bmatrix} \frac{\partial v}{\partial x} \\ \frac{\partial v}{\partial y} \end{bmatrix} = \frac{1}{|J|} \begin{bmatrix} \frac{\partial y}{\partial t} & -\frac{\partial y}{\partial s} \\ -\frac{\partial x}{\partial t} & \frac{\partial x}{\partial s} \end{bmatrix} \begin{bmatrix} \frac{\partial v}{\partial s} \\ \frac{\partial v}{\partial t} \end{bmatrix} \quad (18b)$$

where  $|J|$  is the magnitude of the Jacobian Matrix and is given by:

$$|J| = \frac{\partial x}{\partial s} \frac{\partial y}{\partial t} - \frac{\partial x}{\partial t} \frac{\partial y}{\partial s} \quad (19)$$

The deformation gradient tensor,  $\mathbf{F}$ , completely describes the deformation state of the element and is given by:

$$\mathbf{F} = \begin{bmatrix} \frac{\partial u}{\partial x} & \frac{\partial u}{\partial y} \\ \frac{\partial v}{\partial x} & \frac{\partial v}{\partial y} \end{bmatrix} + \begin{bmatrix} 1 & 0 \\ 0 & 1 \end{bmatrix} = \begin{bmatrix} \lambda_1 & \kappa_1 \\ \kappa_2 & \lambda_2 \end{bmatrix} \quad (20)$$

The determinant of  $\mathbf{F}$ ,  $\det(\mathbf{F})$ , is denoted by  $J$  and is called the Jacobian determinant or the determinant of the deformation gradient.

Soft tissues are comprised primarily of water and have negligible permeability (Fung, 1993) and it can thus be assumed that  $J = 1$ . The Green (Green-Lagrange) strain,  $\mathbf{E}$ , is thus given by Belytschko *et al.*, (2000) as:

$$\mathbf{E} = \frac{1}{2}(\mathbf{F}^T \cdot \mathbf{F} - \mathbf{I}) \quad (21)$$

where  $\mathbf{I}$  is the identity tensor. The components of  $\mathbf{E}$  are computed more directly by:

$$\begin{aligned} E_{11} &= \frac{1}{2}(\lambda_1^2 + \kappa_2^2 - 1), & E_{12} &= \frac{1}{2}(\lambda_1\kappa_1 + \lambda_2\kappa_2), \\ E_{22} &= \frac{1}{2}(\lambda_2^2 + \kappa_1^2 - 1) \end{aligned} \quad (22)$$

### 3.5 Stress calculation

Biaxial testing of biological tissues is performed using thin specimens which in this case are thinner than 1 mm. It is assumed that only in-plane loads act in on the sample and thus creating a state of plane stress so that the components  $\sigma_{13}$ ,  $\sigma_{23}$ ,  $\sigma_{33}$  of the Cauchy stress tensor are zero.

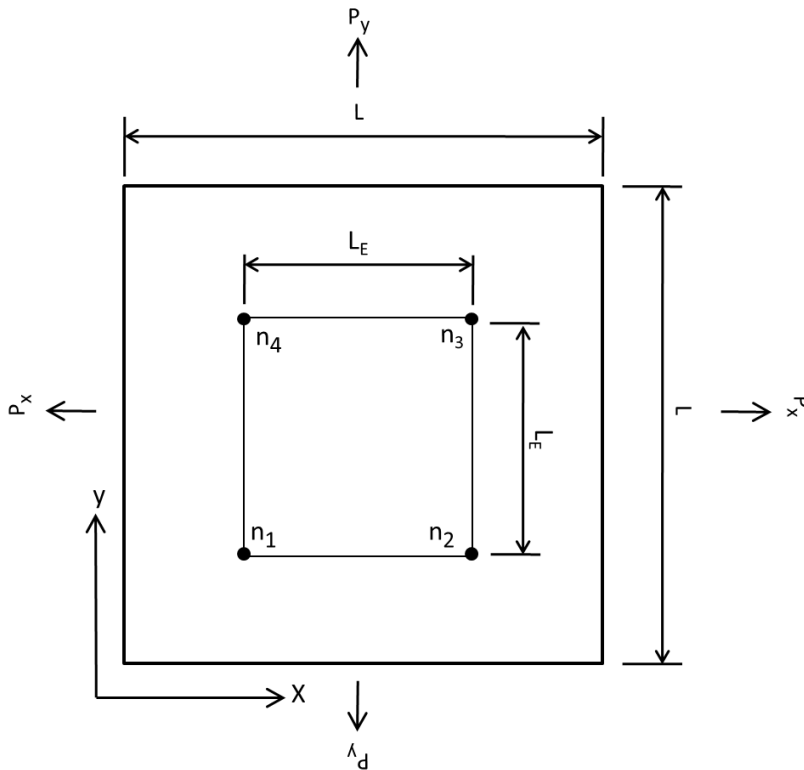


Figure 3-8: Stress calculation of test specimen

The change in thickness of the test specimen is negligible during loading and so is assumed to remain constant. The normal loads on the element are as follows:

$$P_{Ei} = \frac{PiL_E}{L}, \quad (i = X, Y) \quad (23)$$

where  $P_i$  is the normal distributed load applied over the length of the test sample,  $L$ , and  $L_E$  is the length of the element as can be seen in Figure 3-8.

In order to determine the Cauchy stress tensor the length ratios of the element were determined as follows:

$$LR_X = \frac{\left(\frac{n3_{Yi} + n4_{Yi}}{2} - \frac{n1_{Yi} + n2_{Yi}}{2}\right)}{\left(\frac{n3_{Yi} + n4_{Yi}}{2} - \frac{n1_{Yi} + n2_{Yi}}{2}\right)}, \quad (i = 1, 2, 3, \dots) \quad (24a)$$

$$LR_Y = \frac{\left(\frac{n2_{Xi} + n3_{Xi}}{2} - \frac{n1_{Xi} + n4_{Xi}}{2}\right)}{\left(\frac{n2_{Xi} + n3_{Xi}}{2} - \frac{n1_{Xi} + n4_{Xi}}{2}\right)}, \quad (i = 1, 2, 3, \dots) \quad (24b)$$

where  $n$  is an element node. The cross-sectional area of the element is thus:

$$A_i = tLR_iL_E, \quad (i = X, Y) \quad (25)$$

where  $t$  is the average thickness of the test sample. The Cauchy stress tensor for biaxial loading in the  $x$  and  $y$  directions follows as:

$$\boldsymbol{\sigma} = \begin{bmatrix} \frac{P_{EX}}{A_X} & 0 \\ 0 & \frac{P_{EY}}{A_Y} \end{bmatrix} \quad (26)$$

The symmetric second Piola-Kirchhoff stress tensor follows as (Belytschko *et al.*, 2000):

$$\boldsymbol{S} = J\boldsymbol{F}^{-1} \cdot \boldsymbol{\sigma} \cdot \boldsymbol{F}^{-1} \quad (27)$$

where  $J$  and  $\boldsymbol{F}$  are the Jacobian determinant and the deformation gradient, respectively, and are calculated as shown in the previous section. It should be noted that Sacks and Sun (2000) and (2003) calculated the Lagrangian stresses (force/unit original cross-sectional area) which does not always result in a symmetric second Piola-Kirchhoff stress tensor. In this study the Cauchy stress tensor was used in order to calculate a symmetric second Piola-Kirchhoff stress tensor.

### 3.6 Test protocol

A test protocol was developed in order to improve repeatability and accuracy. Techniques were developed to select, prepare and mount the test sample.

#### 3.6.1 Sample selection and preparation

The bovine pericardium provided for this study was supplied pre-cut into approximately 50 mm x 100 mm sections, whereas for the kangaroo pericardium, almost the whole heart sack was provided. Due to the large size of bovine heart sacks, the sections were relatively flat and easy to handle, but the kangaroo sections were bowl-shaped with a distinct ripple texture. The test samples had undergone no preconditioning.

To ensure that the test sample was correctly orientated for the tests, the fibre direction had to be determined as accurately as possible. It was found that the fibre orientation was highly irregular on each pre-cut section and generally not aligned in a single direction. Pictures were taken of the pre-cut tissues and the fibres were highlighted through digital alteration, by increasing the contrast of the pictures while decreasing the brightness. The colours were then inverted and the picture was converted to black and white. This alteration can be seen in Figure 3-9. Sections with more prominent fibre alignment were identified for cutting out the test samples. As can be seen in Figure 3-10, a Perspex stencil with holes was used along with a scalpel to cut the test sample out of the pre-cut tissue. The holes were used as a guide for making the optical and load attachment markers on the tissue with a ballpoint pen.

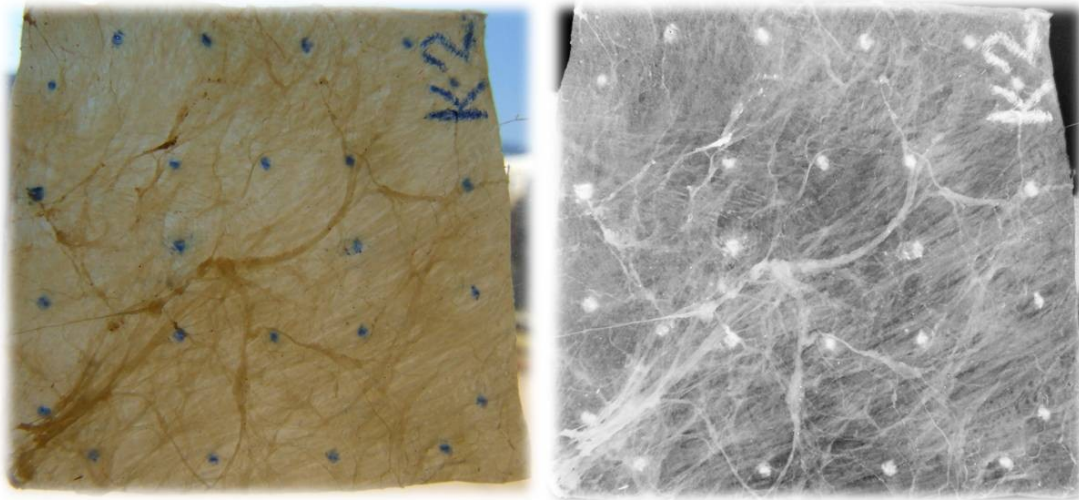


**Figure 3-9: Picture of test sample before (left) and after (right) digital alteration**



**Figure 3-10: Stencil for cutting out test samples**

### 3.6.2 Placement of sample in the testing device

A 32 mm x 32 mm sample was used in this study. Load attachment positions were marked on the outer perimeter of the test sample, 3 mm from the edges and 7.5 mm apart, as shown in Figure 3-11. A 12 mm x 12 mm square element, centred on the test sample, was marked at its nodes. The fibre direction of the test sample was chosen to lie at 45° to the coordinate system so as to induce a maximum shear state when applying normal loads. The loads were applied using # 16 size fishing hooks placed on the designated load markers to allow shearing of the sample. Styrofoam floats were placed over the hooks to eliminate the effect of gravity on the readings. Braided fishing line was used to transfer the loads from the pulley system to the test sample. The placement of the test sample in the testing device can be seen in Figure 3-12.

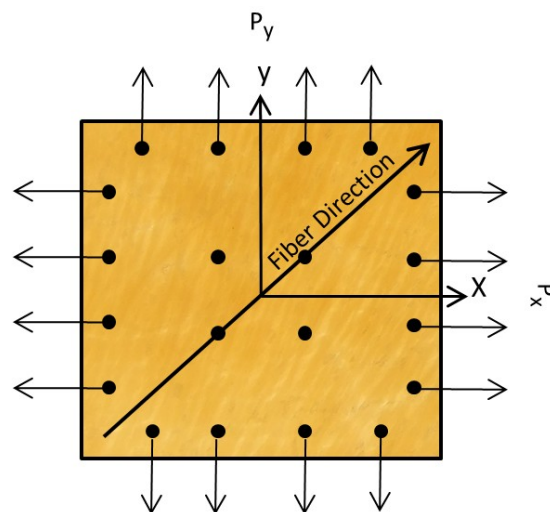


**Figure 3-11: Schematic of fibre orientation and load application**

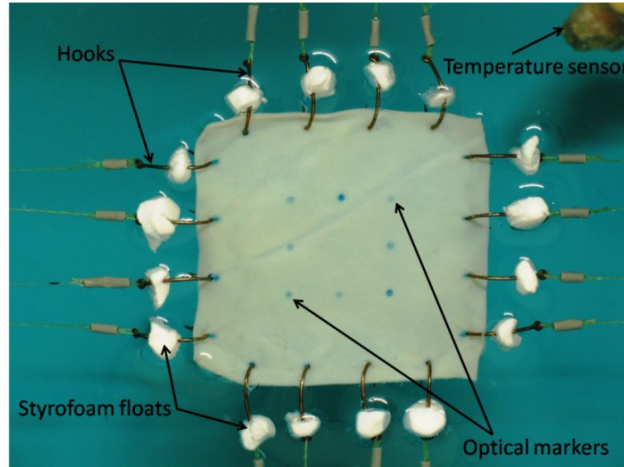


**Figure 3-12: Placement of test sample**

### 3.6.3 Human tissue test setup

Biaxial tests were also conducted on a fresh human valve as shown in Figure 3-13 in order to compare its material properties with that of the pericardium substitutes. The valve was harvested from a fresh male cadaver and provided by the pathology unit situated at Tygerberg Hospital after written consent was given by the relatives.

The valve leaflets were removed first after which 10 mm x 10 mm pieces were cut out with the circumferential direction of the leaflet located at a 45° angle relative to the x-axis of the testing device. Only two hooks were placed on each side of the test sample due to the space limitations. The optical markers in the centre were approximately 3 mm apart. The fresh tissue tests were conducted in a phosphate buffered saline solution. The average thickness of the leaflets was measured as 0.1 mm. Billiar and Sacks (2000) performed biaxial mechanical tests on natural and glutaraldehyde treated porcine valves. Their test specimen widths ranged from 10 mm to 16 mm. They also found a large disparity in the extensibilities between the circumferential and radial directions along with significant differences in the mean extensibility of fresh and treated valves.



**Figure 3-13: Human valve tissue procurement and testing**

### 3.6.4 Calibration

Before the test sample is placed in the testing device, a calibration picture is taken in order to compensate for camera distortion, as can be seen in Figure 3-14. The calibration object is a piece of paper with 16 markers printed on it. There is a 13 mm space between each marker and the next.

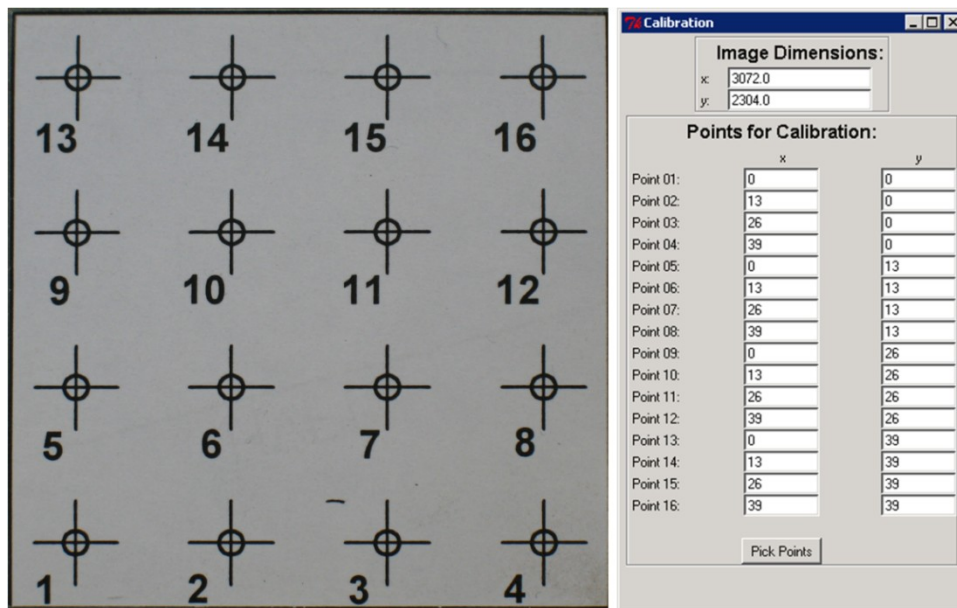


**Figure 3-14: Calibration object and window**

The corresponding world coordinates and image dimensions are inputs for the calibration window which calculates the optimized distortion coefficients and camera matrix according to the methods described in section 3.3.

### 3.6.5 Graphical user interface (GUI) and data processing

The scripting language used for the graphical user interface (GUI) and calculations was Python™. The image dimensions, sample thickness, test sample length and element length are fixed inputs for each sample test. Each image corresponding to a load increment is renamed so that the name contains the respective normal loads applied at that increment. The normal loads are thus automatically obtained for the calculations. The outputs of the GUI are the second Piola-Kirchoff stress tensor and the corresponding Green strain tensor. The GUI can be seen in Figure 3-15. The measurements were synchronized by taking a picture at the exact time the load measurement was taken. The camera activation and load recordings were controlled manually by using the computer.

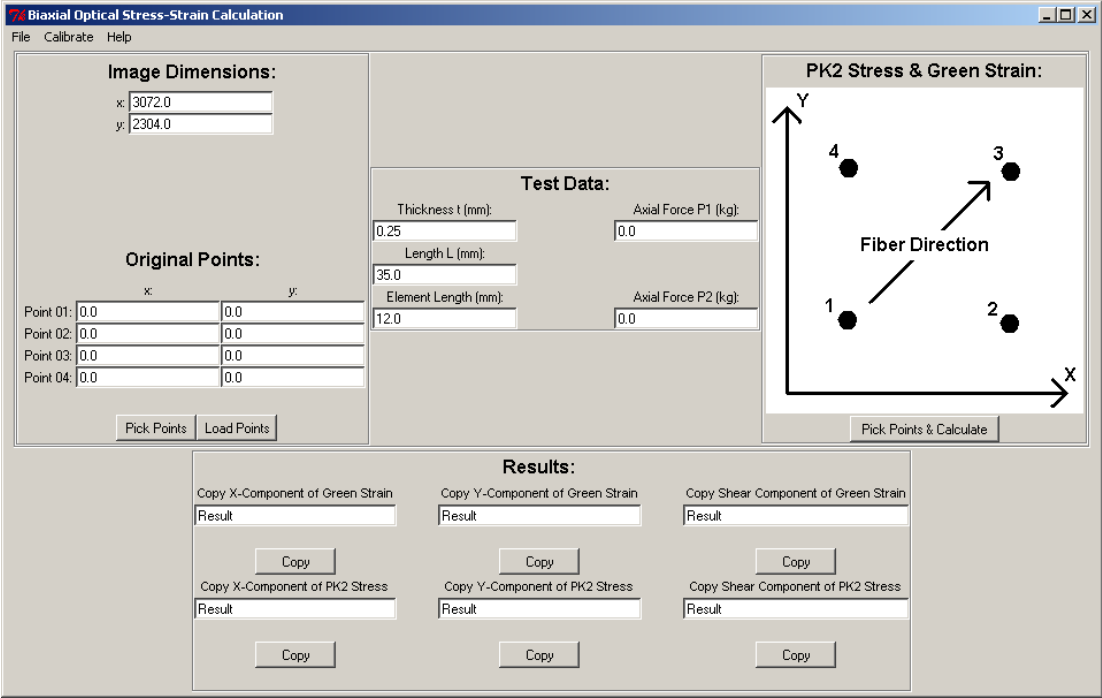


Figure 3-15: Graphical user interface (GUI) for stress-strain calculations

After calibration, the original points are manually picked from an image taken where no loads were applied and the test sample is thus assumed to be stress free. The nature of the tissue surface provided distinct locations on or near the markers to be recognized to be repeatedly picked during each load interval to increase the accuracy, as shown in Figure 3-16. Once the original points are picked, the images corresponding to the loads applied are processed and the corresponding stresses and strains are calculated according to the methods described in section 3.4 and 3.5.

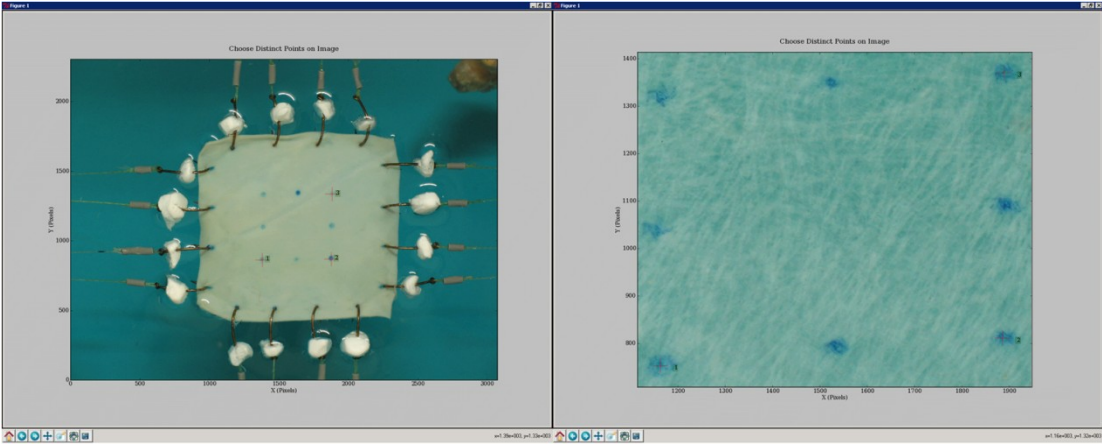


Figure 3-16: Picking of markers for node location

### 3.7 Material parameters

Three kangaroo and three bovine test samples with the most uniform fibre alignment were selected to determine the material properties of each tissue. Three load controlled biaxial test protocols were conducted on each test sample with axial load ratios of  $P_x:P_y = 1:1, 1:2$  and  $2:1$ . This, along with the fact that the axial loads were adjusted manually which caused small variations in the load ratios, produced a wide range of normal and shear stress combinations.

#### 3.7.1 Enforcement of convexity

The experimental data are related to the predicted stresses by the Fung constitutive model by using nonlinear regression techniques. However, due to the complexity of the constitutive model, the resulting model may be numerically unstable. This means that it will generally not lead to convergent solutions. The Newton-Raphson method is usually used in finite element software to evaluate the material stiffness matrix which is a function the fourth-order elasticity tensor,  $\mathbf{C}$ , and is obtained by:

$$\mathbf{C} = \frac{\partial \mathbf{S}}{\partial \mathbf{E}} \quad (28)$$

If  $\mathbf{C}$  is positive definite, full rank and well-conditioned, the numerical solution will be stable and accurate (Sun and Sacks, 2005). It can be shown that  $\mathbf{C}$  is the second partial derivative or Hessian of  $\mathbf{W}$ . If the Hessian of a function is positive definite, the function will be convex. Thus, if  $\mathbf{C}$  is positive definite, the convexity of the constitutive model is enforced. The elasticity tensor,  $\mathbf{C}$ , can be expressed in matrix form for the model used in this study as:

$$\mathbf{D} = \frac{c}{2} e^Q \begin{bmatrix} 2A_1 + \xi_1^2 & 2A_3 + \xi_1\xi_2 & 2A_5 + \xi_1\xi_3 \\ & 2A_2 + \xi_2^2 & 2A_6 + \xi_2\xi_3 \\ sym & & 2A_4 + \xi_3^2 \end{bmatrix} \quad (29)$$

where  $\xi_1 = 2A_1E_{11} + 2A_3E_{22} + 2A_5E_{12}$ ,  $\xi_2 = 2A_2E_{22} + 2A_3E_{11} + 2A_6E_{12}$  and

$$\xi_3 = 2A_4E_{12} + 2A_5E_{11} + 2A_6E_{22}.$$

Sun and Sacks (2005) imposed the convexity condition by examining  $\mathbf{D}$  in the reference configuration (where  $E_{11} = E_{22} = E_{12} = 0$ ):

$$\mathbf{D} = \frac{c}{2} \begin{bmatrix} 2A_1 & 2A_3 & 2A_5 \\ 2A_3 & 2A_2 & 2A_6 \\ 2A_5 & 2A_6 & 2A_4 \end{bmatrix} \quad (30)$$

The definition of positive definiteness requires that the determinants associated with all the upper-left submatrices are positive. The resulting parameter constraints that satisfy positive definiteness for  $\mathbf{D}$  are:

$$c > 0, A_1 > |A_3|, A_2 > |A_3| \text{ and} \tag{31}$$

$$A_1 A_2 A_4 + 2 A_3 A_6 A_5 - A_5^2 A_2 - A_6^2 A_1 - A_3^2 A_4 > 0$$

These constraints are not sufficient to guarantee positive definiteness over the entire strain range, but are used as a preliminary test for convexity violation. It is still necessary to evaluate the convexity over the entire measured strain range to ensure that positive definiteness is always satisfied. For planar biaxial loading of biomembranes, convexity implies that the projections of the contours of the strain energy,  $\mathbf{W}$ , on the  $E_{11} - E_{22}$ ,  $E_{11} - E_{12}$  and  $E_{22} - E_{12}$  planes form convex surfaces (Holzapfel, 2000). Sun and Sacks stated that it is sufficient to examine the convexity of  $\mathbf{D}$  along projections of  $\mathbf{W}$  against two strain components with the other component set to zero.

### 3.7.2 Condition number

Sun and Sacks also examined the condition number,  $R$ , of  $\mathbf{D}$  which is defined as:

$$R = \|\mathbf{D}\| \cdot \|\mathbf{D}^{-1}\| \tag{32}$$

where  $\|\mathbf{D}\| = \max \sum_{i=1}^n |D_{ij}|, 1 \leq j \leq n$

The lower the value of  $R$ , the better the numerical stability of the constitutive law is. Sun and Sacks found that  $R \leq 200$  was acceptable for numerical convergence.

### 3.7.3 Nonlinear regression

The *fminsearch* function from Matlab was used to fit the experimental data to the Fung model. This function, which implements the Nelder-Mead simplex method, finds the minimum of a scalar function of several variables, starting at an initial estimate. This is generally referred to as unconstrained nonlinear optimization. It uses a function handle of which the output is minimized.

The output to be minimized is the sum of the absolute differences between the experimental and the predicted stresses by the Fung model for the current estimated constants. It can be noted that due to the fact that the normal stresses were approximately ten times larger in magnitude than the shear stresses, the shear stress error was multiplied by ten. This resulted in a more accurate data fit. The constraints in *equation 31* were implemented as penalties in the function handle.

After the regression has converged, the convexity of  $\mathbf{D}$  was checked by projecting  $\mathbf{W}$  against two strain components with the other component set to zero. These projections are shown in Figure 3-17 with (d, e, f) and without (a, b, c) the convexity condition imposed. Note the presence of a hyperbolic or saddle shaped strain energy function when the convexity condition is not imposed.

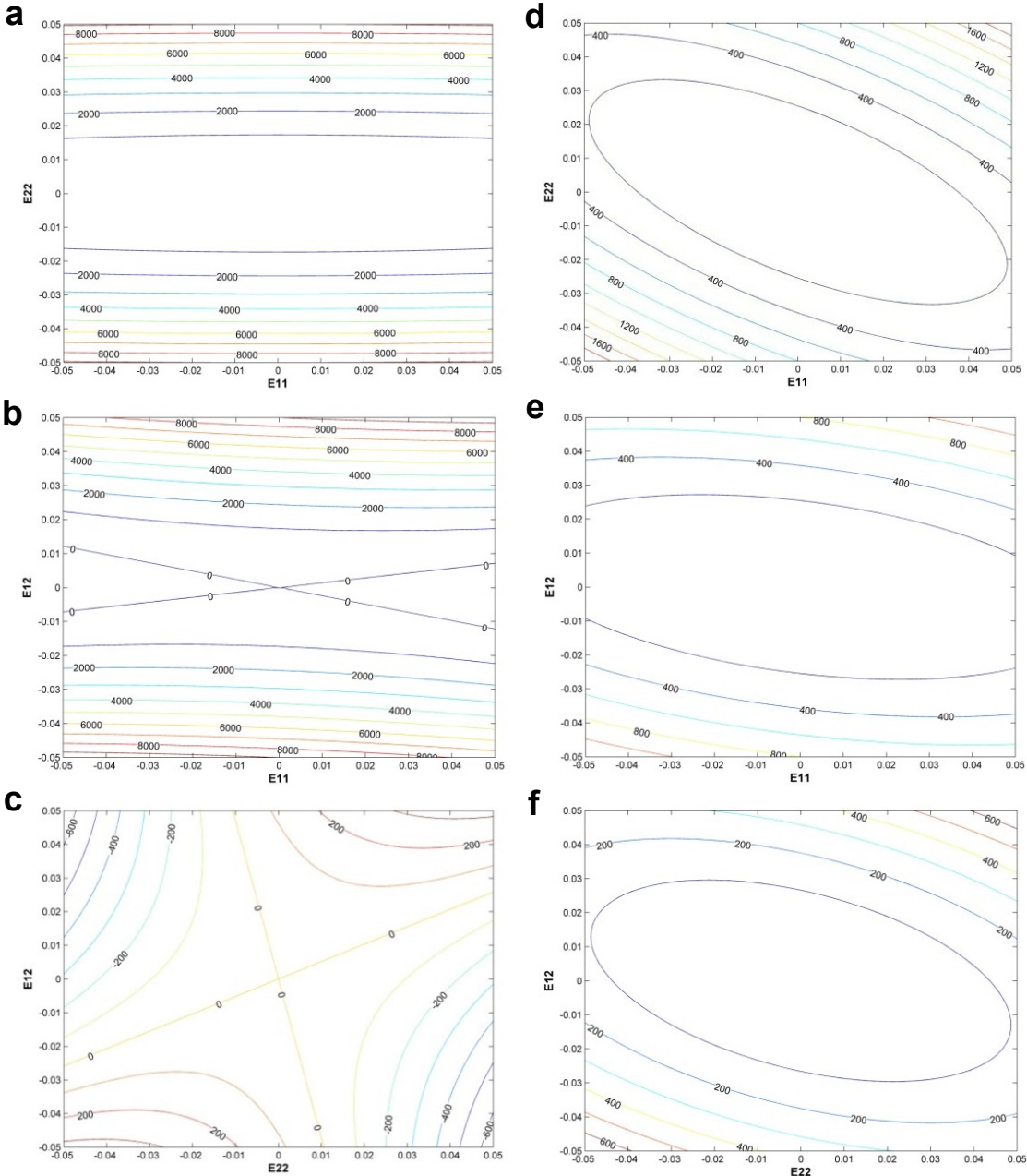


**Figure 3-17: Contour plots representing the projections of  $W$  against two strain components with the other component set to zero with (d, e, f) and without (a, b, c) the convexity condition imposed.**

The material parameters found are given in the next chapter. The parameters are also implemented in FEM and used to evaluate the different tissues that were tested.

## CHAPTER 4

### 4. MATERIAL EVALUATION

Both kangaroo and bovine pericardium were considered for the manufacturing of the PAVR. The higher resistance to calcification and the fact that kangaroo pericardium is thinner than bovine pericardium, makes it more attractive for this application. As previously mentioned, conventional bioprosthetic valves are usually made from bovine pericardium. This emphasizes the need to compare the kangaroo pericardium, of which the thicknesses ranges from 0.13 mm to 0.22 mm, with the bovine pericardium of which the thicknesses ranges from 0.25 mm to 0.5 mm. The data from the human tests was also compared with the pericardial tissues.

#### 4.1 Material constants

The experimental data of all the tests for each pericardium tissue were simultaneously fitted to the Fung constitutive model. Three pieces of tissue per pericardium type were tested with the load ratios described in section 3.7. It was only possible to conduct one test on human valve tissue with the load ratios described in section 3.7. The average material constants for the bovine, kangaroo and human tissue are shown in Table 4-1. The material constants for each piece of tissue are given in Appendix A.

**Table 4-1: Parameters for the Fung-type elastic constitutive model**

	<b>C(kPa)</b>	<b>A1</b>	<b>A2</b>	<b>A3</b>	<b>A4</b>	<b>A5</b>	<b>A6</b>
<b>Bovine</b>	5.7	52.1	25.8	24.8	14.4	7.25	13.4
<b>Kang</b>	4.41	9.42	29.3	7.49	1.24	0.24	0.03
<b>Human</b>	1.91	6.04	58.25	6.03	9.95	0.19	3.7

It was found that when the material constants were determined for a single sample, the Fung model predicted the experimental data more accurately than using all the test samples. This was an indication of the variations and non-uniform fibre directions between the tissue samples. The data fitting for the normal and shear stresses for a bovine tissue sample are shown in Figure 4-1 and Figure 4-2, respectively, as an example.

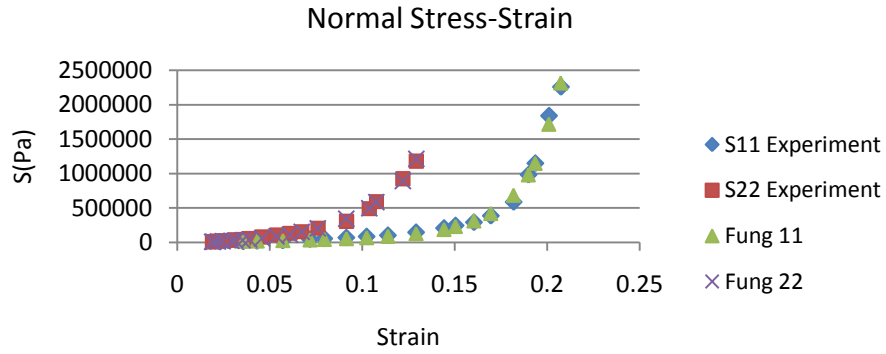


**Figure 4-1: Nonlinear regression fitting results for the normal stresses**

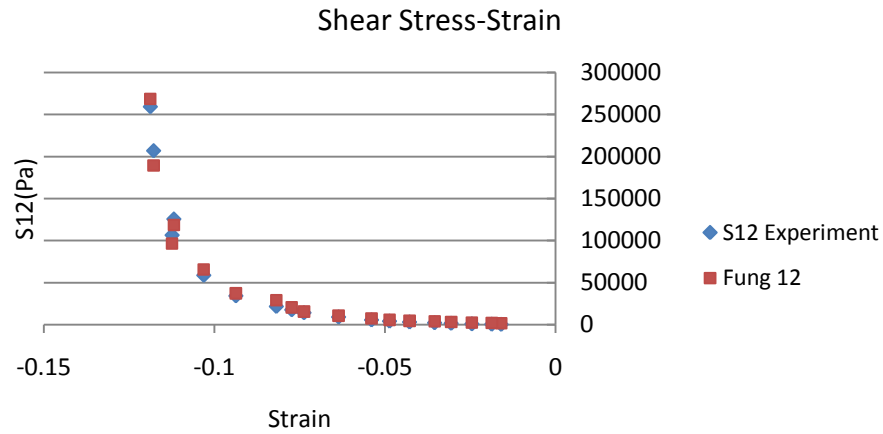


**Figure 4-2: Nonlinear regression fitting results for the shear stresses**

## 4.2 Finite element analysis (FEA) implementation

In order to evaluate the different materials and valve designs, finite element analysis was used with the Fung constitutive model implemented. MSC.Patran was used as the pre-processor and MSC.Marc as the nonlinear post-processor (MSC.Marc, 2007).

The Hypela2 Fortran user subroutine from Marc was used to implement the Fung constitutive model. This subroutine gives the user the ability to implement arbitrary material models. Marc supplies the user with, among others, the total strain and increment of strain. The user is expected to calculate the stresses, tangent stiffness and the state variables (if present) that correspond to the strain at the end of the increment ( $t = n + 1$ ). When the LARGE STRAIN parameter in Marc is used, the logarithmic strains and Cauchy stresses are passed and when the LARGE DISP parameter is used, the Green-Lagrange strains and second Piola-Kirchoff stresses are

passed. The LARGE DISP parameter was used due to the fact that the Fung constitutive model is defined in terms of Green-Lagrange strains and second Piola-Kirchoff stresses. The tangent stiffness,  $\mathbf{D}$ , is defined by Marc as:

$$D_{ij} = \frac{\partial(\Delta\sigma_i)}{\partial(\Delta\varepsilon_j)} \quad (33)$$

where  $\sigma_i$  is a stress and  $\varepsilon_j$  a strain element of the stress and strain tensors, respectively. The rate of convergence depends critically on the user supplied tangent stiffness. A fully consistent exact tangent stiffness provides quadratic convergence of the displacement. The code for the user subroutine is shown in Appendix B.

The bilinear thin-shell element (element 139) which is a four-node, thin-shell element with global displacements and rotations as degrees of freedom was used for the simulations. The element can be used in curved shell analysis. The element is not very sensitive to distortion and it can be used with all constitutive relations.

### 4.3 Finite element analysis (FEA) validation

The FEA implementation of the Fung model had to be validated. The FEA implementation was validated by comparing simulations of the biaxial tests with the actual experimental test data as is shown in Figure 4-3. The test sample was simulated using 19600 shell elements. This allowed the position of the hooks which transmits the loads to be placed accurately. The 35 mm x 35 mm element in the centre was represented by 2304 shell elements of which the average stresses and strains over all 2304 shell elements were used for the validation.

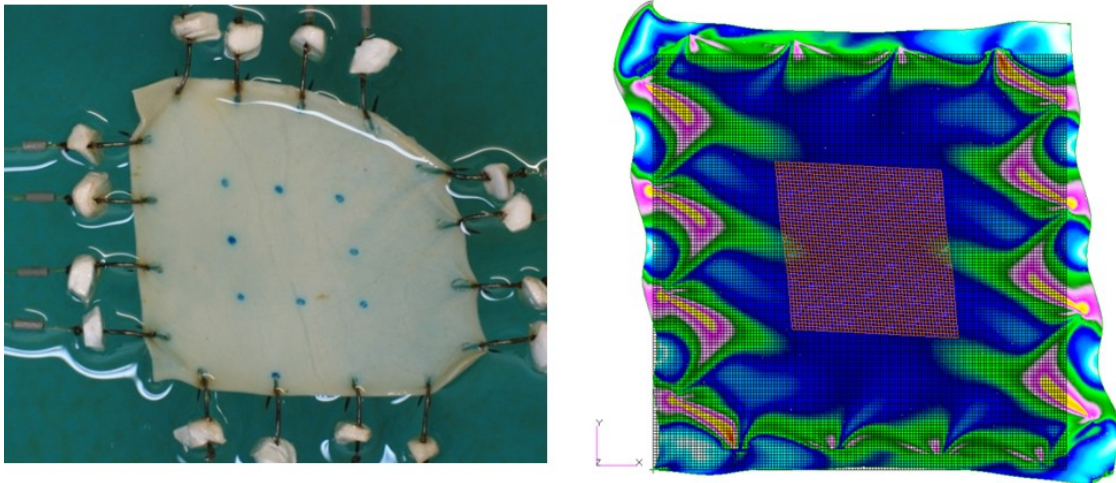


**Figure 4-3: Validation of FEA using a load ratio of 2:1 on Bovine sample # 2**

The stress-strain curves from the FEA simulations were compared with the actual experimental data as are shown in Figure 4-4 and Figure 4-5 respectively. The difference in especially the shear strain plots are mainly due to the fact that the load steps used in the experiment were not always exactly in ratios of  $P_x:P_y = 1:1, 1:2$  and  $2:1$ .

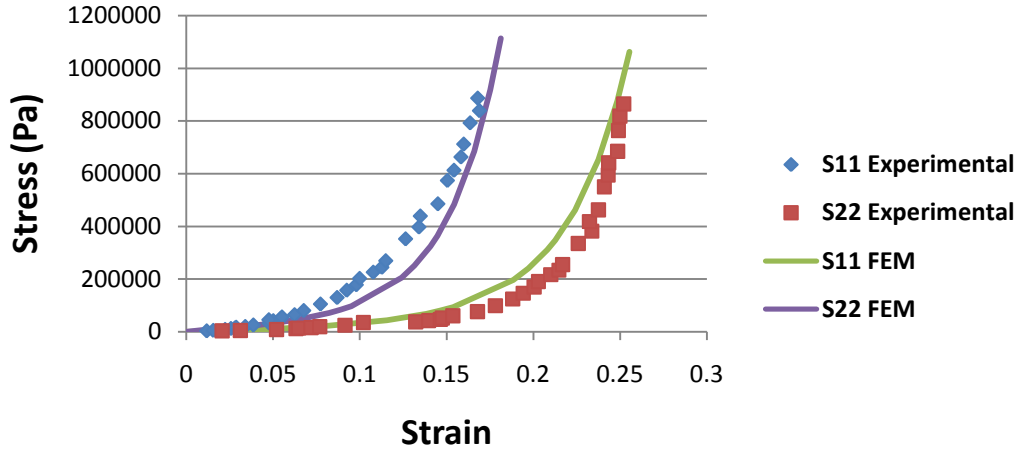


Figure 4-4: Normal stress FEA and experimental comparison

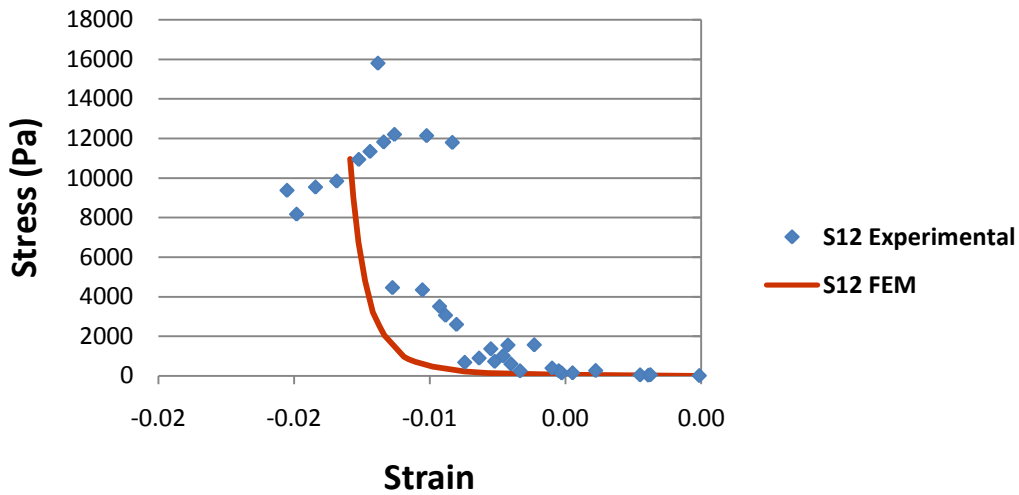


Figure 4-5: Shear stress FEA and experimental comparison

### 4.4 Material comparison

The bovine, kangaroo and human tissue were compared by evaluating the stress-strain curves as well as strain energy properties.

#### 4.4.1 Stress-strain curve comparison

The normal and shear stress-strain relationships for the human, bovine and kangaroo tests are shown in Figure 4-6 and Figure 4-7 respectively for a load ratio of 1:1. It can be seen that the kangaroo tissue possesses on average the highest extensibility followed by the bovine tissue. The difference in the 11 and 22 directions again emphasizes the fact that the fibre orientation is not uniform. The stress-strain relationships for all the experimental tests are shown in Appendix A.

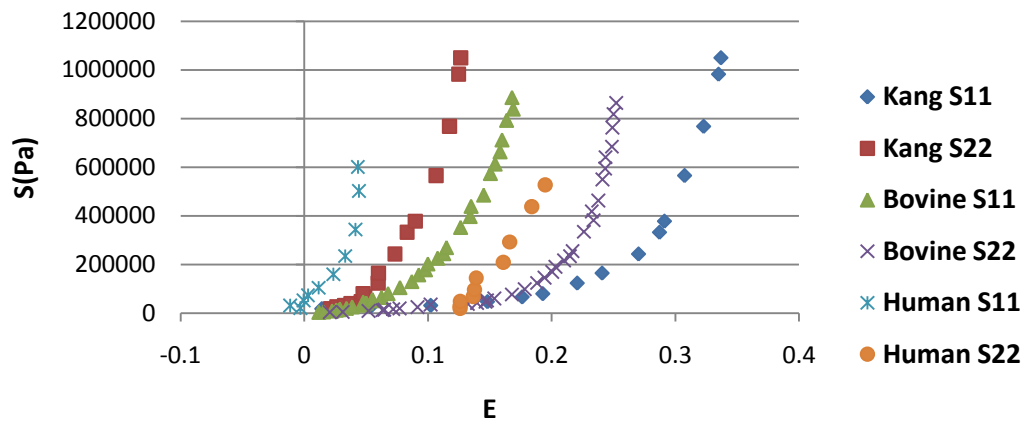


Figure 4-6: Normal stress-strain plots of kangaroo, bovine and human for a load ratio of 1:1

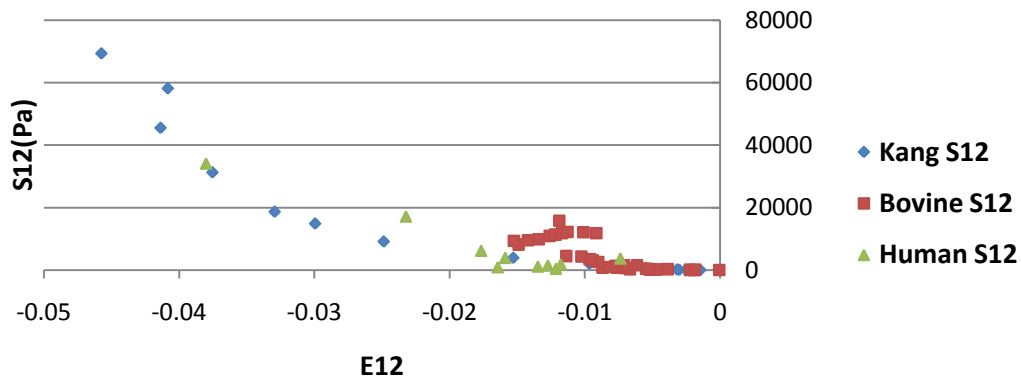


Figure 4-7: Shear stress-strain plots of kangaroo, bovine and human for a load ratio of 1:1

#### 4.4.2 Strain energy comparison

Due to the complexity and nonlinearity of the constitutive model, it is difficult to compare materials as there is no distinct modulus of elasticity or shear modulus for the material. The strain energy represents the total work done against internal forces during loading (Timoshenko and Goodier, 1970). The same model used for the FEA validation was used to compare the bovine and kangaroo material tissue properties as well as an isotropic material with a modulus of elasticity of 5 MPa (Arcidiacono *et al.*, 2005) and a Poisson ratio of 0.3 (Kim *et al.*, 2006). The average strain energy of the 2304 finite elements in the centre of the model was compared. Axial load ratios of  $P_x:P_y = 10:10$ ,  $5:10$  and  $10:5$  N respectively, were placed on the models. All the models had a thickness of 0.25 mm to ensure accurate material comparison. The isotropic model was used as a comparison. The results are shown in Table 4-2.

**Table 4-2: Strain energy of kangaroo, bovine and human pericardium using the Fung model as well as an isotropic model for comparison**

Loads X:Y (N)	Bovine (kJ)	Kang (kJ)	Human (kJ)	5 MPa Isotropic (kJ)
5:10	103	129	50	112
10:5	68	136	76	112
10:10	104	165	77	161

It can be noted that the higher the strain energy, the more work needs to be done against the internal forces and thus indicates a less stiff material. To compare the tissue more accurately, the same tests were done by giving each material its own average thickness in the simulation. The average thicknesses were 0.35 mm for bovine, 0.16 mm for kangaroo and 0.1 mm for the human tissue. A load ratio of 1:1 N was applied during the simulation and the average strain energy and von Mises stresses for the centres of the models are shown in Table 4-3.

**Table 4-3: Strain energy and von Mises stresses of kangaroo, bovine and human pericardium with their respective thicknesses, using the Fung model and subjected to a load ratio of 1:1 N**

	Bovine	Kang	Human
Strain energy (kJ)	34.17	37.48	75.98
von Mises stress (MPa)	0.855	0.773	2.82

It can be seen from Table 4-3 that the thicker bovine and kangaroo pericardium possesses lower von Mises stresses and less work needs to be done against the internal forces than the native human valve tissue. This indicates that the bovine and kangaroo tissues would be mechanically fit for the manufacturing of valve prostheses.

## CHAPTER 5

### 5. VALVE DESIGN

Although the ideal valve design would be one that exactly resembles the native aortic valve, the presence of a balloon expandable stent, which poses its own geometry restrictions, limits the use of these ideal dimensions. The challenge is thus to achieve near ideal valve dimensions which are still compatible with the stent geometry.

#### 5.1 Native aortic valve dimensions

When the aortic valve is open, the circumference is  $2\pi R$  or approximately six times the radius,  $R$ . The total length of the free edges of the three leaflets is also approximately six times the radius when the valve is closed. This means that the three-leaflet valve can produce a circular opening without going through a large change in leaflet length. Two or four-leaflet valves will not produce a circular opening without undergoing large changes in leaflet length and producing folds in the leaflets (Thubrikar, 1990).

Figure 5-1 shows various dimensions that are used to describe the geometry of the aortic valve. Thubrikar (1990) reports that the average dimensions of the adult human aortic valve are  $R_b = 11.3$  to  $14$  mm,  $H = 15.7$  to  $19.8$  mm,  $\phi = 25$  to  $37^\circ$  and  $\alpha = 15$  to  $27^\circ$ . Thubrikar also found that the normalized dimensions of the aortic valve were fairly similar in various mammalian species which suggest that there is an underlying universal principle that governs the design of the aortic valve.

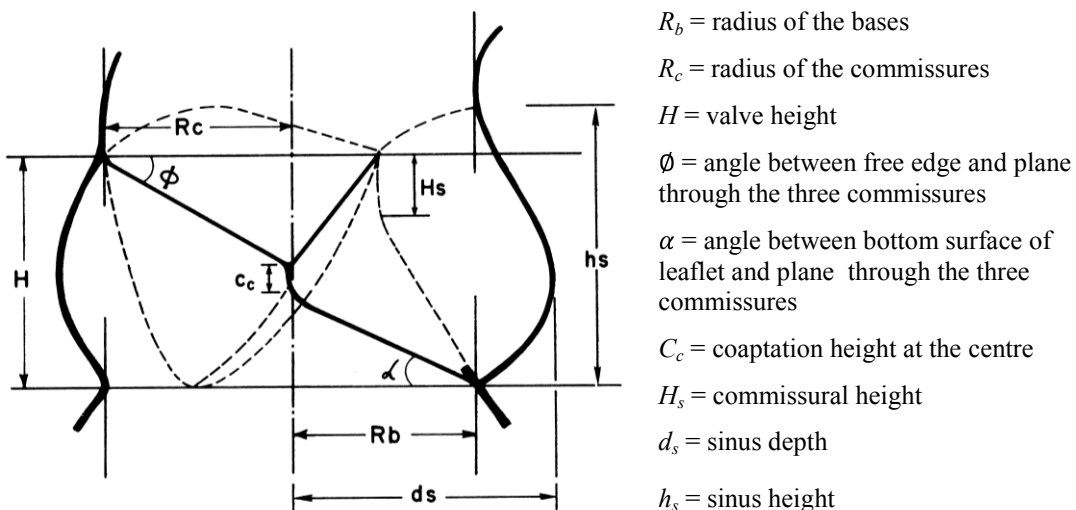
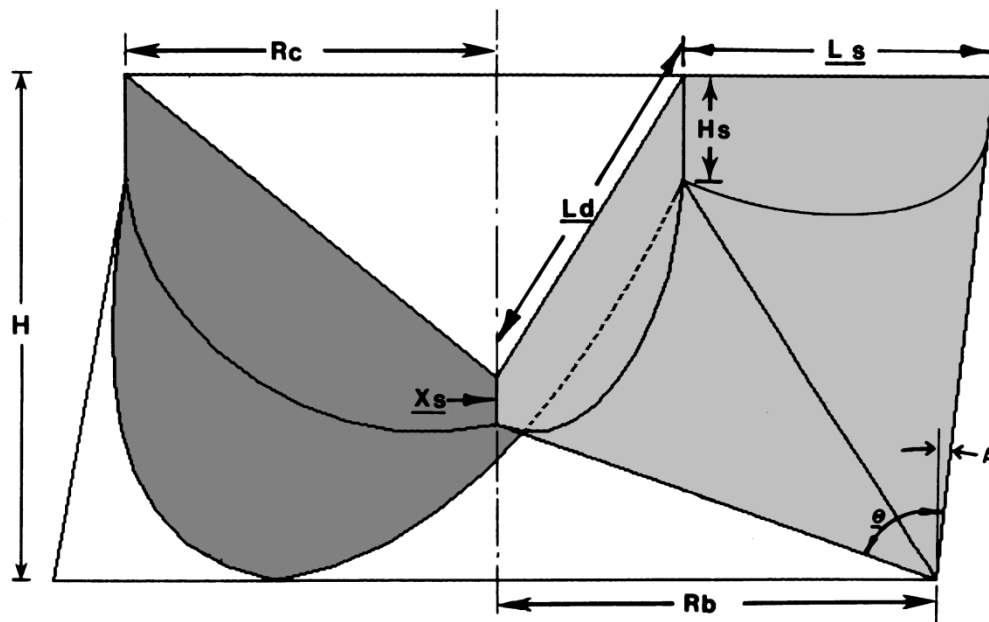


Figure 5-1: Aortic valve showing a side view of one leaflet (Thubrikar, 1990)

## 5.2 Native aortic valve design- and performance parameters

Thubrikar described the design of the aortic valve in terms of five design and four performance parameters as shown in Figure 5-2. A valve described using the design parameters has the following features (Thubrikar, 1990):

- The leaflets are cylindrical
- The free edge of the open leaflet lies in a plane passing through the three commissures
- Part of the line of leaflet attachment is vertical
- The remaining line of the leaflet attachment lies in a plane across which the leaflet can reflect to produce a closed valve.



### Design parameters:

$R_b$  = radius of the bases

$R_c$  = radius of the commissures

$H$  = valve height

$H_s$  = commissural height

$\beta$  = angle between open leaflet and vertical

### Performance parameters:

$\theta$  = angle of leaflet flexion

$X_s$  = minimum coaptation height

$L_d$  = leaflet length in diastole

$L_s$  = leaflet length in systole

**Figure 5-2: The design and performance parameters of the native aortic valve showing a side view (right) of one leaflet (Thubrikar, 1990)**

For the valve to have optimum performance, the following criteria were specified by Thubrikar:

- A certain minimum coaptation height ( $X_s = 0.1R_b$ ) to ensure valve closure
- No folds in the leaflet ( $L_s = L_d$ ) to eliminate folding stresses
- Minimum valve height,  $H$ , (low profile) to reduce dead space
- Minimum leaflet flexion to reduce flexion stresses and conserved energy

Thubrikar developed the following geometric relationships to determine the design parameters for an optimal valve:

$$\theta^\circ = 180^\circ + 2\beta - 2\tan^{-1}\left(\frac{H - H_s}{R_b - \frac{R_c}{2}}\right) \quad (34a)$$

$$X_s = \frac{H}{\cos\beta} + \frac{R_b}{\sin\left[\beta - 2\tan^{-1}\left(\frac{H - H_s}{R_b - \frac{R_c}{2}}\right)\right]} \quad (34b)$$

$$L_D = 2 \cdot \sqrt{R_c^2 + \left\{H - X_s - R_b \cdot \tan\left[2\tan^{-1}\left(\frac{H - H_s}{R_b - \frac{R_c}{2}}\right) - \beta - 90^\circ\right]\right\}^2} \quad (34c)$$

$$L_s = \frac{\sqrt{3} \cdot R_c \left[ \pi - \left(\frac{\pi}{180^\circ}\right) \cdot 2 \cdot \tan^{-1}\left(\frac{\sqrt{3} \cdot R_c}{2R_b + 2H\tan\beta - R_c}\right) \right]}{\sin\left[2\tan^{-1}\left(\frac{\sqrt{3} \cdot R_c}{2R_b + 2H\tan\beta - R_c}\right)\right]} \quad (34d)$$

Thubrikar found that the two performance criteria, minimum height and minimum flexion, opposed each other. The valve height was found to be the maximum when  $R_c = R_b$ , but as  $R_c$  decreases the valve height decreases. It should be stated that too much reduction produces an obstructive valve. It was also found that a positive  $\beta$  lowered the valve height. The commissural height,  $H_s$ , also contributed to a reduction in the valve height.



$$L_e = H - \sqrt{\left(\frac{L_d}{2}\right)^2 - R_c^2} \quad (35a)$$

$$X_s = \frac{H^2 - L_e^2 - R_b^2}{2H - 2L_e} \quad (35b)$$

$$R_{AC} = \sqrt{(L_e - X_s)^2 + R_b^2} \quad (35c)$$

$$\theta^\circ = 90^\circ + \beta - \cos^{-1}\left(\frac{R_b}{R_{AC}}\right) \quad (35d)$$

#### 5.4 Implementation of valve design parameters

In order to achieve an optimal valve design, the valve design and performance parameters were used to aid in the valve geometry design.

The design parameters are used as the input for the optimal calculations whereby the performance parameters are calculated and evaluated. In the calculations for the straight valve, the leaflet length in systole can be given or calculated using *equation 34d*. The performance parameters are calculated as an output for those specific design parameters, given in *equations 35a - d*.

The optimal performance properties ( $X_s = 0.1R_b$ ,  $L_s = L_d$ ,  $\theta = \min$ ) were also used to find the optimal valve geometry for given design parameters. This was done by weighting each performance property and by giving some or all of the design parameters allowable ranges. The GUI implementations of these parameters for the native and straight valve are shown in Figure 5-4 and Figure 5-5, respectively. The GUI for the straight valve has a warning window that appears when the valve will not close properly, which informs the user to increase the height, leaflet length or strain. Optional strain may be added in the calculations to incorporate the actual extension of the leaflet height and length.

Labrosse *et al.*, (2006) found that to conservatively avoid leaflet prolapse under systolic pressure, angle  $\alpha$  of the closed leaflet to the basal plane should be greater than  $13^\circ$ , while the leaflet length,  $L_d$ , should be less than twice the leaflet height.

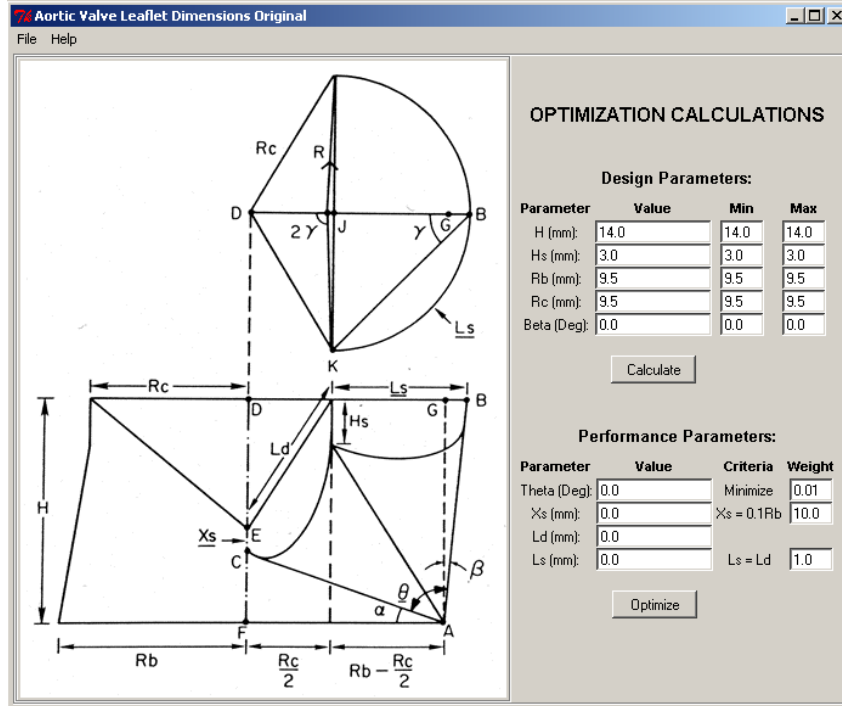


Figure 5-4: GUI for designing and evaluating a native aortic valve

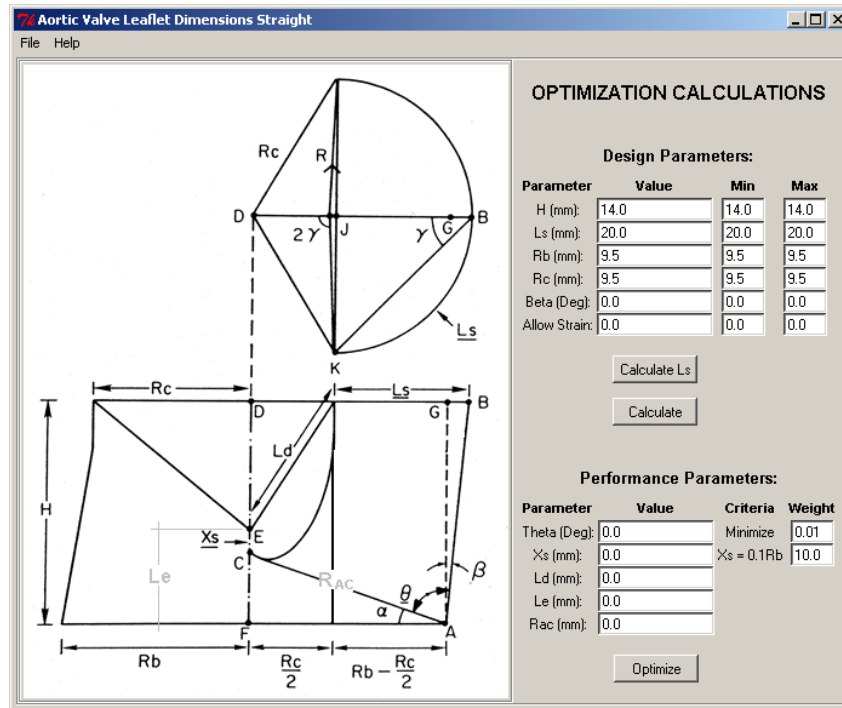


Figure 5-5: GUI for designing and evaluating a straight aortic valve

## 5.5 Valve geometry design

The valve and stent geometry designs are highly dependent on each other which meant that both had to be altered from a possible ideal geometry to complement each other in order to provide an optimal valve. The stent design and analysis was conducted by Esterhuyse, (2008).

Four stent concepts were considered for valve manufacturing, shown in Figure 5-6. Concept A consists out of a diamond-shaped mesh whereas the other concepts have a “zigzag” mesh with vertical support bars. Concepts B and C have three vertical holed bars to provide vertical attachment for the valve. The vertical bars of concept B are extended to allow for a sealing section for the straight valve at the bottom. Due to the lower height of concepts A, C and D, an additional sealing method is needed to avoid paravalvular regurgitation. One of the main criteria to evaluate the stents was the ability of the stent to support the tissue valve attachment regions, and its contribution to high stress concentrations and excessive leaflet folding. The stents were designed for in vivo trials in sheep, with an outer diameter of 20 mm and a wall thickness of 0.5 mm.

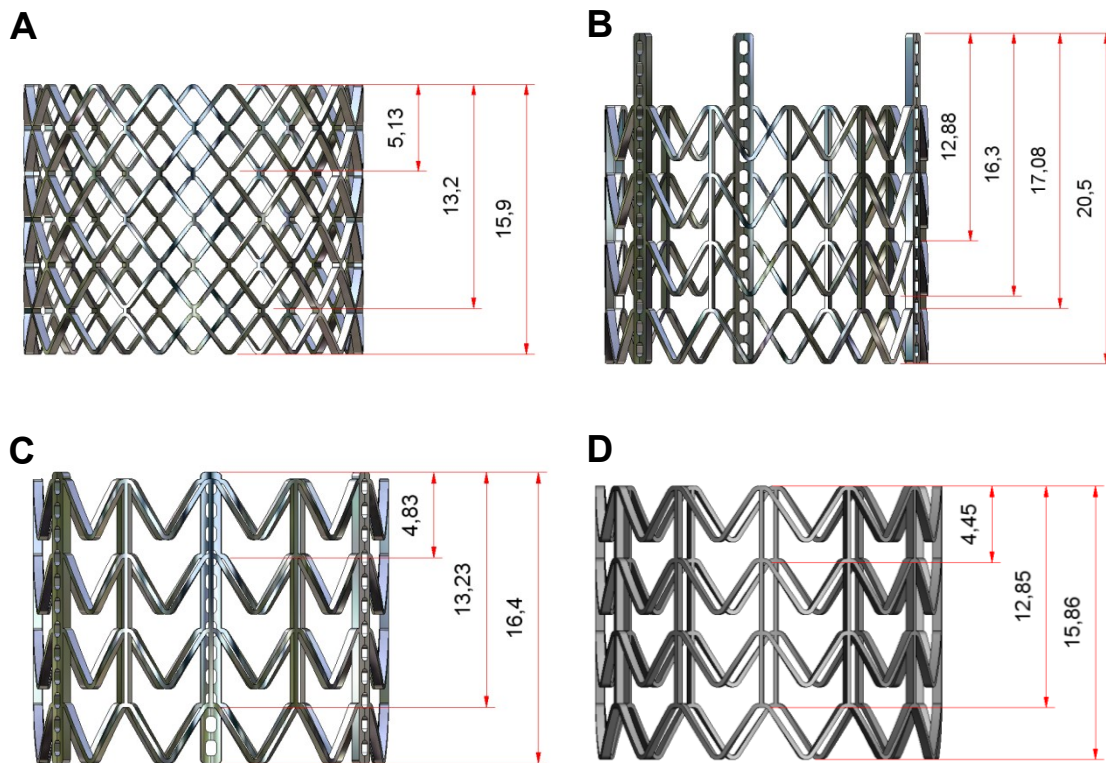
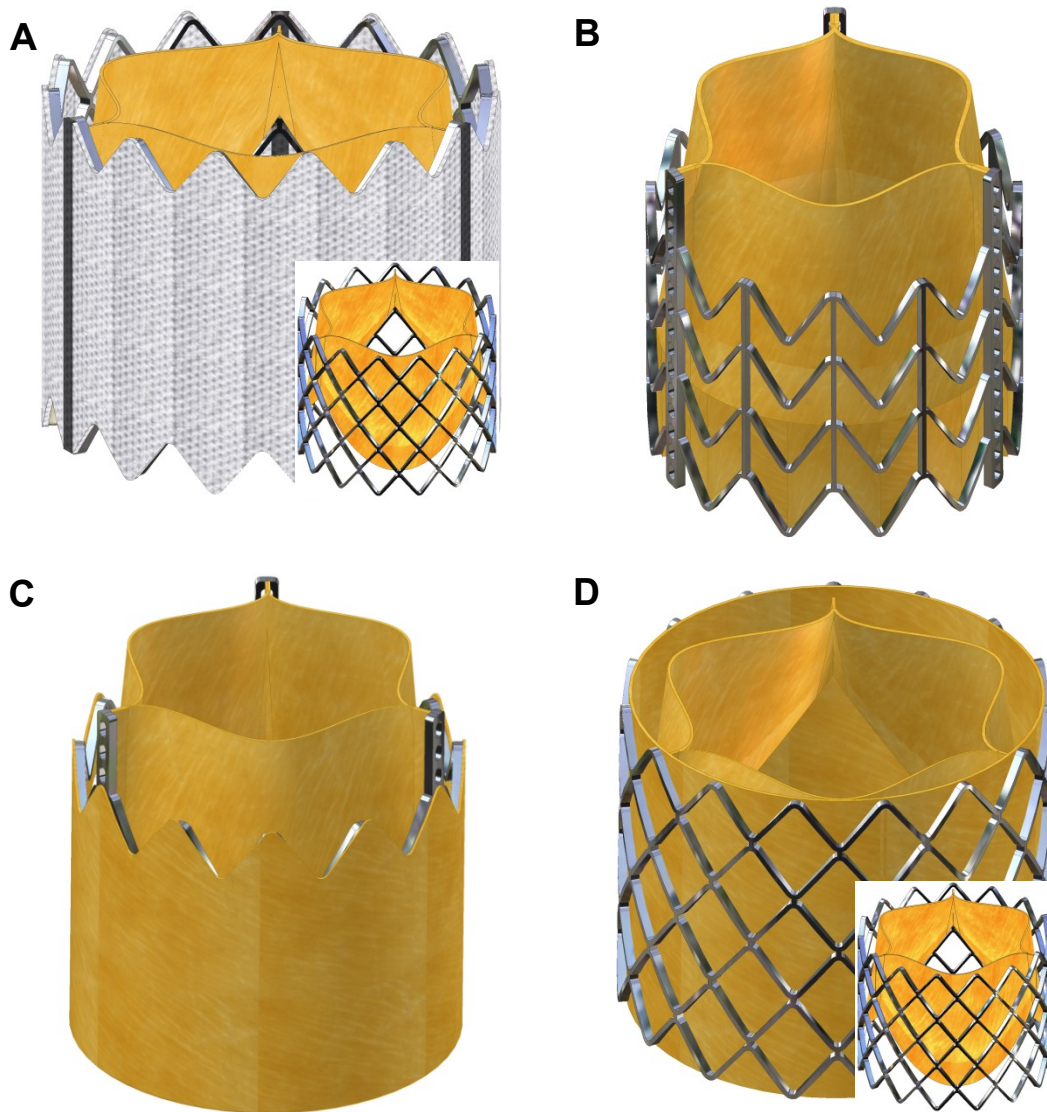


Figure 5-6: The four different stent designs with measurements

Four different valve design concepts were developed which can be divided in two main categories, namely, curved or native shaped, and straight leaflets. In Figure 5-7 it can be seen that concepts A and D have native shaped leaflets with the distinct parabolic shape at the base. These concepts also possess additional sealing components which may be situated on the inside or outside of the stent for which both synthetic material and tissue were considered. Concepts B and C have straight leaflets which in the case of concept B uses the lower leaflet section for sealing. Each leaflet of concept C is folded back over the outside of the stent to provide sealing.



**Figure 5-7: The four different valve designs**

Concepts A and B were chosen for refinement due to the fact that they are easier to manufacture and have the potential for smaller crimping diameters. The lines of attachment used for the native and straight leaflet shapes are shown in Figure 5-8. The diamond meshed stent provides a near hyperbolic or native attachment line for the leaflet while the “zigzag” meshed stent catered for the straight leaflet and a section for sealing at the bottom.

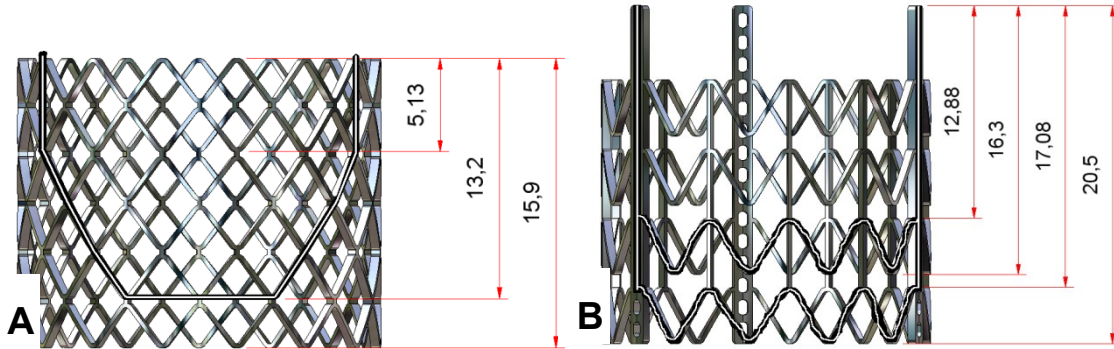


**Figure 5-8: Lines of attachment for concepts A and B**

The attachment dimensions derived from the attachment lines in Figure 5-8 were used as inputs for the evaluation calculations from which the performance parameters were calculated, as shown in Table 5-1. The most appropriate design and performance parameters for each concept were derived and used as geometry inputs in the valve assembly. The parameters in Table 5-1 are for a 20 mm outer diameter stent which was designed for trials in sheep.

**Table 5-1: The design and performance parameters for concepts A and B**

Design Parameters			Performance Parameters		
Parameter	Concept A	Concept B	Parameter	Concept A	Concept B
H (mm)	13.2	12.88	$\theta$ °	60.96	55.81
$H_s$ (mm)	5.13	N/A	$X_s$ (mm)	2.33	1.4
$L_s$ (mm)	N/A	21.5	$L_d$ (mm)	22.05	21.5
$R_b$ (mm)	9.5	9.5	$L_s$ (mm)	19.89	21.5
$R_c$ (mm)	9.5	9.5	$L_e$ (mm)	N/A	7.85
$\beta$ °	0	0	$R_{AC}$ (mm)	N/A	11.48
Strain	0	0			

## CHAPTER 6

### 6. VALVE MANUFACTURING

Due to the novelty of PAVR technology, there are basically no manufacturing guidelines and techniques available to aid in the design process. Currently there are only ISO standards for conventional heart valve prostheses (International Organization for Standardization , 2005). The techniques and procedures used in this study are detailed here.

#### 6.1 Attachment material considerations

The valve attachment material is essential in the manufacturing process as it provides the link between the tissue valve and the metal stent. It is essential that the material should be biocompatible and durable. Another requirement for the PAV is to aid in the low profile of the prosthesis, especially when crimped. The material is also subjected to displacements and tension during the crimping procedure.

Surgical sutures are commonly used in conventional valve prostheses. There are two main categories of sutures: monofilament vs. braided and permanent vs. absorbable. Absorbable sutures are not considered as these prostheses are designed to be permanent. Some monofilament sutures are commonly manufactured from nylon and are usually stiff and retain their packaged shape. Braided sutures are commonly manufactured from silk or cotton in a braided construction and are more soft and supple.

The suture range used in this study was from Gore-Tex<sup>®</sup>. These sutures are unique, microporous, non-absorbable monofilaments made of expanded polytetrafluoroethylene (ePTFE). Although these are monofilament sutures, they are also soft and supple, like braided sutures. In vivo tests have revealed that Gore-Tex sutures caused minimal capsule formation and limited inflammatory response which is generally greater with multifilament or braided sutures (GORE-TEX, 2008). These sutures have been specifically designed for cardiovascular surgery and are swaged to needles that closely approximate the diameter of the thread which enables the suture to fill the needle hole and reduce leakage. PTFE is one of the most inert materials known and clinical trials have shown that it elicits minimal tissue reaction and is also not weakened by the action of tissue enzymes or infection (GORE-TEX, 2008). The internodal spaces permit infiltration of fibroblasts and leukocytes. Collagen also penetrates into the suture which may actually reinforce the suture strength (GORE-TEX, 2008). The different suture sizes and their tensile strengths are given in Table 6-1.

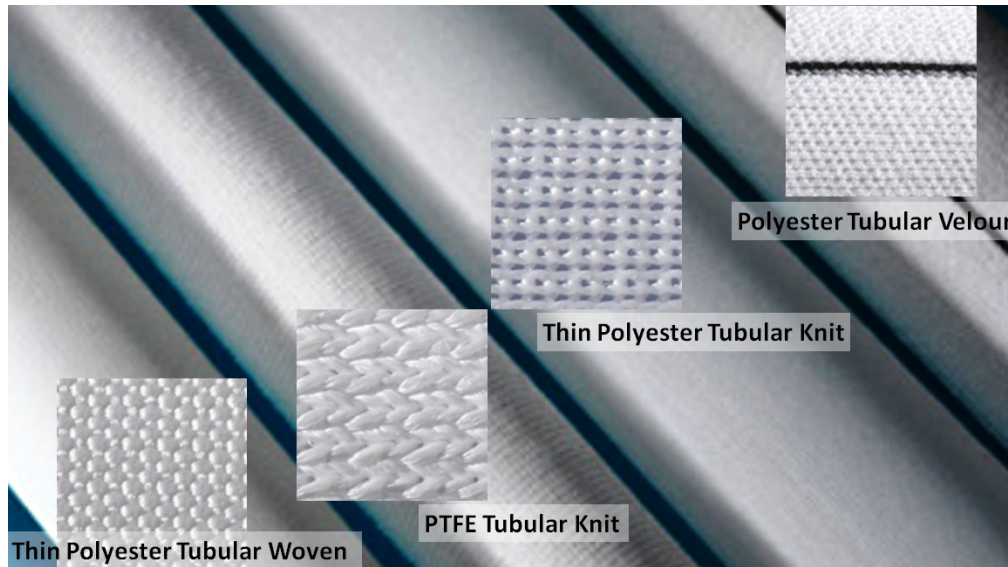
**Table 6-1: Size and strength properties of Gore-Tex<sup>®</sup> sutures**

Gore-Tex <sup>®</sup> Suture Size	Mean suture diameter (mm)	Knot-pull tensile strength (kg)
CV-0	0.626	5.27
CV-2	0.518	3.50
CV-3	0.422	2.64
CV-4	0.307	1.67
CV-5	0.246	1.00
CV-6	0.168	0.65
CV-7	0.109	0.40
CV-8	0.091	0.30

## 6.2 Valve sealing considerations

In order to avert paravalvular leakage, a sealing mechanism is needed which is situated between the prosthetic valve and the native annulus. The material of this mechanism needs to be biocompatible, thus pericardial tissue and biocompatible textiles were considered.

Biocompatible textile tubes from BARD (BARD OEM, 2008) were considered for paravalvular sealing. The different styles and their properties are shown in Figure 6-1 and Table 6-2, respectively. The polyester tubular velour and thin polyester tubular knit tubes were considered for covering the stent. The tubular velour has three distinct black lines to aid in valve alignment during open heart surgery. The tubular knit has a lower wall thickness than the tubular velour. The tubular velour, however, possesses lower porosity which minimizes leakage.

**Figure 6-1: Tubular fabrics**

**Table 6-2: Physical properties of tubular fabrics**

<b>Product style:</b>	<b>Design properties:</b>	<b>Dimensional properties:</b>
Thin Polyester Tubular Woven	Designed for device applications that require a strong thin tubular construction with minimal stretch and low porosity.	Thickness: .010" $\pm$ .001" (single wall) Minimum length: 16" Maximum water permeability: 220 ml/cm <sup>2</sup> /min Nominal diameter range: 14mm – 38 mm
PTFE Tubular Knit	Designed for device applications that require a tubular PTFE construction with minimal seam to prevent disruption of the flow characteristics.	Thickness: .019" - .024" (single wall) Minimum length: 12" Nominal diameter range: 14mm – 30 mm
Thin Polyester Tubular Knit <i>(with maximum stretch characteristics)</i>	Designed for device applications that require a very thin tubular construction.	Thickness: .010" $\pm$ .001" (single wall) Minimum length: 12" Nominal diameter range: 16mm – 36 mm
Polyester Tubular Velour <i>(Fabric incorporates three black lines to provide equidistant reference marks when used to cover mechanical aortic heart valve stents)</i>	Designed for device applications that require a velour surface and stretch characteristics.	Thickness: .047" $\pm$ .010" (double wall) Minimum length: 19.5" Flat tubular width: 1.11" – 1.85"

### 6.3 Valve attachment considerations

Various valve attachment methods were developed and examined, as is shown in Figure 6-2.

Method A consists out of three rectangular tissue sections which are overlapped at the lower part of the valve and attached to the stent while the upper part may be attached by using method B. In method B the ends of the three sections are folded backwards for attachment to the stent which also helps the valve to achieve its closed position. In method C the ends of the three sections are folded backwards twice to reduce the tearing strain on the tissue. Methods D and E use one piece of tissue, shaped into a cylinder. Three of the attachment points are fixed by folding the tissue to provide a double layer for suture attachment. The other attachment point is attached by using one of the previous methods as it consists out of two separate leaflet ends. In most cases the leaflet length in systole,  $L_s$ , is longer than the length of the leaflet at the base, which may require the top section of the cut-out to be longer.

Methods F and G show the attachments of concepts A and B to the bottom of the stent. The suture pierce the tissue twice in order to create a loop over the strut of the stent which ensures a more secure attachment compared to the single piercing through the outer sealing tube, shown in method I.

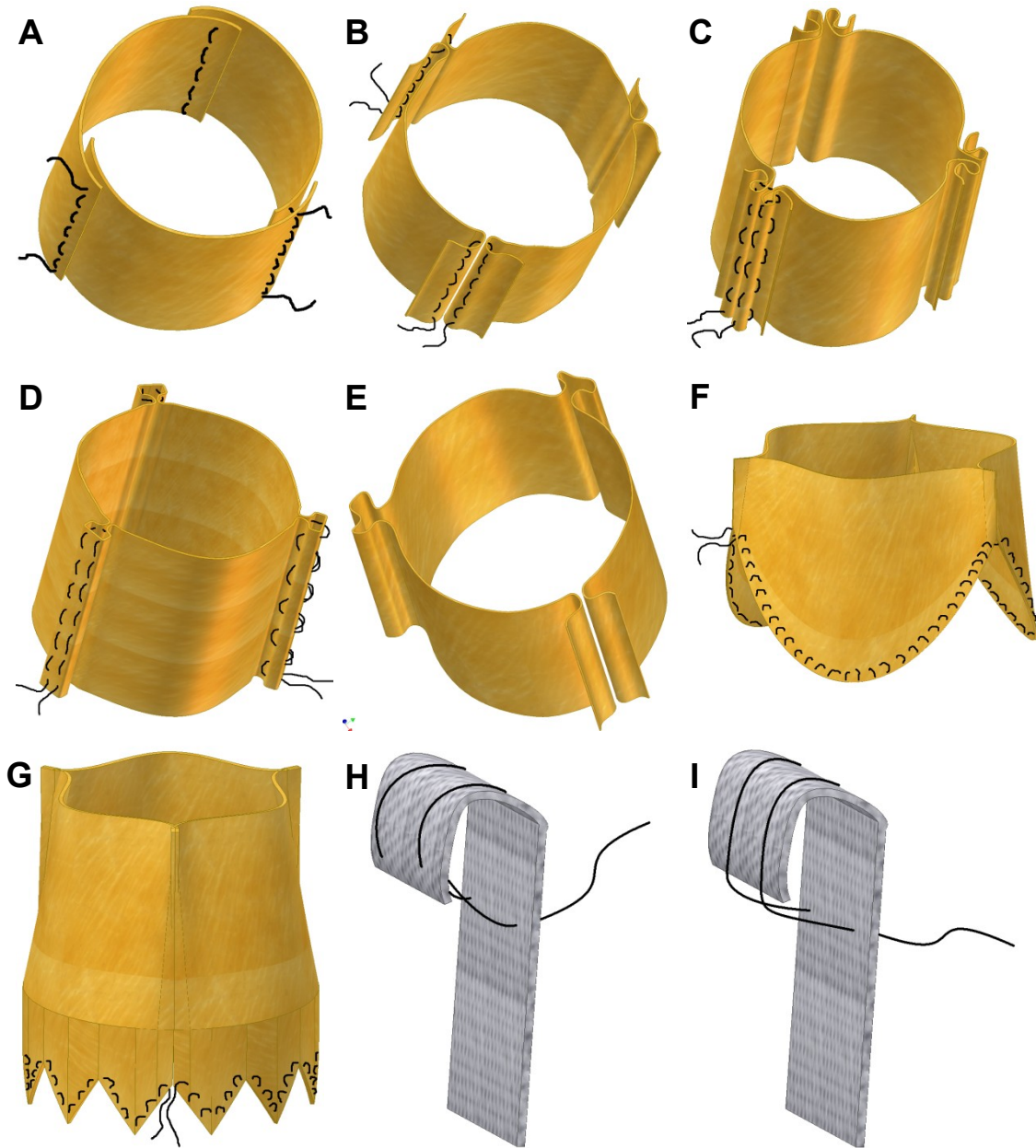


Figure 6-2: Valve attachment methods considered

## 6.4 Valve assembly tools and techniques

Various tools and techniques were developed and investigated to aid in the valve assembly procedure. The relatively small size of the valve also posed some challenges in the design of the assembly techniques and tools.

### 6.4.1 Suturing techniques

Wound closure manuals (Dunn, 2008) and guidelines (Boyer, 2008) were used to investigate the various suture techniques and principles in practice. The various suturing techniques shown in Figure 6-2 were evaluated and the implementation feasibility was investigated. The suturing technique in Method B proved to be adequate and relative easy to implement for the leaflet attachment. Method I proved to be the better technique for attaching the textile tube to the stent as it reduced the appearance of loose ends in the tube. The semicircular shaped needles attached to the sutures worked adequately when using a needle holder or tweezers. Sizes 10 - 13 beading needles however proved to be easier to handle as they are flexible and relative long which enables the manufacturer to use his/her hands instead of pinching tools.

### 6.4.2 Knot consideration

There are a large variety of knots, each with special properties and tasks (Troop7, 2008). The size and strength of the suture knot is mostly interdependent and thus an optimum knot was needed which was strong enough and not too bulky.

There are primarily two kinds of knots used for sutures, namely, the square knot and the surgeon's or friction knot, shown in Figure 6-3. These knots can be tied by hand or by using instruments. The surgeon's knot provides more friction to avert slipping of the knot. When tying in a deep cavity where it is impossible to pull the two strands apart, a deep tie is used. A granny knot occurs when the stands of a square knot are inadvertently crossed incorrectly which leads in a knot that may slip. All these techniques are described in detail by surgical knot guidelines (Johnson&Johnson, 2008). Gore-Tex<sup>®</sup> proposed the square knot for its ePTFE sutures where alternative directions of each throw with even tension parallel to the previous throw is applied. Four to six throws was found to be adequate for a secure square knot, depending on the suture thickness.

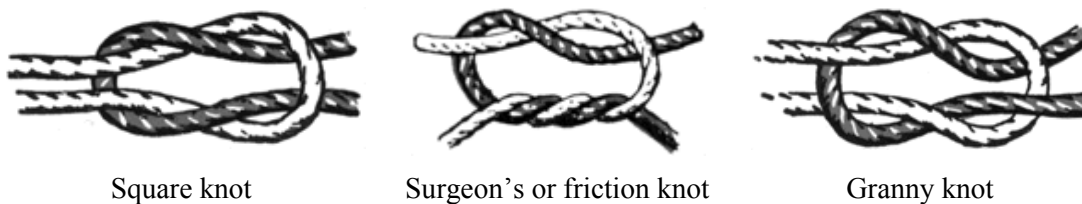


**Figure 6-3: Suture knots (Troop7, 2008)**

### 6.4.3 Assembly tools developed

The design and performance parameters in Table 5-1 were used as inputs for leaflet cut-out geometry shown in Figure 6-4. Extra tissue was added to provide appropriate attachment to the stent.

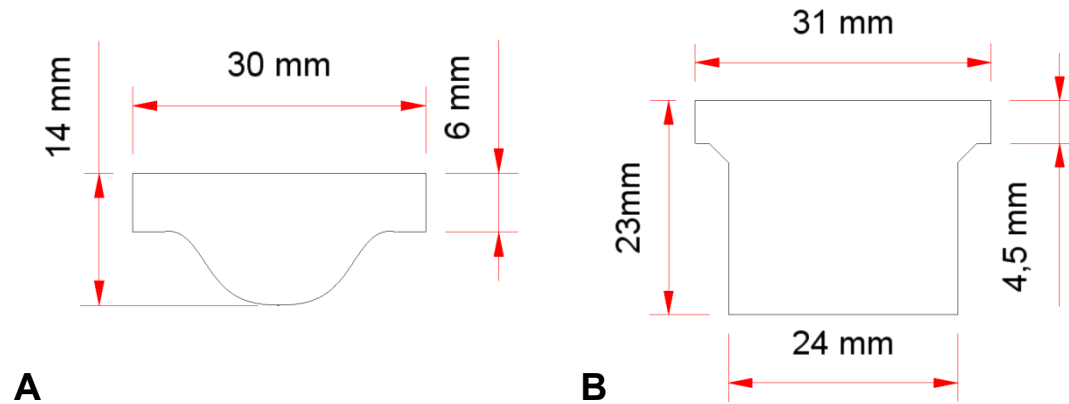


**Figure 6-4: The leaflet cut-out geometry for concepts A and B**

Stainless steel stencils with the geometries shown in Figure 6-4 were laser cut to provide templates for cutting out the leaflets. Two different custom made tweezers were developed to aid in the assembly of the valves. The tweezers are made from two identical laser cut stainless steel sections which are spot welded together. Both tweezers have grooves cut into their tips with the one having teeth for guiding the needle. A circular plate with a groove was used to lock the tweezers in position during assembly. The purpose of these tweezers, which are shown in Figure 6-5, is mainly to clamp the leaflet tissue to the stent during assembly and to guide the needles. The tweezers proved to be very helpful in improving accuracy and reducing assembly time.



**Figure 6-5: Custom made tweezers for valve assembly**

#### 6.4.4 Assembly procedures

The valve attachment methods shown in Figure 6-2 were considered for the valve assembly. After some consideration and trials some suitable techniques and procedures were found and are shown in Figure 6-6.

The stainless steel templates were used along with a scalpel to cut out each leaflet, as shown in picture A. It was found that rolling rather than dragging the scalpel over the tissue resulted in a better cut and reduced the sliding of the tissue underneath the template. The fibre alignment of the tissue was chosen to lie in line with the circumferential direction of the valve. It was also found that one side of the tissue was smooth while the other side possessed a fibrous surface texture, almost like leather. The fibrous side was chosen to be situated on the stent or outer side of the leaflet in order to use the smooth side for sealing between the leaflets. Pictures B and C shows the placement of two leaflets on the toothed tweezers and the stent with the help of a normal pair of tweezers. Picture D shows how the toothed tweezers are used to clamp the tissue leaflets to the stent and guide the needle. A conventional pair of tweezers could be used to keep the leaflet out of the needles path when the needle is pushed in from the outside.

The attachment methods B and G in Figure 6-2 were used for concept B in Figure 5-7. It was also found that the combination of methods A and B was also easy to implement for concept B where method B was used for the attachment of the top section. The CV-7 sutures from Gore-Tex<sup>®</sup> were found to be adequate for suturing method B while ranges CV-3 to CV-5 proved to be adequate for method G, as only three suture loops were made per strut.

Picture E shows the three leaflets of concept A being attached to each other by using the pair of toothed tweezers. The leaflets are first attached to each other because the diamond shaped stent does not have specified holes for attachment. This attachment is done in such a manner that the length of tissue between each attachment line is equal to the leaflet length at systole or  $L_s$  calculated in section 5.5. Attachment methods B and F in Figure 6-2 were used for the construction of concept A. Method I was used to attach the textile tube to the stent. CV-7 sutures were used for the leaflet attachment while CV-6 sutures were used for attaching the textile tube to the stent. Picture F shows the attachment of the leaflet and textile tube to the stent using a beading needle and the toothed tweezers.

It should be noted that the tissue first needs to be rehydrated as stipulated in section 2.6 before use. The tissue also needs to be kept moisturized during assembly. After assembly is finished, the valves are stored in one of the alcohol solutions described in section 2.6. Care should also be taken in order not to damage the tissue with the tools.

## VALVE MANUFACTURING

The three different manufactured valves are shown in Figure 6-7 corresponding to concepts A, B and C in Figure 5-7. It should be noted that one prototype of concept C was manufactured, but it was found that its outer surface did not provide enough fixation due to the smooth surface texture of the tissue. The manufacturing of each valve took approximately six to eight hours.

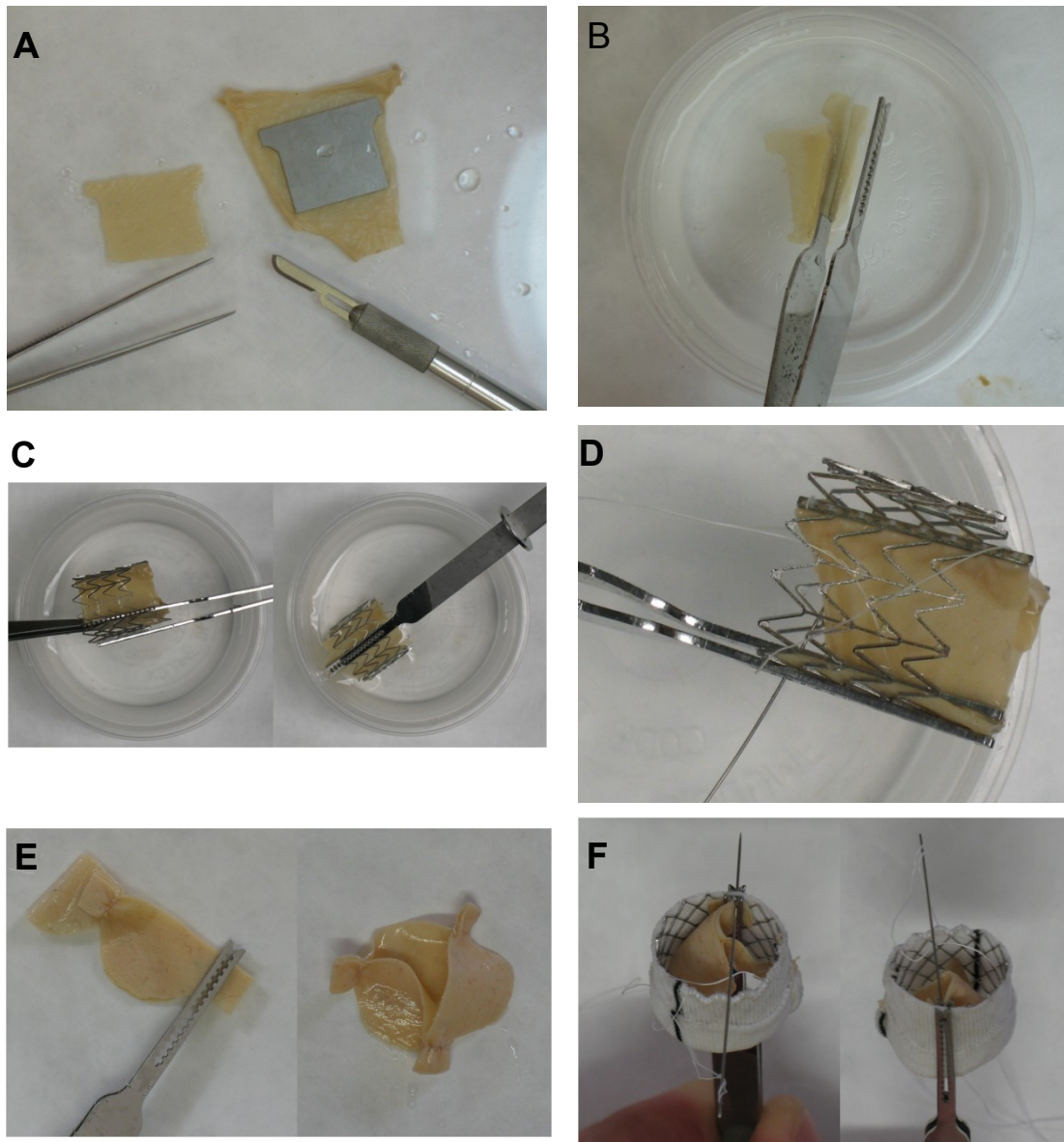


**Figure 6-6: Valve assembly procedures**

VALVE MANUFACTURING

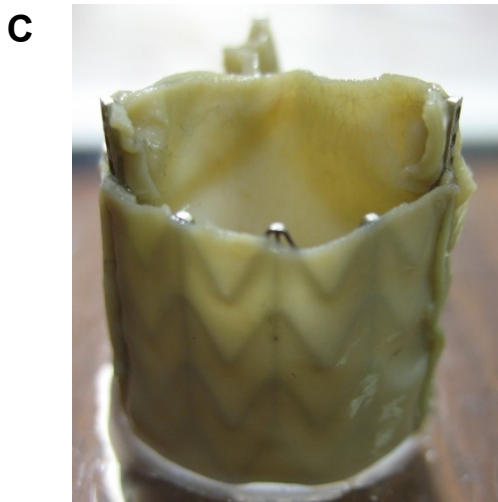
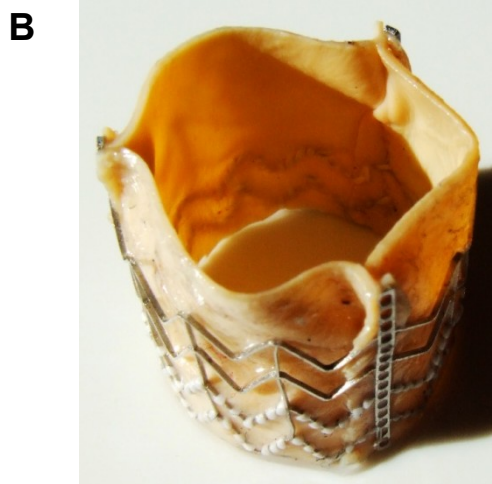
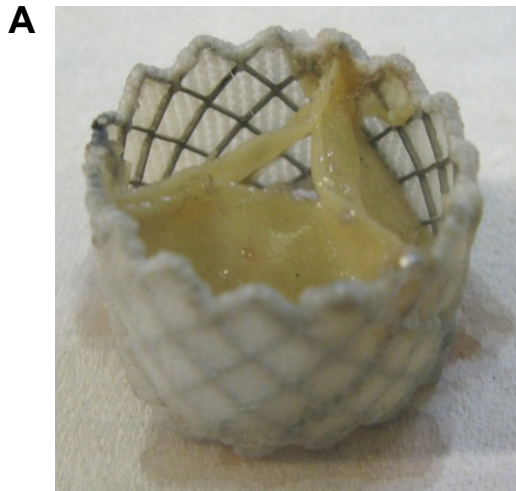


**Figure 6-7: The three different manufactured valves**

## CHAPTER 7

### 7. FINITE ELEMENT ANALYSIS (FEA) OF VALVE

Finite element analysis was used to aid in the evaluation of concepts A and B. Both normal and hypertensive pressure differences across the valve were examined by using static analysis. This was simulated for diastole when the maximum pressure difference across the valve occurs. The valve material orientation as well as the use of different material properties for each leaflet was investigated to determine its influence on the valve performance. The allowable over and under dilation, along with unsymmetrical dilation were also investigated. The leaflet attachment forces were determined to investigate the probability of tissue tearing. Finally the stress distribution across the leaflet was examined.

#### 7.1 FEA implementation

The same FEA implementation technique used in section 4.2 was used for the valve simulations. The geometries derived in section 5.5 were used to construct the FE models for concepts A and B, as are shown in Figure 7-1. Conventional aortic valve simulations are performed by either using an open or closed valve geometry, constructed according to the native aortic valve geometry. The aim in this study was to construct the FEA geometry in such a way that it resembles the geometry of the valve prosthesis as much as possible. This ensures a more accurate simulation, because the initial leaflet geometry resembles the semi-relaxed state of the valve, with minimal prestresses in the leaflet.

Contact analysis was used to accurately simulate the interaction between the leaflets. Five integration points through the leaflet thickness were used for all the simulations. Translation constraints were placed on lines of attachment to the stent. A uniform pressure load was placed on the top of each leaflet. A cylindrical coordinate system was placed in the centre of the valve to act as the material orientation system. Concept A consisted out of 3480 elements and concept B out of 5496 elements.

#### 7.2 Extreme pressure simulations

The ISO standards for conventional heart valve prostheses (International Organization for Standardization, 2005) states that a heart valve substitute must be able to withstand a single maximum cycle consisting of a pressure difference of 230 mmHg across the valve. Both concepts A and B were subjected to this pressure during the finite element analysis. Kim *et al.* (2006) investigated the bioprosthetic heart valve function using the Fung constitutive model for the opening of the valve during systole. It is known that the highest stresses in the valve tissue occur during diastole which is the reason why the closure of the valve was simulated in this study.

## FINITE ELEMENT ANALYSIS (FEA) OF VALVE

Both concepts were simulated using the bovine and kangaroo material properties as well as a hypothetical isotropic material with a modulus of elasticity of 5 MPa and a Poisson ratio of 0.3. A leaflet thickness of 0.16 mm was used for all simulations.

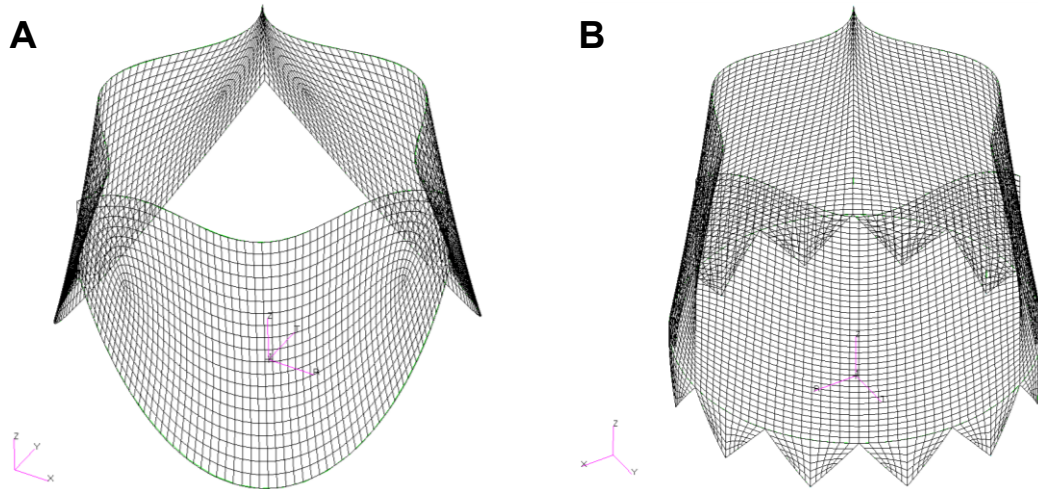


**Figure 7-1: Finite element models for concepts A and B**

The simulated distortion and predicted maximum von Mises stresses are shown in Figure 7-2 and

Table 7-1, respectively. Concept B presented higher stress concentrations for all cases, especially at the base, and significant folding in the corners which are some of the primary causes of mechanical damage on the valve leaflets (Smith *et al.*, 1999) and (Thubrikar, 1990).

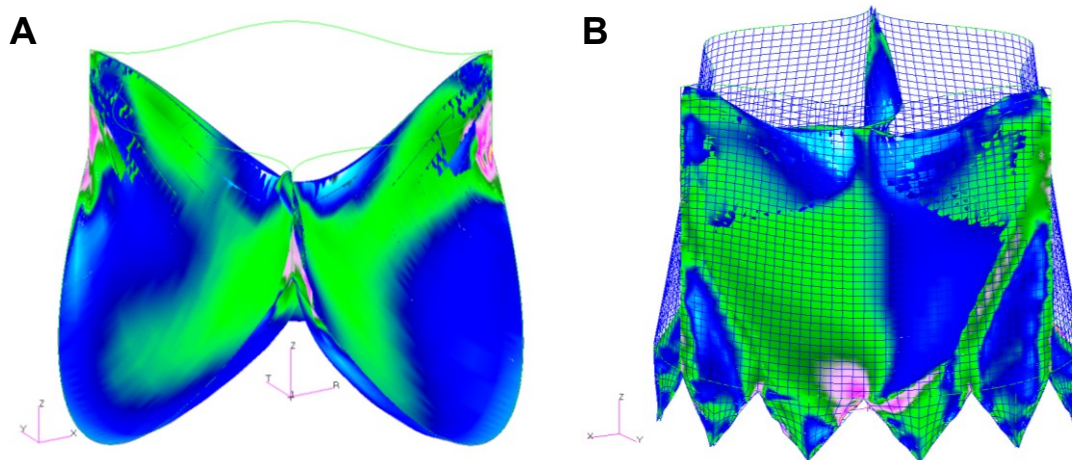


**Figure 7-2: Finite element simulations for concepts A and B under hypertensive pressures**

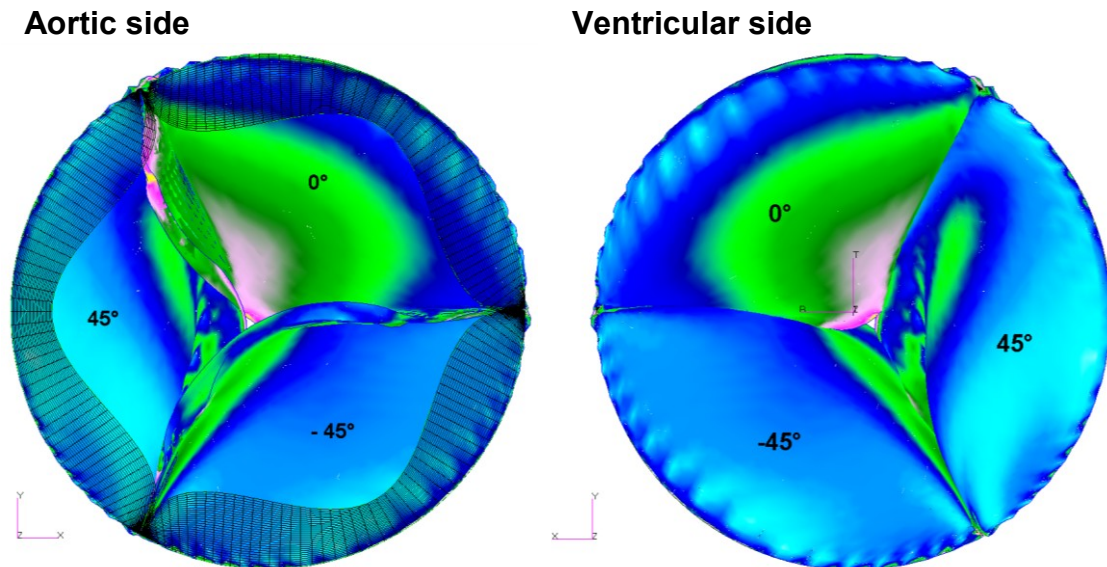
**Table 7-1: Maximum von Mises stresses for various material properties**

Concept	Bovine (MPa)	Kang (MPa)	5 MPa Isotropic (MPa)
A	13.7	6.67	3.18
B	42.8	34.1	7.29

### 7.3 Material orientation

It is known that the pericardial tissue used for the construction of the valves have distinct fibre orientations. It was decided to use the same fibre orientation during valve manufacturing as found in native aortic valves, which is primarily in the circumferential direction. The effects of manufacturing the valves using different fibre directions were investigated using finite element analysis.

Each leaflet was given a different fibre direction of  $0^\circ$ ,  $45^\circ$  and  $-45^\circ$  measured from the circumferential direction, respectively. A normotensive pressure of 95 mmHg was placed on the valve. The leaflets had a thickness of 0.35 mm and Bovine was chosen as the valve material. It was found that the leaflets did not close at the same rate which caused unsymmetrical valve closure and folding in some leaflets, as is shown in Figure 7-3.

**Figure 7-3: The effects of leaflet material orientation on valve closure**

## 7.4 Different leaflet material

As there was a high degree of variability between the material properties of different pieces of pericardium from the same material (see Appendix A), it was necessary to investigate the valve function when the leaflets are not manufactured from one piece of pericardium. Arcidiacono *et al.* (2005) did dynamic simulations on an aortic heart valve of which the leaflets were given different mechanical properties. They found the occurrence of asynchronous leaflet movements. Simulation of a valve that is constructed out of two different pieces of pericardium was performed.

The material parameters of two different kangaroo tissue tests were used for the simulation. Two leaflets had identical material parameters (Kang #1, Appendix A) while the third had a different set of parameters (Kang #3) assigned to it. The leaflets were given a thickness of 0.16 mm and were subjected to a hypotensive pressure of 50 mmHg. It was found that with these specific parameters the one leaflet had less extension than the others which caused the valve to close unsymmetrically. The result was that the centre of valve closure was shifted away from the centre, as shown in Figure 7-4.

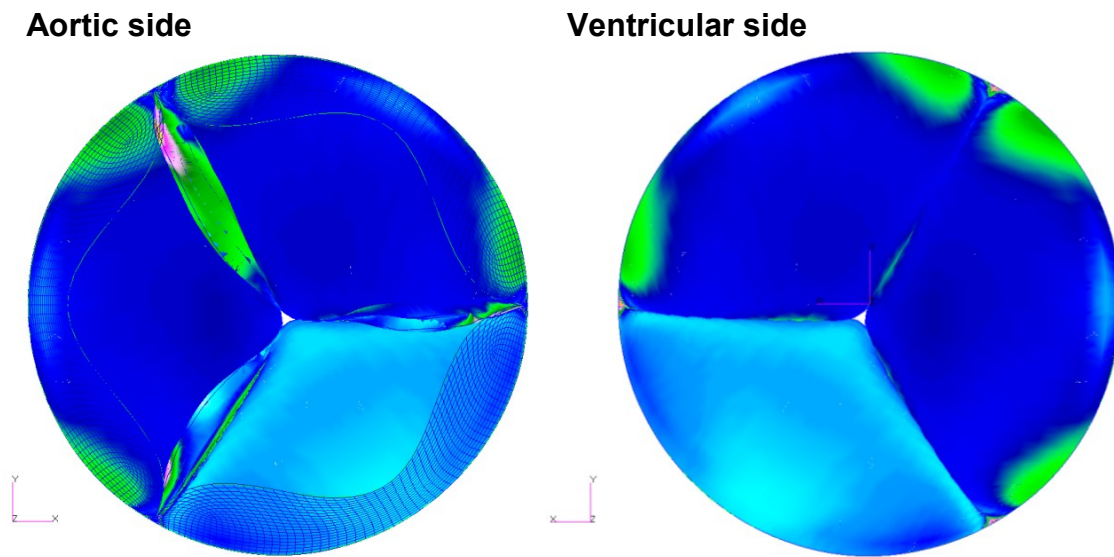


Figure 7-4: The effects of different leaflet material on valve closure

## 7.5 Over and under dilation of the valve

Due to the fact that percutaneous aortic heart valves are expandable and only limited size ranges are manufactured, the valve must be able to withstand over and under dilation to ensure a secure fit. Simulations were performed to find the maximum over and minimum under expansion the valve can tolerate, that will still allow it to operate effectively.

Valve dilation was simulated for ranges -1.0, 1.0, 2.0 and 4.0 mm relative to the valve diameter. The simulations were performed by applying a hypotensive pressure of 50 mmHg to the valves to ensure valve closure under lower pressures. The leaflets were given a thickness of 0.16 mm. Two load steps were used in the simulations, where the first applied the dilation, and the second one the pressure. It was found that the gap in the centre of the valve increased in size during over dilation and the presence of leaflet folding occurred during under dilation, as is shown in Figure 7-5.

The simulations were compared with the normal valve simulations and it was found that the gap in the centre was still reasonably small at an over dilation of 2.0 mm for concept B. This is due to the extensibility of the kangaroo pericardium along with the fact that concept B had a larger leaflet height than concept A. The gap in the centre of concept A was larger compared to Concept B. It should be noted that both concepts had the same leaflet length during systole. Folds were already present in the 1.0 mm under dilation of both valves, with B possessing more distinct folding. The over and under dilation of the valves is shown in Figure 7-5.

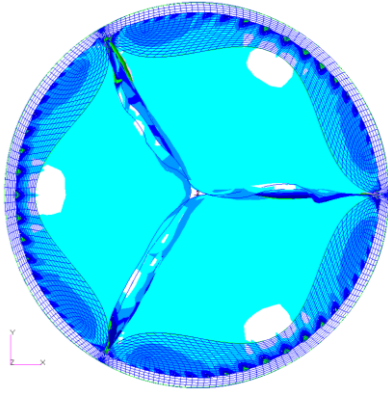
## 7.6 Unsymmetrical dilation of valve

It was found while expanding the manufactured valves with a balloon, the stent occasionally experienced unsymmetrical expansion. The reason for this may be the complex interaction between the folded balloon and the stent during expansion. Another cause of unsymmetrical expansion may be the irregular geometry of a calcified native valve annulus, as is shown in Figure 2-2.

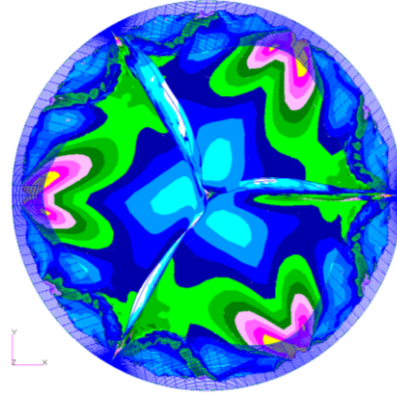
Unsymmetrical expansion of the stent was simulated by expanding one third of the valve using a quadratic function of the form  $y = \frac{1}{a^2}x^2$ , where  $a$  is the number of stent attachment points in one half of the section and  $x$  is the stent attachment point number starting at 1. This produced the irregular expansion of one third of the valve with a maximum expansion of 1 mm in the centre of the section, as shown in Figure 7-6. The simulations were performed by applying a hypotensive pressure of 50 mmHg to the valves to ensure valve closure under lower pressures. The leaflets were given a thickness of 0.225 mm and the Bovine #2 material properties given in Appendix A was used for the simulation in Figure 7-6.

The unsymmetrical dilation caused the valve's centre of closure to be off-centre. The valve still closed effectively with the 1 mm unsymmetrical expansion.

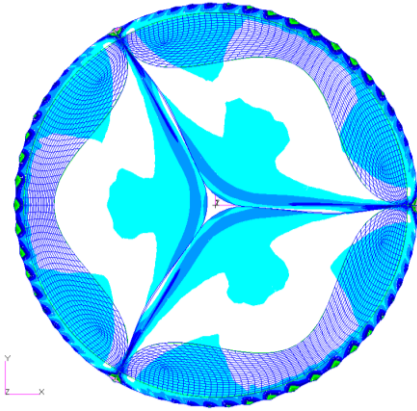
1 mm under dilation of A



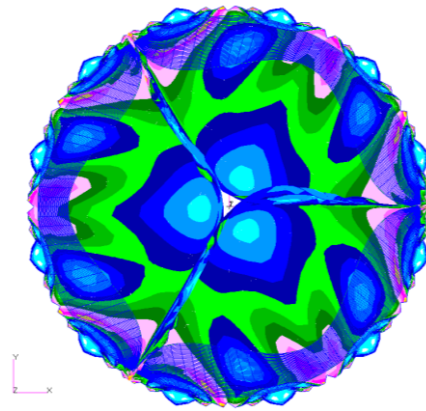
1 mm under dilation of B



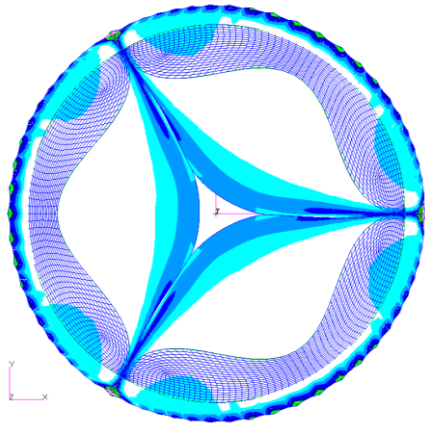
1 mm over dilation of A



1 mm over dilation of B



2 mm over dilation of A



2 mm over dilation of B

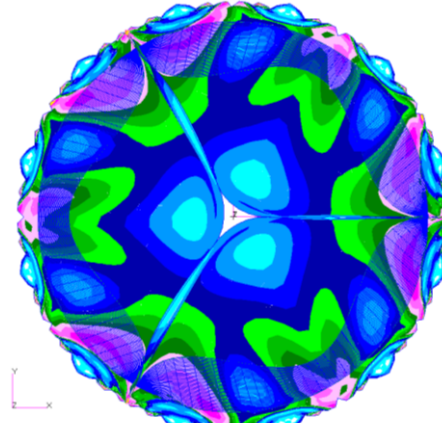
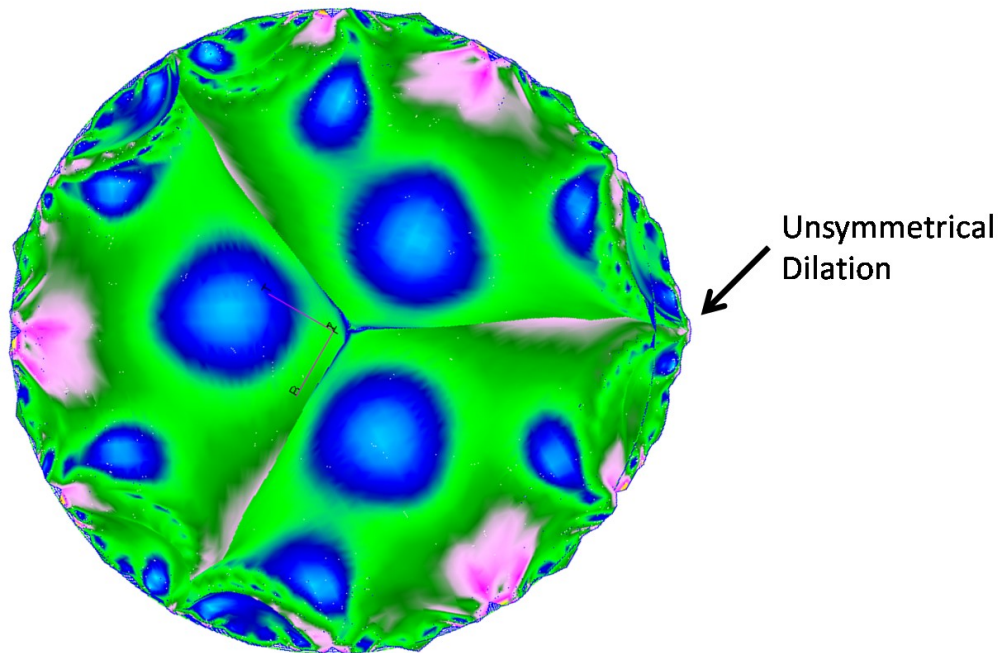


Figure 7-5: Over and under dilation of valves



**Figure 7-6: Unsymmetrical dilation of the valve**

### **7.7 Leaflet attachment forces**

The attachment forces induced by the valve on the stent were calculated in order to determine whether the sutures and tissue are strong to handle the loads. These simulations were also used as an aid in finding a suitable suture density.

Suture densities were found during valve manufacturing as those that ensured a secure and tight attachment for suture thicknesses and attachment methods used. Each attachment point consisted out of two tissue piercings as shown in Figure 6-2, pictures A, B, F and G. Concept A was constructed using approximately five attachment points on each of the three sides and twenty-three attachment points on the base of the valve, as indicated by the square markers in Figure 7-7. Concept B had ten attachment points on each side and three attachment points on each “zigzag” strut of the stent.

The attachment forces were determined by constraining certain nodes in the simulations to act as the suture attachment points, as shown in Figure 7-7. A maximum pressure of 230 mmHg according to the ISO standards was placed on the valves. It should be noted that the nodal attachments on the sides of the valves constitute loads for the two leaflets connected to it. The maximum nodal attachment force for concept A was 1.3 N and was located at the highest attachment point of the valve. Thus the force per leaflet at that attachment was 0.65 N. The maximum nodal

attachment force at the base was 0.16 N. The maximum nodal attachment force for concept B at the sides was 1.05 N and was also located at the highest attachment point of the valve. Thus the force per leaflet at that attachment was 0.53 N.

The maximum nodal attachment force at the base was 0.64 N and was located on the central tip of the “zigzag” strut configuration.

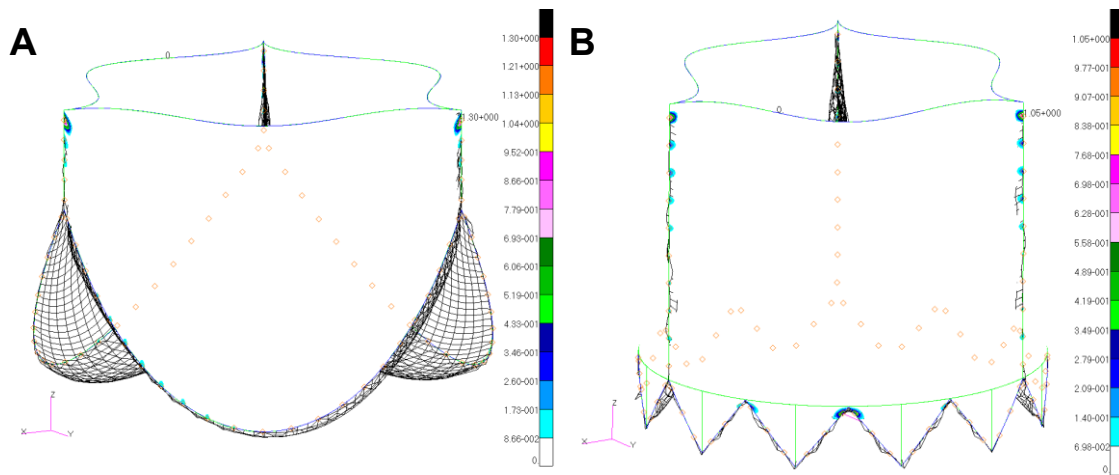


**Figure 7-7: Attachment forces for concepts A and B**

## 7.8 Stress distribution across the valve leaflet

The stress distribution across the valve leaflet for the circumferential and transverse directions was examined. An isotropic material model with an elasticity modulus of 5 MPa and a Poisson ratio of 0.3 was used for the simulations. A normotensive pressure of 95 mmHg was placed on the valve and the leaflets were given a thickness of 0.16 mm.

It was found that the circumferential stress distribution was predominantly higher than the transverse stress distribution at the vertical attachments and the “belly” region of the valve as is shown in Figure 7-8. The circumferential stresses at the vertical attachments were however the largest of all the stresses. This indicated that stresses could be reduced by aligning the fibre direction in the circumferential direction. The fibres in a native valve are aligned to compensate for high stresses in certain regions of the leaflet (Sacks *et al.*, 1998). It is however only possible to manufacture valves of which the fibre direction is primarily aligned in one direction.

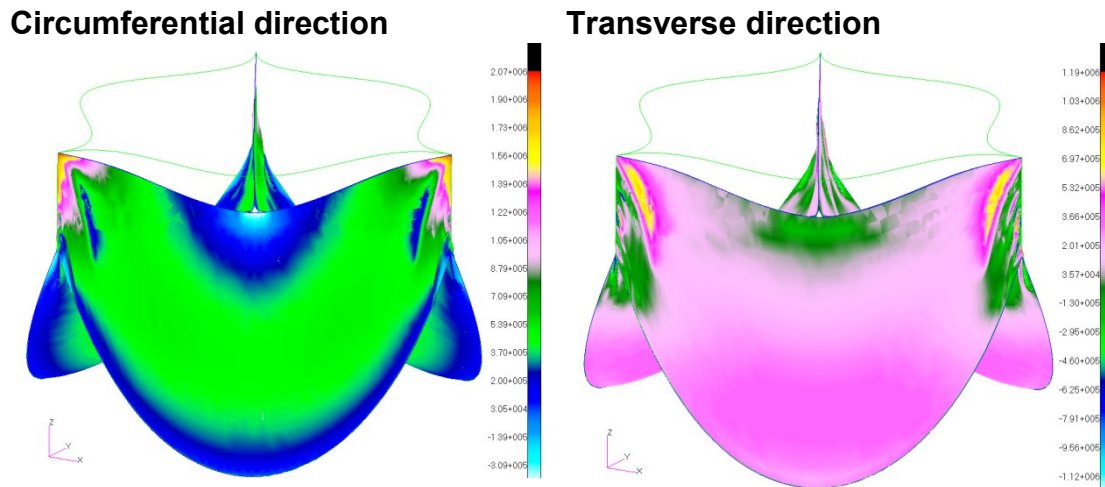


**Figure 7-8: Stress distribution across the valve leaflet**

The FEA simulations proved to be a valuable tool in evaluating valve geometries and the materials considered. It also assisted in the evaluation of the suture density and fibre orientation. In this analysis, the leaflets were subjected to a uniform pressure load on the aortic side during the closing phase of the valve. A fluid-structure interaction model could provide a more realistic analysis as a result of fluid flow patterns that may vary in different regions. The material properties were also assumed to be homogeneous through the entire leaflet. Due to the complex geometry and material properties of aortic valve prostheses, FEA is limited by only being a valuable initial design tool, and rigorous testing of valve prostheses is still required in order to determine unforeseen causes of failure.

## CHAPTER 8

### 8. TESTING AND RESULTS

The manufactured valves were tested by doing in vitro tests in a pulse duplicator. The crimping diameters of the valves were also investigated along with deployment tests in a sheep heart. Rupture tests were performed on the tissues used for valve manufacturing to compare the attachment loads with those given by the FEA simulations. The need for calibrating the digital camera was also investigated.

#### 8.1 Camera calibration testing

The influence of camera calibration on the biaxial testing data was investigated by comparing the original points with the calibrated points as shown in Figure 8-1.

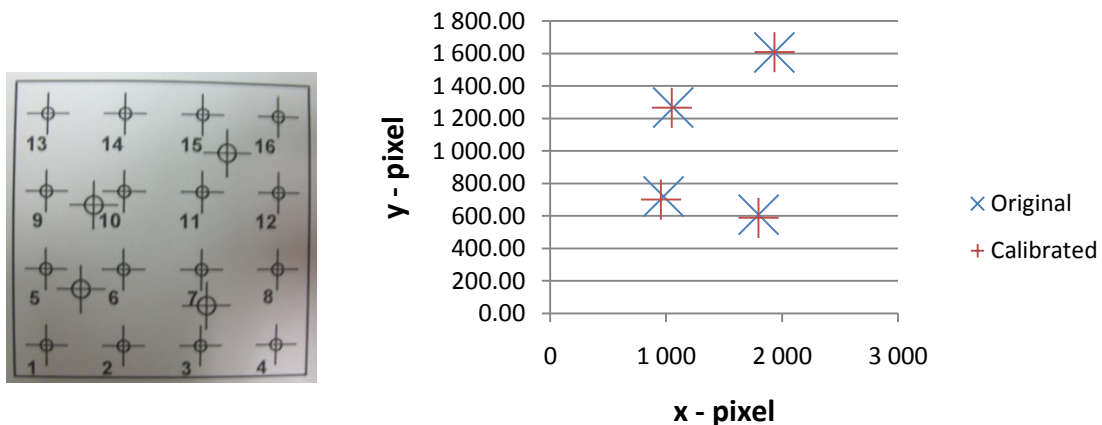


**Figure 8-1: Original and calibrated camera points**

The digital camera was found to have little lens distortion which could eliminate the need for camera calibration. The specific test shown in Figure 8-1 indicated that there was a strain error between the original and calibrated points of 0.007 for both normal strains and an error of 0.0007 for the shear strain. This produces an error of approximately 2.3 % in normal strain measurements and 0.7 % in shear strain measurements.

#### 8.2 Rupture tests

The suture density used in the valve assembly was primarily determined during the physical valve construction. Factors like space restrictions and gap forming when tension was applied to the leaflets contributed to choice of final suture density. Tearing of the leaflet at the attachment points may be one of the causes of valve

failure. The suture weakens the tissue and reduces the effective load carrying connection area at the attachments. García Páez *et al.* (2003) compared the mechanical behaviour of biological tissues sutured with Gore-Tex<sup>®</sup> and subjected to uniaxial tensile testing. Lim and Cheong, (1994) did uniaxial tests on bovine pericardium strips cut along three different axes. They found that suturing lowered the strength of the tissue and that tissue with thicker sutures ruptured at significantly lower stresses. All of the above research was conducted by stitching two pieces of tissue together.

The attachment forces found in section 7.7 needed to be compared to experimental tests in order to authenticate the suture density used. Rectangular pieces of tissue each with a length of 25 mm and a width of 5 mm were used for the tests. CV-5 Gore-Tex<sup>®</sup> sutures were stitched through the tissue by piercing it twice, as shown in Figure 8-2, which resembles one attachment point. The pair of toothed tweezers was used to insert the stitches of which the two piercings were approximately 1.3 mm apart and 1.6 mm from the tip of the sample. These dimensions corresponded to that used during valve assembly. Ten samples each of the bovine and kangaroo tissues were tested. The fibre direction of one half of the samples was chosen along the longitudinal direction while the other half was chosen along the transverse direction of the sample.

The tearing load was plotted against the tissue thickness as shown in Figure 8-3. The data tended to form a linear relation and no significant differences were observed between the two different fibre directions. The minimum tearing load for kangaroo was found to be 2.79 N and is thus 4.3 times larger than the highest attachment force calculated in section 7.7. The minimum tearing load for bovine was found to be 4.71 N and is thus 7.2 times larger than the highest attachment force determined in section 7.7. The FEM determined attachment forces were also found to be significantly smaller than the suture tensile strength shown in Table 6-1.

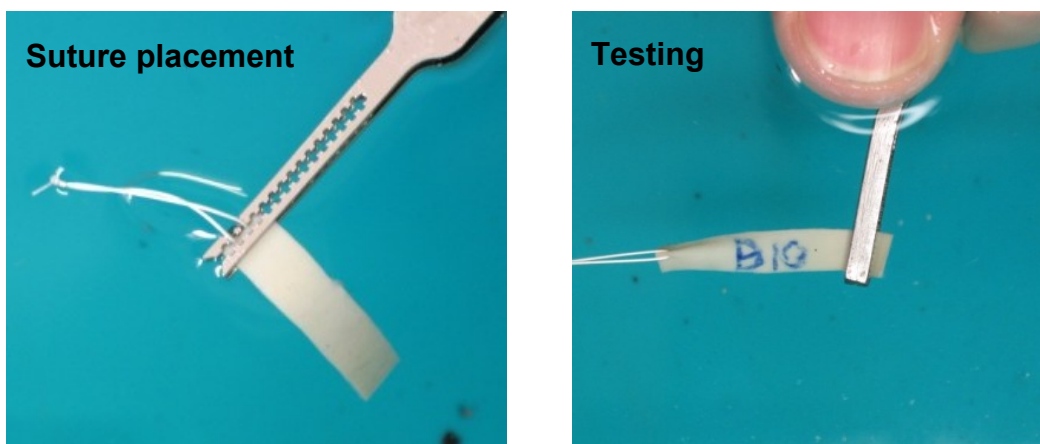


**Figure 8-2: Tissue rupture tests**

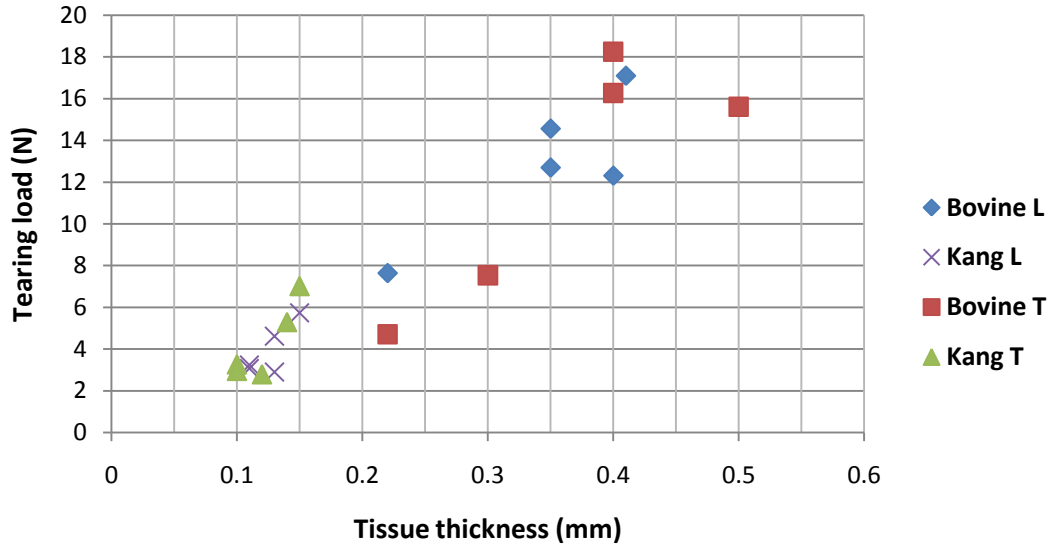


**Figure 8-3: Tearing loads of pericardium for various tissue thicknesses with fibre alignment in the longitudinal and transverse directions**

### 8.3 Pulse duplicator tests

In vitro tests were conducted in a pulse duplicator and the valve geometry was monitored during systole and diastole. Figure 8-5 shows concept A using kangaroo tissue being tested. Both valves, (concepts A and B), were subjected to stage 4 hypertensive pressures of 185 mmHg and above, as shown by the pressure curves in Figure 8-5. The pulse duplicator was designed as part of this project by Mr. H. Krynauw at the University of Cape Town

The pulse duplicator was only able to operate for short periods during the time of testing, due to mechanical defects. This only allowed testing of approximately five minutes per valve. Both concepts however proved to close properly and there were no indications of failure following the tests. Concept A proved to have better fixation properties, and concept B tended to migrate at high pressures. It was also observed that the specific valve shown in Figure 8-4 had one leaflet that was longer than the others which created folds, and an offset from the centre during closure. This indicates the need to improve repeatability and consistency during manufacturing. Despite this geometrical irregularity, the valve was still able to operate effectively. It can also be seen from Figure 8-4 that there was no folding in the other two leaflets and that the valve had a large orifice area during systole, which is an indication of a potentially low mean pressure difference during forward flow.

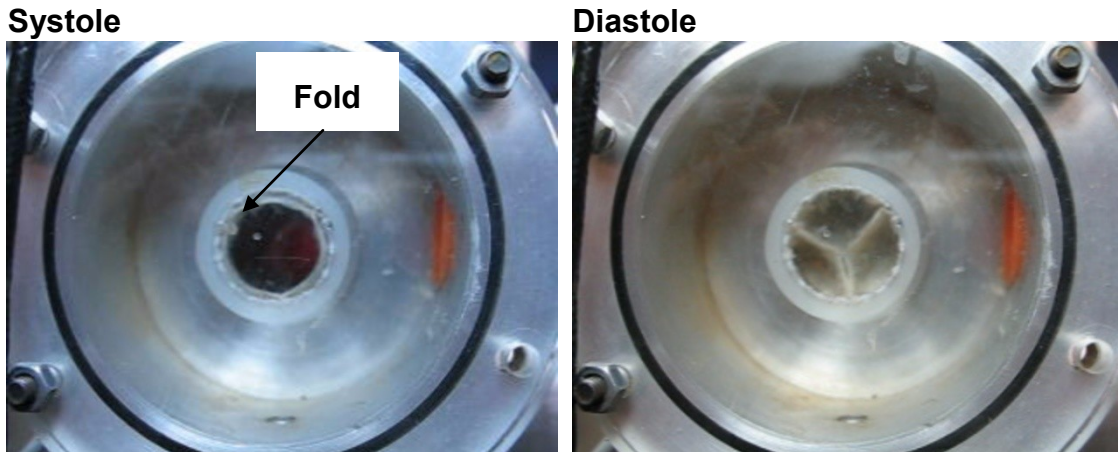


Figure 8-4: Concept A during pulse duplicator tests showing the systole and diastole

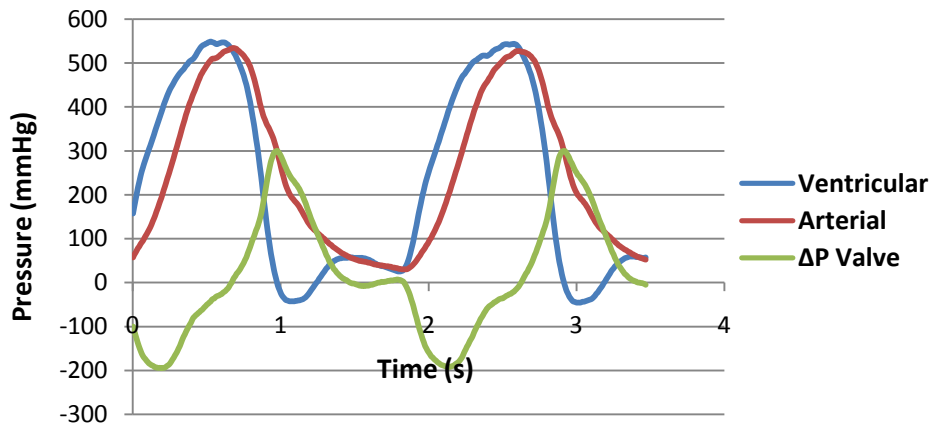


Figure 8-5: Pressure curves of pulse duplicator tests

### 8.4 Crimping diameter

The crimping diameter of the valves was measured in order to evaluate the designs and to find possible improvements. The valves were crimped over an 18 mm Z-MED™ percutaneous transluminal valvuloplasty catheter balloon. The folded diameter of the balloon is approximately 3 mm.

Concept A was crimped to a diameter of 6.75 mm (20.25 French) and concept B to 7.5 mm (22.5 French). Concepts A and B had leaflet thicknesses of 0.15 mm and 0.25 mm, respectively. Pictures of the valves in their crimped states are shown in Figure 8-6. A variation of concept A for which thin tubular knit was used for the outer sealing of the valve was also crimped and delivered a crimped diameter of 5.8 mm (17.4 French).

It was found that the sutures, sealing material and strut geometry restricted the crimping of concept A more than the balloon and leaflet on the inside. It was also found that the sutures at the base of concept B constrained the tissue in that area which resulted in crimping restrictions, shown in Figure 8-6. The valves also tend to recoil when crimped which may indicate the need for the use of a sheath over the valve during delivery. The sheath may also allow the valve to be crimped to an even smaller diameter by eliminating the occurrence of recoil.

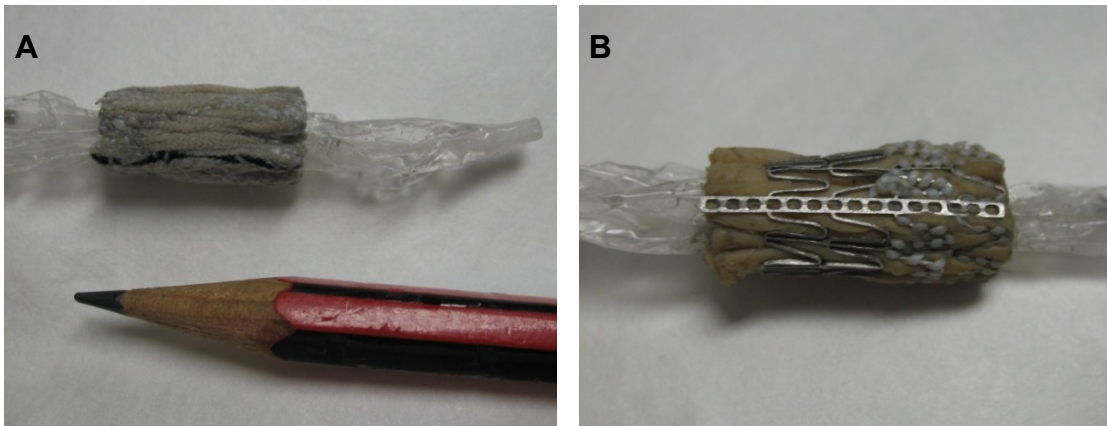


**Figure 8-6: Crimping of concepts A and B**

## 8.5 Deployment tests

The dimensional interaction of the valves with their operating environment was investigated by placing the valves in a sheep heart, as shown in Figure 8-7. The black wire in the image on the left was used to indicate the position of the coronary ostia.

It was found that concept A possessed a greater possibility to obstruct the coronary ostia due to its higher sealing distance. However, this property made the valve less susceptible to paravalvular leakage due to its greater sealing area and the fact that the sealing tube is situated on the outside of the stent. Concept B proved to be less obstructive to the coronary ostia as long as the valve is rotated in such a manner that the valve commissures do not interfere with the coronary ostia. It was found that care should be taken during deployment in order not to interfere with the mitral valve.

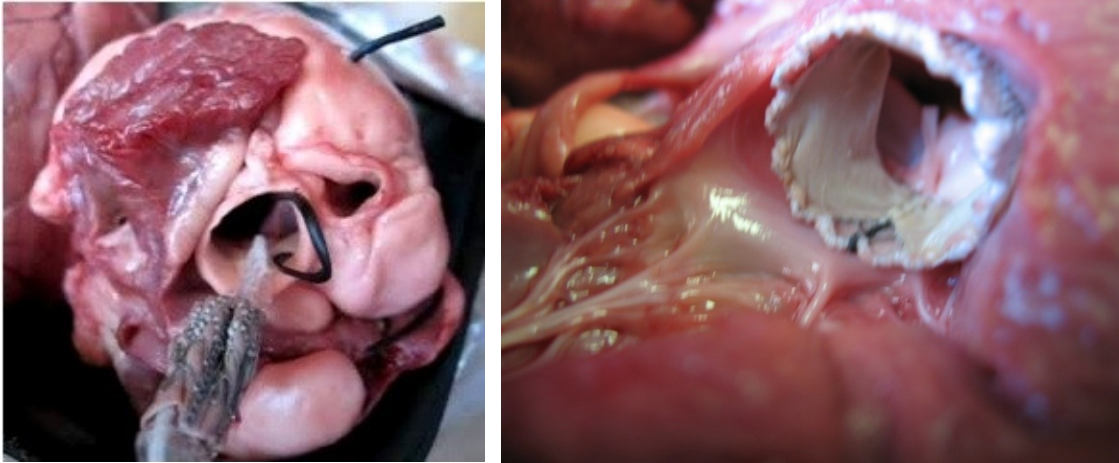


**Figure 8-7: In vitro deployment of concept B (left) constructed out of bovine and concept A (right) constructed out of kangaroo in a sheep heart**

## CHAPTER 9

### 9. CONCLUSIONS AND RECOMMENDATIONS

#### 9.1 Thesis goal and outcome

The goal of this thesis was the testing and comparison of a newly developed tissue and its use in the manufacturing of tissue leaflets for a percutaneous aortic heart valve. Concepts for valve geometries were developed and investigated by using valve design requirements and improving on existing valve limitations. Repeatable and reliable manufacturing techniques and tools were developed. Prototypes of valves were manufactured and evaluated by using numerical simulations and experimental testing.

Although rigorous fatigue testing in a pulse duplicator was not performed due to time constraints, the experiments conducted proved that the developed concepts were feasible with no prominent defects. Although the majority of the design requirements were used as design inputs during concept development, the actual testing of all of the requirements could not be performed.

#### 9.2 Challenges, future improvements and recommendations

The tendency of the Fung constitutive model to be unstable posed challenges in its FEM implementation. The moderately large difference in material properties between various tissue samples, along with scattered and uneven fibre directions, also posed some challenges. More rigorous experimental determination of the material properties could improve the accuracy of the material characterisation. The assembly of the valves requires expertise that can only be achieved with experience. The manufacturing is done manually which poses some repeatability issues; however the special tools developed improves the repeatability to some degree.

Future improvements on the valve design may be a second iteration of the stent and valve geometry design in order to achieve more ideal performance parameters for the valve. A larger scale of manufacturing is also needed to evaluate and refine the manufacturing techniques and repeatability. The stainless steel stencil used for cutting out the leaflets can also be replaced by a CNC manufactured hollow punch as shown in Figure 9-1 in order to improve repeatability and provide leaflets with more even edges.

Testing in a pulse duplicator is recommended whereby fatigue, durability and leakage tests can be performed. A preclinical animal study in sheep must be performed in order to examine the valve's biocompatibility, placement and resistance to calcification.

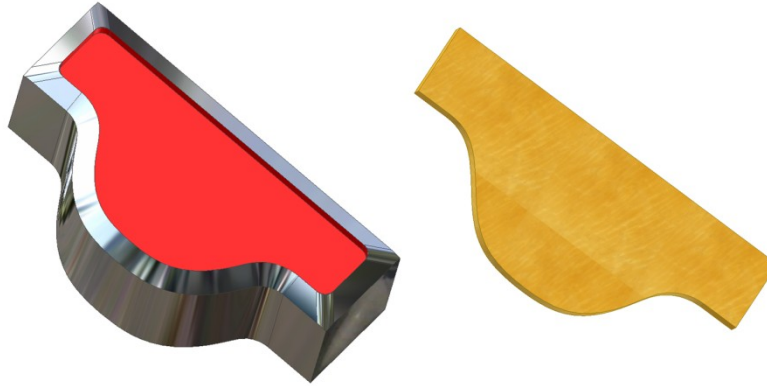


**Figure 9-1: Hollow punch for cutting out valve leaflets**

### 9.3 Conclusion

Aortic stenosis represents high health risks to patients who currently have limited treatment options. New technologies for percutaneous heart valve implantation still have limitations.

Valve design requirements and limitations were implemented to develop PAV concepts. The implementation of the Fung type material model to accurately simulate the tissue with in-plane shear aided in the analysis of the material and valve designs. Concept A was chosen for refinement as a result of the following advantages:

- Concept A has a unique valve and leaflet design
- It has a more beneficial height and profile
- It possesses better fixation properties
- It is less susceptible to paravalvular leakage due to the polyester tube on the outside which also facilitates tissue ingrowth and fixation.
- It has lower stress concentrations according to the FEA simulations

Kangaroo pericardium was found to be suitable for this application due to the following advantages:

- Its thickness benefits the requirement for a lower profile valve
- The tearing tests shown that kangaroo tissue is strong enough
- It is thicker than native human valve tissue, which makes it mechanical fit, although it is less stiff
- Valves manufactured from kangaroo pericardium presented no signs of tissue failure
- Kangaroo pericardium poses extensibility advantages over bovine which may aid in over expansion of the valve and reduce the possibility for regurgitation.

## CONCLUSIONS AND RECOMMENDATIONS

- The preliminary pulse duplicator tests revealed no damage to the valves manufactured from kangaroo pericardium

The numerical simulations and testing revealed the following important points:

- The leaflets should preferably be cut from the same piece of tissue
- The tissue fibres must be aligned in the circumferential direction of the valve
- Over and under dilation of 1 mm is acceptable
- A sheath may be needed to be placed over the valve during placement
- Care should be taken during placement in order not to interfere with the coronary ostia or mitral valve which again emphasizes the benefit of a lower valve height

The developed prototypes prove to be feasible and can serve as a basis for continued research and development.

## 10. REFERENCES

- Anderson, H. R., Knudsen, L. L., and Hasekam, J. M. (1992). Transluminal implantation of artificial heart valves. Description of a new expandable aortic valve and initial results with implantation by catheter technique in closed chest pigs. *European Heart Journal*, Vol. **13**(5), pp.704-708.
- Arcidiacono, G., Corvi, A., and Severi, T. (2005). Functional analysis of bioprosthetic heart valves. *Journal of Biomechanics*, Vol. **38**, pp.1483-1490.
- BARD OEM. (2008). *Implantable Textiles - Tubular Fabrics*. [online]. [Accessed 10 October 2008]. Available form World Wide Web: <<http://www.bardpvoem.com/pages/tubular.html>>
- Belytschko, T., Liu, W. K., and Moran, B. (2000). *Nonlinear Finite Elements for Continua and Structures*. Chichester: Wiley.
- Billiar, K. L. and Sacks, M. S. (2000). Biaxial Mechanical Properties of the Natural and Gluteraldehyde Treated Aortic Valve Cusp - Part I: Experimental Results. *Journal of Biomechanical Engineering*, Vol. **122**, pp.23-30.
- Billiar, K. L. and Sacks, M. S. (2000). Biaxial Mechanical Properties of the Natural and Gluteraldehyde Treated Aortic Valve Cusp - Part II: A Structural Constitutive Model. *Journal of Biomechanical Engineering*, Vol. **122**, pp.327-335.
- Boyer, L. (2008). *Surgical Skills Laboratory*. [online]. [Accessed 18 11 2008]. Available form World Wide Web: <[http://www.medicine.usask.ca/surgery/surgical-skills-lab/Suture Lab Handout](http://www.medicine.usask.ca/surgery/surgical-skills-lab/Suture%20Lab%20Handout)>
- Brounstein, K., Feygin, D., Hu, M., Koop, T., and Lee, L. (2007). *Science-Based Business Initiative Fair*. [online]. [Accessed 18 11 2008]. Available form World Wide Web: <[http://www.hbs.edu/units/tom/conferences/docs/Aortic Valve Space Station.pdf](http://www.hbs.edu/units/tom/conferences/docs/Aortic_Valve_Space_Station.pdf)>
- Burriesci, G., Howard, I. C., and Patterson, E. A. (1999). Influence of Anisotropy on the Mechanical Behaviour of Bioprosthetic Heart Valves. *Journal of Medical Engineering*, Vol. **23**(6), pp.203-215.
- (2008). *CoreValve*. [online]. [Accessed 29 September 2008]. Available form World Wide Web: <<http://www.corevalve.com/index.aspx>>
- Cribier, A., Eltchaninoff, H., Bash, A., Borenstein, N., Tron, C., Bauer, F., Derumeaux, G., Anselme, F., Laborde, F., and Leon, M. B. (2002). Percutaneous Transcatheter Implantation of an Aortic Valve Prosthesis for Calcific Aortic Stenosis: First Human Case Description. *Circulation*, Vol. **106**(24), pp.3006-3008.

## REFERENCES

- Dunn, L. D. (2008). *Wound Closure Manual*. [online]. [Accessed 20 11 2008]. Available form World Wide Web: <[http://www.uphs.upenn.edu/surgery/dse/simulation/Wound\\_Closure\\_Manual.pdf](http://www.uphs.upenn.edu/surgery/dse/simulation/Wound_Closure_Manual.pdf)>
- (2008). *Edwards Lifesciences*. [online]. [Accessed 29 September 2008]. Available form World Wide Web: <<http://www.edwards.com/>>
- Esterhuyse, A. (2008). *Structural Design and Analysis of a Stent for Implimentation in a Percutaneous Aortic Heart Valve*. Stellenbosch: University of Stellenbosch.
- Fung, Y. (1993). *Biomechanics: Mechanical Properties of Living Tissues*. New York: 2nd ed. Springer.
- García Páez, J. M., Jorge Herrero, E., Carrera Sanmartín, A., Millán, I., Cordon, A., Martín Maestro, M., Rocha, A., Arenaz, B., and Castillo-Olivares, J. L. (2003). Comparison of the mechanical behaviors of biological tissues subjected to uniaxial tensile testing: pig, calf and ostrich pericardium sutured with Gore-Tex. *Biomaterials*, Vol. **24**, pp.1671-1679.
- GORE-TEX. (2008). *GORE-TEX Suture*. [online]. [Accessed 10 October 2008]. Available form World Wide Web: <<http://www.goremedical.com/suture/index>>
- Hoffman, A. H. and Grigg, P. (1984). A method for measuring strains in soft tissue. *Journal of Biomechanics*, Vol. **17**(10), pp.795-800.
- Holzapfel, G. A. (2000). *Nonlinear solid mechanics :a continuum approach for engineering*. Chichester, West Sussex: Wiley.
- International Organization for Standardization. (2005). *Cardiovascular implants - Cardiac valve prosthesis*. ISO.
- Johnson&Johnson. (2008). *National Association of Orthopaedic Nurses (NAON)*. [online]. [Accessed 20 11 2008]. Available form World Wide Web: <[http://www.orthonurse.org/portals/0/knot\\_tying.pdf](http://www.orthonurse.org/portals/0/knot_tying.pdf)>
- Kar, S. and Shah, P. K. (2006). Impact of new percutaneous techniques of aortic valve replacement on cardiology/cardiac surgical practice. *In: Transcatheter Valve Repair*, London: Taylor & Fransis, pp.139-144.
- Kay, J. D. and Carroll, J. D. (2006). Hemodynamic evaluation of aortic valve disease and indications for repair/replacement. *In: Transcatheter Valve Repair*, London: Taylor & Fransis, pp.127-137.
- Kim, H., Lu, J., Sacks, M. S., and Chandran, K. B. (2006). Dynamic Simulation of Pericardial Bioprosthetic Heart Valve Function. *Journal of Biomechanical Engineering*, Vol. **128**, pp.717-724.

## REFERENCES

- Labrosse, M. R., Beller, C. J., Robicsek, F., and Thubrikar, M. J. (2006). Geometric modeling of functional trileaflet aortic valves: Development and clinical applications. *Journal of Biomechanics*, Vol. **39**, pp.2665-2672.
- Lemmon, J. D. (2006). Valve testing: Durability and beyond. *In: Transcatheter Valve Repair*, London: Taylor & Fransis, pp.359-368.
- Lim, K. O. and Cheong, K. C. (1994). Effect of suturing on the mechanical properties of bovine pericardium - implications for cardiac valve bioprosthesis. *Medical engineering & physics*, Vol. **16**(6), pp.526-530.
- MSC.Marc. (2007). *Marc user manual*. MSC Software.
- Neethling, W. 2008. Interview with the author on 2008. E-mail correspondence.
- Neethling, W., Cooper, S., van den Heever, J., Hough, J., and Hodge, A. (2002). Evaluation of kangaroo pericardium as an alternative substitute for reconstructive cardiac surgery. *Journal of Cardiovascular Surgery*, Vol. **43**(3), pp.301-306.
- Neethling, W. M., Glancy, R., and Hodge, A. J. (2004). ADAPT-Treated Porcine Valve Tissue (Cusp and Wall) versus Medtronic Freestyle and Prima Plus: Crosslink Stability and Calcification Behavior in the Subcutaneous Rat Model. *The journal of heart valve disease*, Vol. **13**(4).
- Sacks, M. S. (2000). Biaxial Mechanical Evaluation of Planar Biological Materials. *Journal of Elasticity*, Vol. **61**(1-3), pp.199-246.
- Sacks, M. S., Smith, D. B., and Hiester, E. D. (1998). The aortic valve microstructure: Effects of transvalvular pressure. *Journal of Biomedical Materials Research*, Vol. **41**(1), pp.131-141.
- Sacks, M. S. and Sun, W. (2003). Multiaxial mechanical behavior of biological materials. *Annual Review of Biomedical Engineering*, Vol. **5**, pp.251-284.
- Shekar, P. S., Soltesz, E. G., and Cohn, L. H. (2006). Established methods of aortic valve repair and replacement. *In: Transcatheter Valve Repair*, London: Taylor & Fransis.
- Smith, D. B., Sacks, M. S., Pattany, P. M., and Schroeder, R. (1999). Fatigue-induced changes in bioprosthetic heart valve three-dimensional geometry and the relation to tissue damage. *Journal of heart valve disease*, Vol. **8**(1), pp.25-33.
- Sun, W., Abad, A., and Sacks, M. S. (2005). Simulated Bioprosthetic Heart Valve Deformation Under Quasi-static Loading. *Journal of Biomechanical Engineering*, Vol. **127**(6), pp.905-914.

## REFERENCES

- Sun, W. and Sacks, M. S. (2005). Finite element implementation of a generalized Fung-elastic constitutive model for planar soft tissues. *Biomechanics and Modeling in Mechanobiology*, Vol. 4(2-3), pp.190-199.
- Thubrikar, M. (1990). *The Aortic Valve*. Florida: CRC Press.
- Timoshenko, S. P. and Goodier, J. N. (1970). *Theory of Elasticity*. Singapore: McGraw-Hill.
- Troop7. (2008). *How To Tie Popular Knots*. [online]. [Accessed 20 11 2008]. Available form World Wide Web: <<http://www.troop7.org/Knots/>>
- Van Aswegen, K. (2008). *Dynamic Modelling of a Stented Aortic Valve*. Stellenbosch: University of Stellenbosch.
- Van der Merwe, W. J. (2008). *Rapid 3D Measurement Using Digital Video Cameras*. Stellenbosch.
- Ward, R. P. and Lang, R. M. (2006). Aortic stenosis: Pathophysiologic, clinical, and echocardiographic manifestations. In: *Transcatheter Valve Repair*, London: Taylor & Francis, pp.115-126.
- Webb, J. G., Chandavimol, M., Thompson, C. R., Ricci, D. R., Carere, R. G., Munt, B. I., Buller, C. E., Pasupati, S., and Lichtenstein, S. (2006). Percutaneous Aortic Valve Implantation Retrograde From the Femoral Artery. *Circulation*, Vol. 113, pp.842 - 850.
- Zilla, P., Brink, J., Human, P., and Bezuidenhout, D. (2008). Prosthetic heart valves: Catering for the few. *Biomaterials*, Vol. 29(4), pp.385-406.

APPENDIX A

EXPERIMENTAL STRESS-STRAIN RELATIONSHIPS

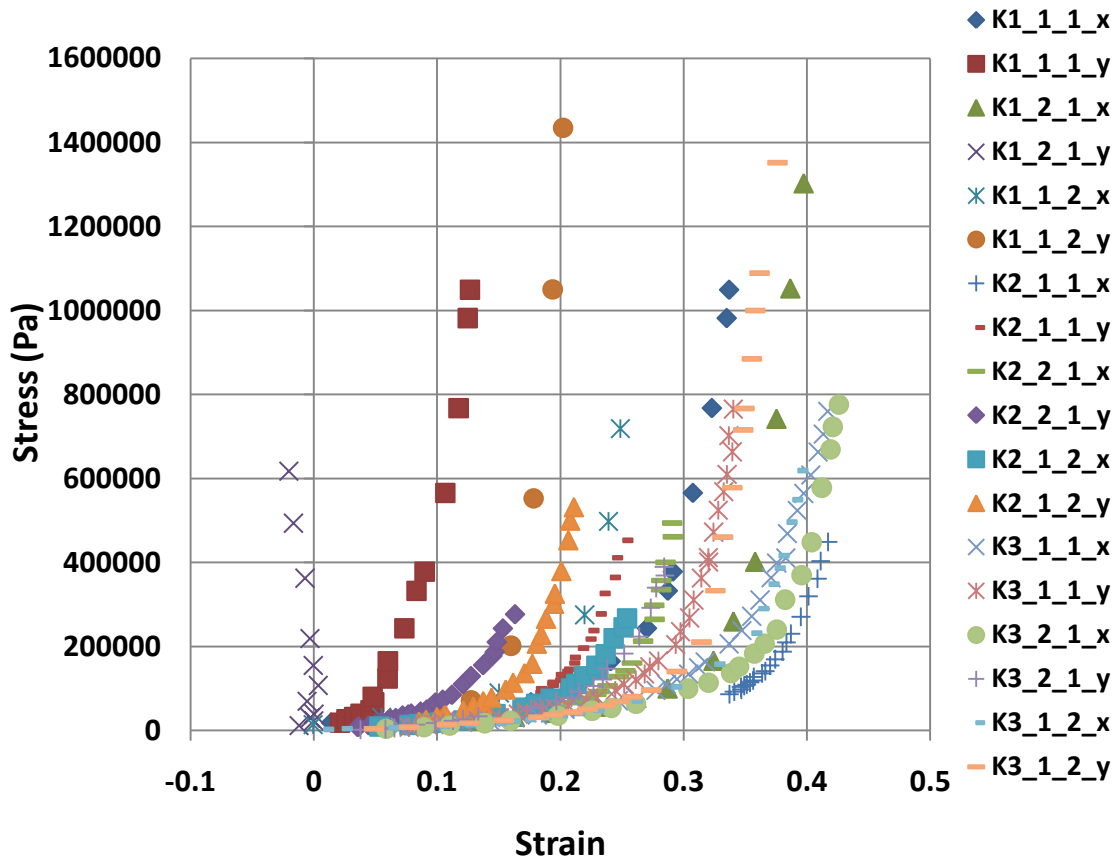


Figure A-1: Normal stress-strain relationships for kangaroo tests for ratios of  $P_x:P_y = 1:1, 1:2$  and  $2:1$ .

# EXPERIMENTAL STRESS-STRAIN RELATIONSHIPS

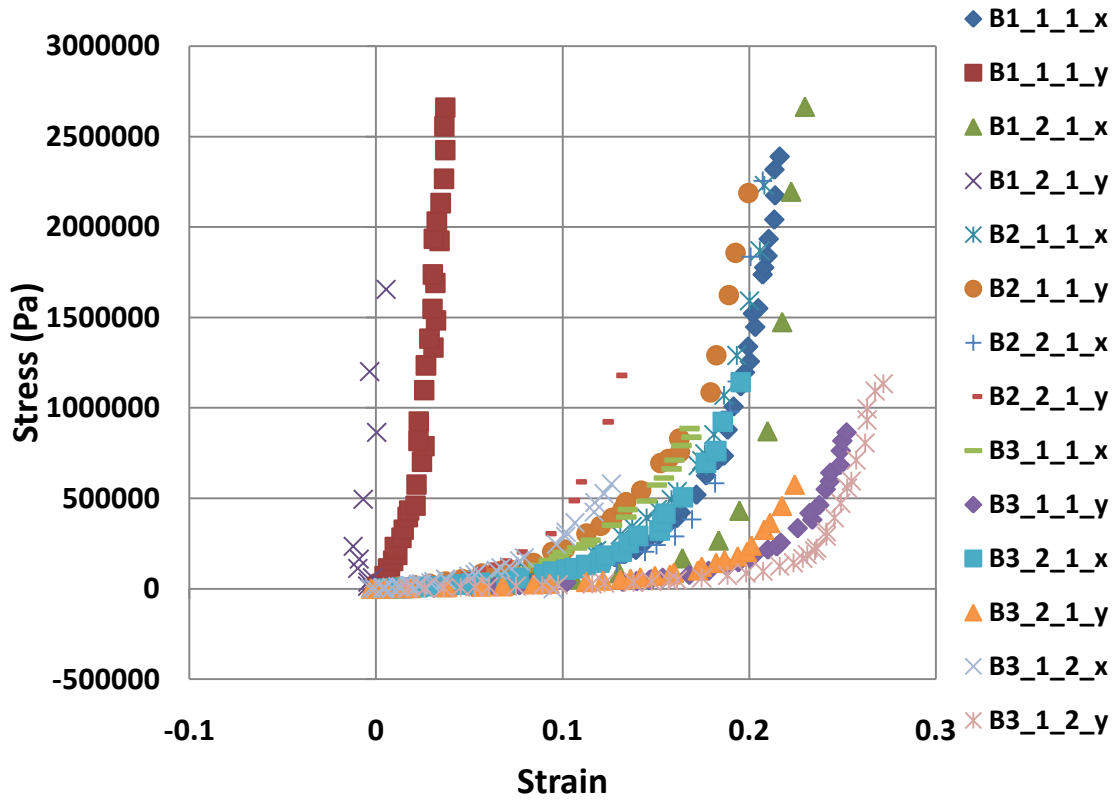


Figure A-2: Normal stress-strain relationships for bovine tests for ratios of  $P_x:P_y = 1:1, 1:2$  and  $2:1$

# EXPERIMENTAL STRESS-STRAIN RELATIONSHIPS

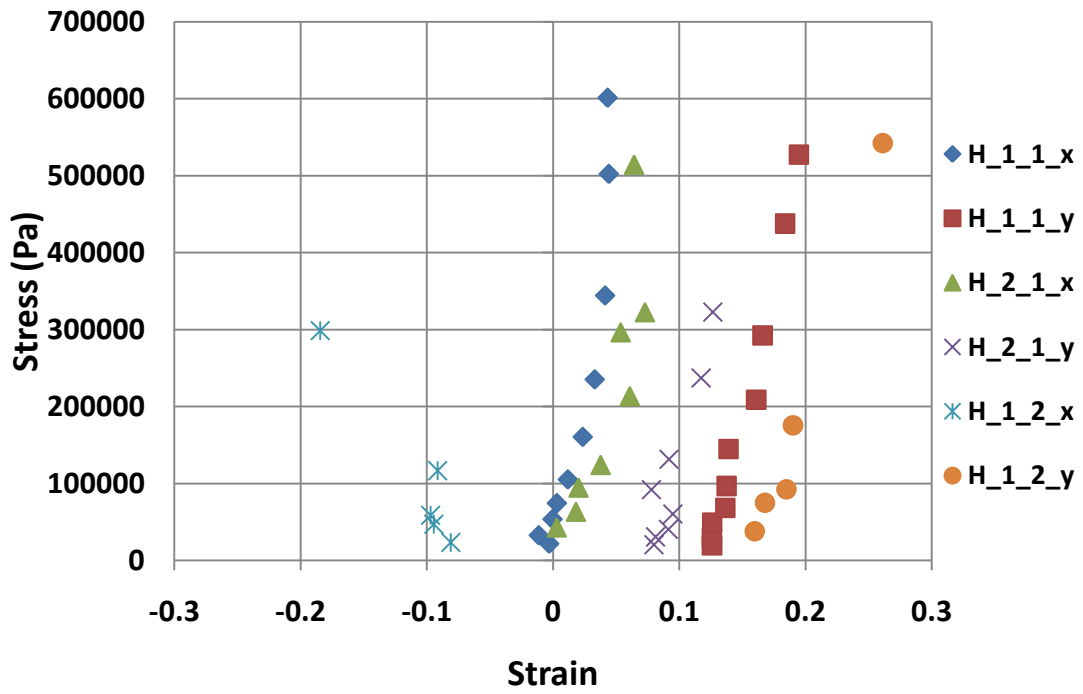


Figure A-3: Normal stress-strain relationships for human tests for ratios of  $P_x:P_y = 1:1, 1:2$  and  $2:1$

EXPERIMENTAL STRESS-STRAIN RELATIONSHIPS

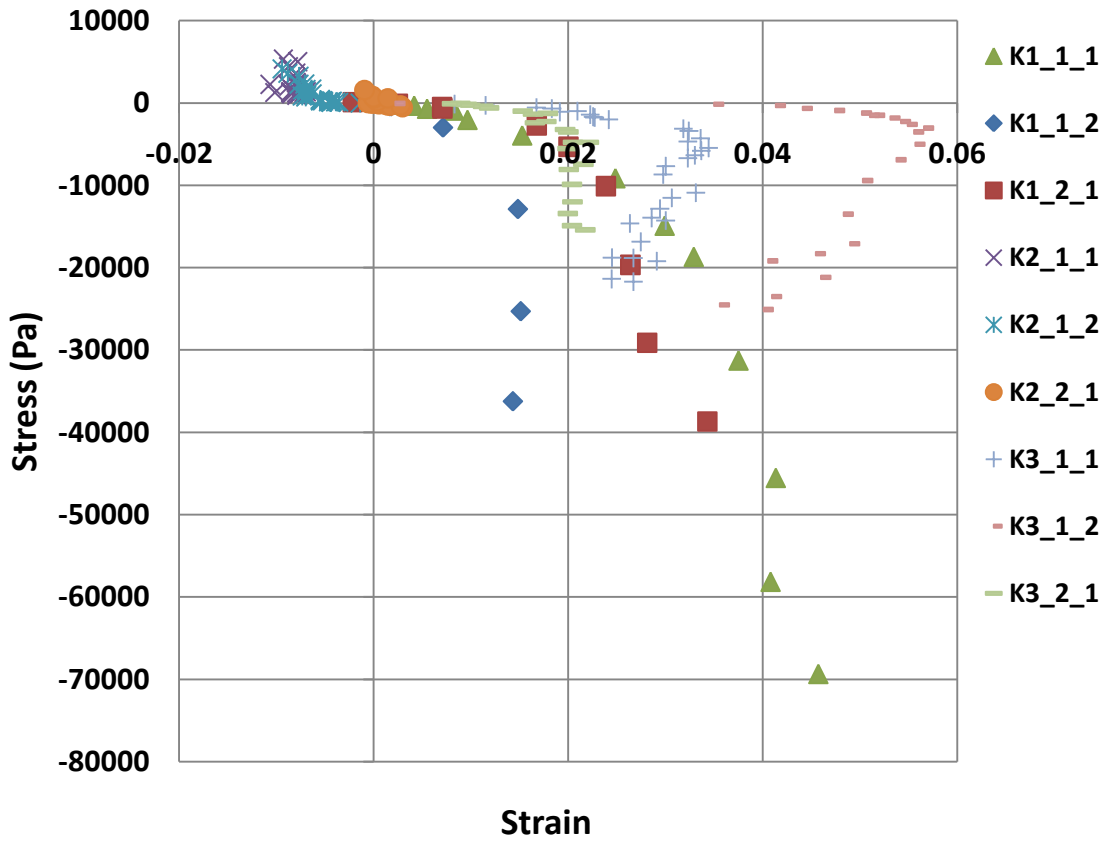


Figure A-4: Shear stress-strain relationships for kangaroo tests for ratios of  $P_x:P_y = 1:1, 1:2$  and  $2:1$

EXPERIMENTAL STRESS-STRAIN RELATIONSHIPS

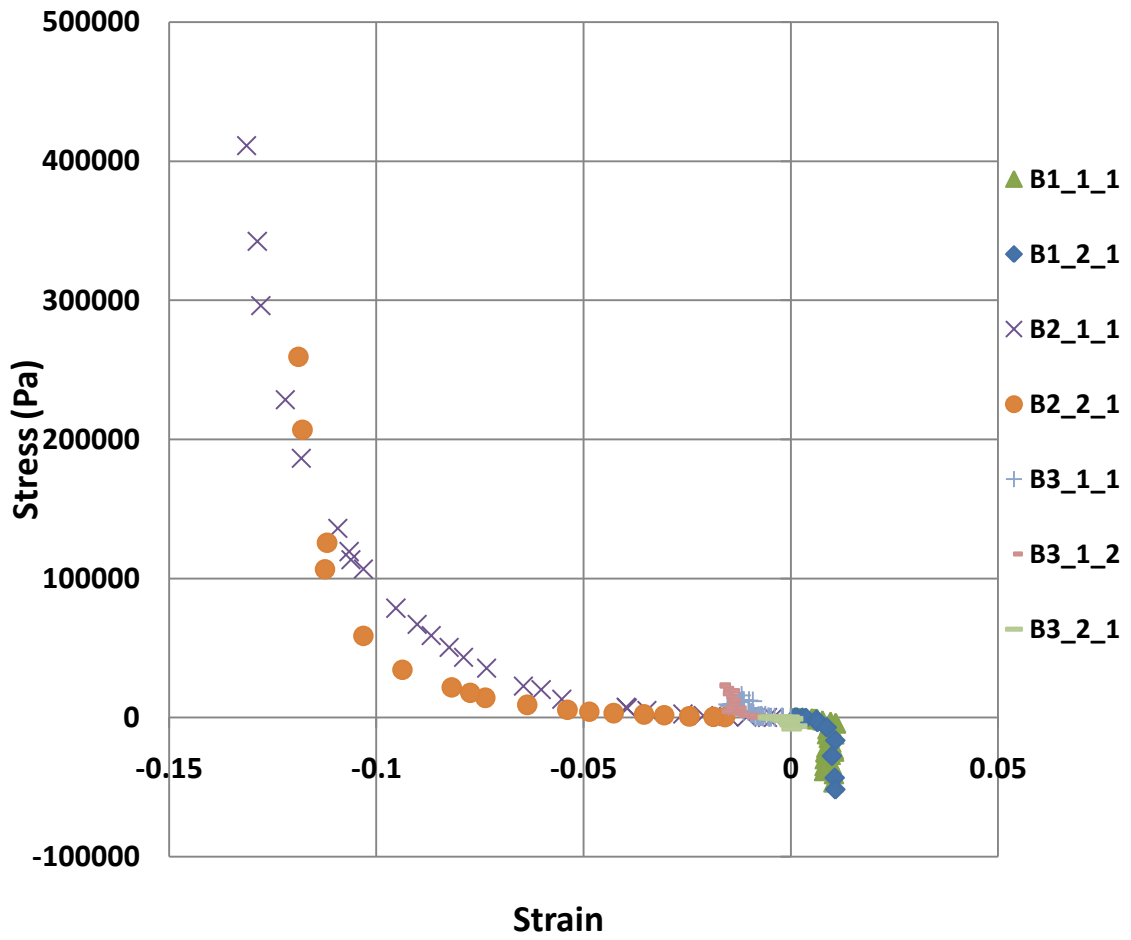


Figure A-5: Shear stress-strain relationships for bovine tests for ratios of  $P_x:P_y = 1:1, 1:2$  and  $2:1$

EXPERIMENTAL STRESS-STRAIN RELATIONSHIPS

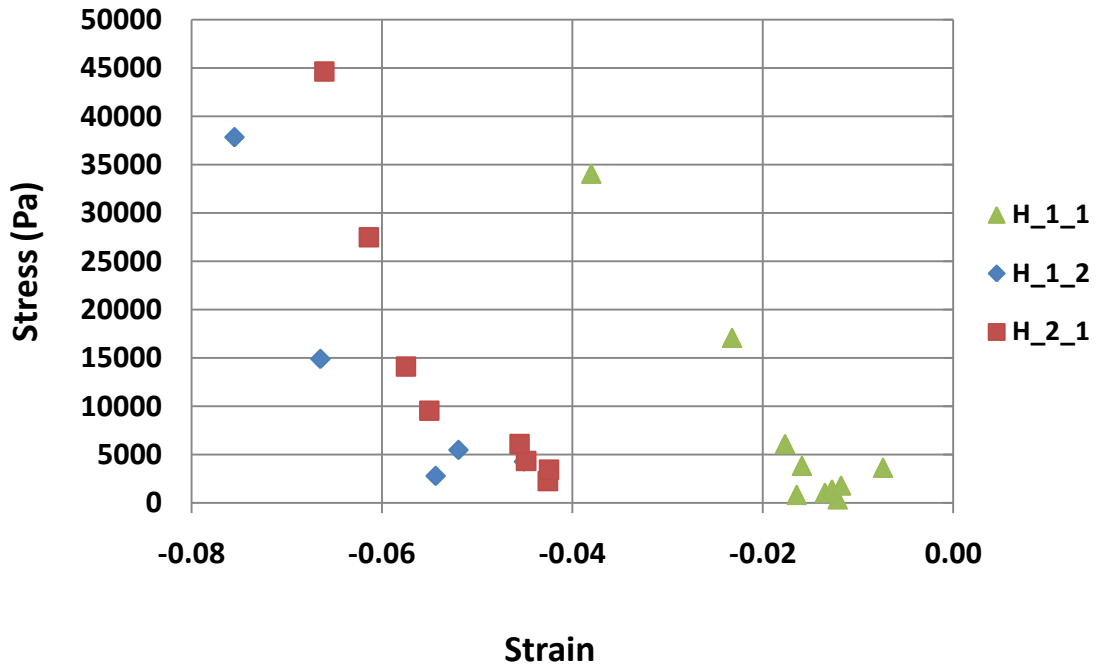


Figure A-6: Shear stress-strain relationships for human tests for ratios of  $P_x:P_y = 1:1, 1:2$  and  $2:1$

Table A-1: Fung parameters for the bovine and kangaroo pericardium samples

	C(kPa)	A1	A2	A3	A4	A5	A6
<b>Bovine #1</b>	14.38	46.06	142.70	27.38	5.92	-1.70	4.92
<b>Bovine #2</b>	36.71	43.41	28.36	0.00	28.16	21.05	0.67
<b>Bovine #3</b>	6.61	53.23	34.01	-8.08	2.44	-2.32	1.44
<b>Kang #1</b>	6.69	19.66	33.97	5.51	0.74	-0.89	-0.26
<b>Kang #2</b>	57.52	7.01	17.18	-5.21	4.11	0.09	0.13
<b>Kang #3</b>	3.30	27.99	38.81	-19.40	0.98	-0.49	-0.02

## APPENDIX B

### USER SUBROUTINE FOR FEA IMPLEMENTATION

```

subroutine hypela2(d,g,e,de,s,t,dt,ngens,n,nn,kcus,matus,ndi,
                 nshear,disp,dispt,coord,ffn,frotn,strechn,eigvn,ffnl,
                 frotn1,strechn1,eigvn1,ncrd,itel,ndeg,ndm,
                 nnode,jtype,lclass,ifr,ifu)
c
c
c
c ***** user subroutine for defining material behavior *****
c
c
c CAUTION : Due to calculation of the Deformation gradients, Stretch Tensors and
c           Rotation tensors at previous and current states, the analysis can be
c           computationally expensive. Please use the user subroutine -> hypela
c           if these kinematic quantities are not needed in the constitutive model
c
c
c IMPORTANT NOTES :
c
c (1) F,R,U are only available for continuum and membrane elements (not for
c     shells and beams).They are also not available for higher order Herrmann
c     elements and Herrmann element types 155 to 157
c
c (2) For total Lagrangian formulation use the -> 'Elasticity,1' card(=
c     total Lagrange with large disp) in the parameter section of input deck.
c     For updated Lagrangian formulation use the -> 'Plasticity,3' card(=
c     update+finite+large disp+constant d) in the parameter section of
c     input deck.
c
c
c     d          stress strain law to be formed
c     g          change in stress due to temperature effects
c     e          total elastic strain
c     de         increment of strain
c     s          stress - should be updated by user
c     t          state variables (comes in at t=n, must be updated
c                to have state variables at t=n+1)
c     dt         increment of state variables
c     ngens      size of stress - strain law
c     n          element number
c     nn         integration point number
c     kcus(1)    layer number
c     kcus(2)    internal layer number
c     matus(1)   user material identification number
c     matus(2)   internal material identification number
c     ndi        number of direct components
c     nshear     number of shear components
c     disp       incremental displacements
c     dispt      displacements at t=n   (at assembly,          lovl=4) and
c                displacements at t=n+1 (at stress recovery, lovl=6)
c     coord      coordinates
c     ncrd       number of coordinates
c     ndeg       number of degrees of freedom
c     itel       dimension of F and R, either 2 or 3
c     nnode      number of nodes per element
c     jtype      element type

```

## USER SUBROUTINE FOR FEA IMPLEMENTATION

```

c      lclass(1)      element class
c      lclass(2)      Herrmann element flag (1)-lower order, (2)- higher order
c      ifr           set to 1 if R has been calculated
c      ifu           set to 1 if strech has been calculated
c
c      at t=n       :
c
c      ffn          deformation gradient
c      frotn        rotation tensor
c      strechn      square of principal stretch ratios, lambda(i)
c      eigvn(i,j)   i principal direction components for j eigenvalues
c
c      at t=n+1     :
c
c      ffn1         deformation gradient
c      frotn1       rotation tensor
c      strechn1     square of principal stretch ratios, lambda(i)
c      eigvn1(i,j)  i principal direction components for j eigenvalues
c
c      The following operation obtains U (stretch tensor) at t=n+1 :
c
c      call scla(un1,0.d0,itel,itel,1)
c      do 3 k=1,3
c        do 2 i=1,3
c          do 1 j=1,3
c            un1(i,j)=un1(i,j)+dsqrt(strechn1(k))*eigvn1(i,k)*eigvn1(j,k)
c1         continue
c2        continue
c3       continue
c
c
c      #ifndef _IMPLICITNONE
c         implicit none
c      #else
c         implicit logical (a-z)
c      #endif
c      ** Start of generated type statements **
c      real*8 coord, d, de, disp, dispt, dt, e, eigvn, eigvn1, ffn, ffn1
c      real*8 frotn, frotn1, g
c      integer ifr, ifu, itel, jtype, kcus, lclass, matus, n, ncrd, ndeg
c      integer ndi, ndm, ngens, nn, nnode, nshear
c      real*8 s, strechn, strechn1, t
c
c      real*8 C,A_1,A_2,A_3,A_4,A_5,A_6,Q,z_1,z_2,z_3,I,J
c      real*8 e_1,e_2,e_3,Q_e
c      ** End of generated type statements **
c
c      dimension e(*),de(*),t(*),dt(*),g(*),d(ngens,*),s(*)
c      dimension n(2),coord(ncrd,*),disp(ndeg,*),matus(2),
c      *      dispt(ndeg,*),ffn(itel,*),frotn(itel,*),
c      *      strechn(itel),eigvn(itel,*),ffn1(itel,*),
c      *      frotn1(itel,*),strechn1(itel),eigvn1(itel,*),
c      *      kcus(2),lclass(2)
c
c      -----
c      HYPELA2 FOR GENERALIZED FUNG-ELASTIC CONSTITUTIVE MODEL
c      FOR PLANAR SOFT TISSUES
c      -----
c
c      CONSTANTS
c      -----
c
c      C = 15000.d0
c      A_1 = 40.59
c      A_2 = 18.70

```

## USER SUBROUTINE FOR FEA IMPLEMENTATION

```

A_3 = 17.70
A_4 = 6.94
A_5 = 5.94
A_6 = 5.d0

```

```

-----
C
C
C   CALCULATE THE TANGENT STIFFNESS AT THE BEGINNING OF THE ITERATION
C-----
Q = A_1*(e(1))**2 + A_2*(e(2))**2
* + 2.d0*A_3*e(1)*e(2) + A_4*(e(3))**2
* + 2.d0*A_5*e(3)*e(1) + 2.d0*A_6*e(3)*e(2)

z_1 = 2.d0*(A_1*e(1) + A_3*e(2) + A_5*e(3))
z_2 = 2.d0*(A_2*e(2) + A_3*e(1) + A_6*e(3))
z_3 = 2.d0*(A_4*e(3) + A_5*e(1) + A_6*e(2))

DO I=1,ngens
  DO J=1,ngens
    d(I,J)=0.0D0
  ENDDO
ENDDO

d(1,1) = (exp(Q)*C/2.d0)*(2.d0*A_1 + z_1**2)
d(2,2) = (exp(Q)*C/2.d0)*(2.d0*A_2 + z_2**2)
d(3,3) = (exp(Q)*C/2.d0)*(2.d0*A_4 + z_3**2)
d(1,2) = (exp(Q)*C/2.d0)*(2.d0*A_3 + z_1*z_2)
d(1,3) = (exp(Q)*C/2.d0)*(2.d0*A_5 + z_1*z_3)
d(2,3) = (exp(Q)*C/2.d0)*(2.d0*A_6 + z_2*z_3)
d(2,1) = d(1,2)
d(3,1) = d(1,3)
d(3,2) = d(2,3)

-----
C
C
C   CALCULATE THE STRESS AT THE END OF THE INCREMENT (Vol. A, P 367)
C-----
DO I=1,ngens
  DO J=1,ngens
    s(I)=s(I)+d(I,J)*de(J)
  ENDDO
ENDDO

-----
C
C
C   CHANGE IN STRESS DUE TO TEMPERATURE EFFECTS
C-----
DO I=1,ngens
  g(I) = 0.d0
ENDDO

-----
return
end

```